KUVEMPU UNIVERSITY

Synthesis and Characterization of Graphene/Metal oxides Nanocomposites for Supercapacitor Applications

A thesis submitted to
Kuvempu University
for the award of the degree of

DOCTOR OF PHILOSOPHY
IN
PHYSICS

By
Mrs. Madhuri D.R. M.Sc.

Research Guide
Dr. Ashok R. Lamani M.Sc., Ph.D.
Professor of Physics
Kuvempu University

Department of P.G. Studies and Research in Physics
Kuvempu University
Jnana Sahyadri, Shankaraghatta – 577 451
Shivamogga District, Karnataka, INDIA

2022

Dedicated to My
Family
for their endless love, support and
encouragement

Mrs. Madhuri D.R.
Research scholar
Dept. of P.G. Studies and Research in Physics
Kuvempu University
Jnana Sahyadri, Shankaraghatta – 577 451
Shivamogga District, Karnataka, INDIA

Declaration

I do hereby declare that, the thesis entitled **“Synthesis and Characterization of Graphene/Metal oxides Nanocomposites for Supercapacitor Applications”** being submitted to the Kuvempu University for the award of the degree of **Doctor of Philosophy in Physics** is the result of original research work carried out by me in the Department of P.G. Studies and Research in Physics, Kuvempu University, Jnana Sahyadri, Shankaraghatta, under the constant support and immense guidance of **Dr. Ashok R. Lamani**, Professor and Chairman, Department of P.G. Studies and Research in Physics, Kuvempu University, Jnana Sahyadri, Shankaraghatta.

I further declare that this work or any part of it has not been submitted to any other university/institution or elsewhere by me or others for any degree or diploma.

Date : 28/09/2022
Place: Shankaraghatta

Madhuri · DR
Madhuri D.R.

KUVEMPU UNIVERSITY

Department of Studies in Physics
Jnana Sahyadri, Shankaragatta - 577451
Karnataka, INDIA
Mobile: +91 9845856893
Email: ashok1571972@gmail.com

Dr. Ashok.R. Lamani. Ph.D
Professor and Chairman
Chairman, BoS PG and UG
Director, School of Physical Sciences

Certificate

This is to certify that the thesis entitled **"Synthesis and Characterization of Graphene/Metal oxides Nanocomposites for Supercapacitor Applications"** being submitted to the Kuvempu University for the award of the degree of **Doctor of Philosophy in Physics,** is a bonafide record of the research work done by Mrs. Madhuri D.R. in the Department of P.G. Studies and Research in Physics under my supervision and guidance. I also certify that the thesis represents her independent, original, investigation without forming previously part of the award of any degree or diploma by any university or examining body.

Date : ೨೮/೦೯/೨೦೨೨

Place: Shankaraghatta

Dr. ASHOK R. LAMANI

Dr. Ashok. R. Lamani, M.Sc.,Ph.D.,
Professor
Dept. of P.G. Studies & Research in Physics
Kuvempu University, Jnana Sahyadri
SHANKARAGHATTA-577 451.

Acknowledgements

Words cannot express my gratitude to my esteemed guide Dr. Ashok R. Lamani, Professor and Chairman, Department of PG studies and research in Physics, Kuvempu University, Shankaraghatta, for his guidance, valuable patience, kind support and encouragement. He was incredibly helpful and supportive throughout this entire journey by providing feedback at each stage of my Ph.D., work. His immense patience, faith, and enthusiasm has always encouraged me in my research work and personal life to work harder. His passion and dedication about research have energized me at every step of my Ph.D., tenure. I am very fortunate to have been his Ph.D., student.

I would like to show my gratitude to Dr. H.S. Jayanna, Professor, Department of PG studies and research in Physics, Kuvempu University, Shankaraghatta, for giving valuable suggestions that helped me to make better performance.

I am also grateful to express my gratitude to Dr. Nagaraju G. Assistant Professor, Department of Chemistry, Siddaganga Institute of Technology, Tumakuru, for giving me an opportunity to utilize the lab facilities to conduct my research work and characterization facilities (XRD and FTIR). He has taught me, how to do organized research and communicate it across the scientific community.

I am extremely thankful to Dr. Shridhar Mundinmani, Assistant Professor, Department of Physics, Siddaganga Institute of Technology, Tumakuru, who helped me in conducting electrochemical studies, analysing data and calculation part.

I wish to express my sincere thanks to CeNS Bengaluru for TEM facility, funded by a TPF Nanomission, GOI project at Centre for Nano and Soft Matter Sciences, Bengaluru.

I would also like to extend my deepest gratitude to Dr. C. Kavitha, Assistant Professor, Department of Physics, BMS Institute of Technology & MGMT, Bengaluru for providing facility of Raman spectra.

I extend my thanks to CoE-BMS College of Engineering for providing SEM facility.

I take this opportunity to express my gratitude to Dr. J. Sannappa, Dr. Sudha and Dr. G.B. Devidas, Department of PG studies and research in Physics, Kuvempu University, Shankaraghatta.

I would like to express my gratitude to Dr. Udaya Kumar, Dr. G.K. Raghu, Dr. K. Uma, Dr. H.N. Anil Rao, Department of Chemistry, SIT Tumakuru, for their support and for providing characterization facilities.

I wish to express my sincere thanks to my senior research group Dr. C.S. Naveen, Dr. M.P. Rajeeva, Dr. V.S. Chaturmukha, Dr. H.K. Reshma, Dr. B.S. Avinash, Dr. A.S. Jagadeesha, Dr. Rangaswamy D.R, Mr. M. Hemantha, Dr. B.M. Harish for their valuable suggestions and guidance during my Ph.D., work. I also express my regards to my colleagues Mrs. K. Kavyashree, Dr. Sunitha B Patil, for their valuable inputs. Also, I thank Mr. Raviteja G, and Mr. Sandeep Dongre for their support.

I extend my thanks to my friends Dr. Tangarani, Dr. B.G. Akshatha, Dr. B.N. Vimala, Mrs. Shwetha, Mrs. Aishwarya, for their boundless love, care and encouragement.

I would like to extend my thanks to my friends Dr. Udayabhanu, Dr. Manukumar, Dr. M. Shashank, Dr. K. Lingaraju, Dr. Sumedha Rao, Mrs. Pavithra, Mrs. V. Pavithra, Ms. Tanuja, Ms. H.P. Divya, Ms. T.L. Soundarya in SIT, Tumakuru, for their valuable suggestions.

Now, I want to convey my deepest sense of gratitude and express my utmost feelings to my parents Late. Mr. Ramesh D.S. Jois, Mangala J.N. and younger sister Ms. Madhura D.R. for their love, unconditional support, trust and encouragement.

I could not have undertaken this journey without my husband Mr. Achyut M. Potdar. I would like to express my special thanks to him for his belief in me, his motivational words and all support. Also, I would like to extend my gratitude to my little daughter Tanvi A. Potdar for her cooperation.

I will forever be thankful to my in-laws, cousins, uncles and all relatives for their continuous support, guidance and understanding.

My sincere thanks to Mr. Ramesh K.N, Mahesh S. and Basavachar S, Mr. Srinivas, Smt. Sarojamma, Non-teaching staff, Department of Physics, Kuvempu University for their support.

Finally, I thank all my teachers, classmates, friends and non-teaching staff who supported me a lot throughout my research journey. I thank Kuvempu University for providing research facilities and opportunity to pursue Ph.D., degree. I express my utmost thanks to all those who helped me directly or indirectly in successful completion of my research work.

Above all I thank the God who is being with me and showers his blessings and grace towards me throughout my research journey.

……….. *Madhuri D.R.*

LIST OF ABBREVIATIONS

BSEs - Back scattered electrons

CCD - Charged couple device

C_{dl} - Electrical double layer capacitance

CNFs - Carbon nanofibers

CNHs - Carbon Nanohorns

CNTs - Carbon nanotubes

CO - Carbo monoxide

C_p - Pseudo-capacitance

CV - Cyclic voltammetry

CVD - Chemical vapour deposition

ECs - Electrochemical capacitors

EDAX - Energy-dispersive X-ray analysis

EDAX - Energy dispersive X-ray analysis

EDLC - Electric double layer capacitor

EIS - Electrochemical impedance spectroscopy

EVs - Electric vehicles

FEG - Field emission guns

FET - Field effect transistor

FLG - Few-layer graphene

FT - Fourier transform

FTIR - Fourier transform infrared spectroscopy

GCD - Galvanostatic charge-discharge

GO - Graphene oxide

HEVs - Hybrid electric vehicles

ICE - Internal combustion engine

NEC - Nippon Electric Company

Ppm - Parts per million

PVD - Physical vapour deposition

R_{ct}	-	Charge transfer resistance
rGO	-	Reduced graphene oxide
R_s	-	Solution resistance
SAED	-	Selected area electron diffraction
SCS	-	Solution combustion synthesis
SDD	-	Silicon drift detectors
SEM	-	Scanning electron microscopy
SEs	-	Secondary electrons
SWCNHs	-	Single-wall carbon nanohorns
TEM	-	Transmission electron microscopy
W	-	Warburg impedance
XRD	-	X-ray diffraction

LIST OF TABLES

LIST OF FIGURES

Page No.

Ouriginal
by Turnitin

Document Information

Analyzed document	KU-TH-PHY-MADHURI-DR-22.pdf (D144648952)
Submitted	2022-09-23 08:43:00
Submitted by	Walmiki R H
Submitter email	walmiki_rh@rediffmail.com
Similarity	1%
Analysis address	walmiki_rh.kuvempu@analysis.urkund.com

Sources included in the report

SA	**Madras university, Chennai / S. MARY MARGARET.pdf** Document S. MARY MARGARET.pdf (D132515768) Submitted by: kkperumal3@gmail.com Receiver: kkperumal3.madra@analysis.urkund.com	5
SA	**Betsie.pdf** Document Betsie.pdf (D137900853)	1
SA	**Periyar University, Salem / P. KRISHNA PRIYA (PHYSICS) Shri Sakthi.pdf** Document P. KRISHNA PRIYA (PHYSICS) Shri Sakthi.pdf (D57861860) Submitted by: gomathi148@gmail.com Receiver: gomathi148.periyar@analysis.urkund.com	1
SA	**SYNTHESIS AND CHARACTERIZATION OF GRAPHENE METAL OXIDE FOR PHOTOCATALYTIC AND SUPERCAPACITOR APPLICATIONS.docx** Document SYNTHESIS AND CHARACTERIZATION OF GRAPHENE METAL OXIDE FOR PHOTOCATALYTIC AND SUPERCAPACITOR APPLICATIONS.docx (D141691307)	8
SA	**Anna University, Chennai / Synthesis and Characterzation Ph D THESIS by Saranya.pdf** Document Synthesis and Characterzation Ph D THESIS by Saranya.pdf (D40775432) Submitted by: azhaguvelg@gmail.com Receiver: azhaguvelg.annauniv@analysis.urkund.com	2
W	URL: https://ujcontent.uj.ac.za/vital/access/services/Download/uj:40723/SOURCE1 Fetched: 2021-05-15 17:42:06	2
SA	**Periyar University, Salem / jaishree.pdf** Document jaishree.pdf (D51753376) Submitted by: physicsvicas@gmail.com Receiver: physicsvicas.periyar@analysis.urkund.com	1
W	URL: https://core.ac.uk/download/pdf/144148517.pdf Fetched: 2021-08-17 13:59:36	1
W	URL: https://escholarship.org/content/qt3b62s818/qt3b62s818_noSplash_0261545bf00c23763ce49c628943d061.pdf Fetched: 2021-09-21 11:59:01	2

Entire Document

CONTENTS

Page No.

Chapter-5. Conclusions 173

Appendices

Preface

In the system of the electricity grid, power supply and demand must be equal at all the moment. Energy storage plays an essential role in this balancing act and helps to create a more flexible and reliable grid system. For this purpose, there are various types of energy storage devices such as batteries, fuel cells, supercapacitors, etc. Among all these, supercapacitors have the advantage of high-power density, better reversibility, long cycle life, and are much safer than batteries. Supercapacitors are constructed much like a battery in which there are two electrodes immersed in an electrolyte with an ion-permeable separator located between the electrodes.

Carbon materials are considered as the best material in the preparation of electrodes for supercapacitors because of their low cost, functional properties, and commercial availability. There is a wide range of carbon materials and their electrical property depends on their structure. Graphene is a two-dimensional honeycomb structured single atomic layer of sp^2 hybridized carbon atoms. Graphene oxide (GO) is an exciting material because of its low cost and easy conversion from GO to graphene. GO contains oxygen molecules in between carbon layers. It is then reduced to separate carbon layers into a single layer or few-layer graphene. In recent days the green approach of preparing reduced graphene oxide using plant extracts has attracted more attention among the research fraternity over the orthodox way of using chemicals. The green approach carries advantages like low cost and environmentally friendly nature. Here in this study, the reduction of graphene oxide is carried out using Phyllanthus Emblica, commonly known as amla.

Metal oxides are also promising materials for supercapacitors. They show higher value of specific capacitance than carbon materials but they have less stability. Carbon materials are more stable for supercapacitors. So, by combining these two materials we can expect an improved result is called synergistic effect.

Due to the rapidly expanding global economy, there exists few problems that are caused by a considerable increase in the usage of fossil fuels worldwide. The first one is the rapid consumption of existing fossil fuel reserves, and the second is the associated environmental issues, such as rising greenhouse gas emissions and general air and water pollution. To efficiently gather these intermittent energy sources, corresponding energy conversion and energy storage systems must be developed. Electrochemical supercapacitors are useful in this regard. These are the motivation factors to enter into this research field.

1.1 Nanoscience and nanotechnology

Recent advances in nanoscience and nanotechnology intend new and innovative applications in many industries. The promise of scientific development in a variety of fields, including medical, energy, materials and manufacturing and consumer goods, makes research in nanotechnology very interesting. Nanomaterials are materials having individual grain or particle sizes in the range of 1-100 nm in at least one dimension. 1 nm is nearly 1,00,000 times smaller than the diameter of human hair. It is difficult to imagine how small a nanoparticle is. Figure 1.1 shows the scale comparison of nanoparticle with other particles. The special optical, electrical, magnetic and other properties that arise in nanomaterials at this size make them intriguing. These new traits have the potential to significantly assist medicine, electronics and other industries.

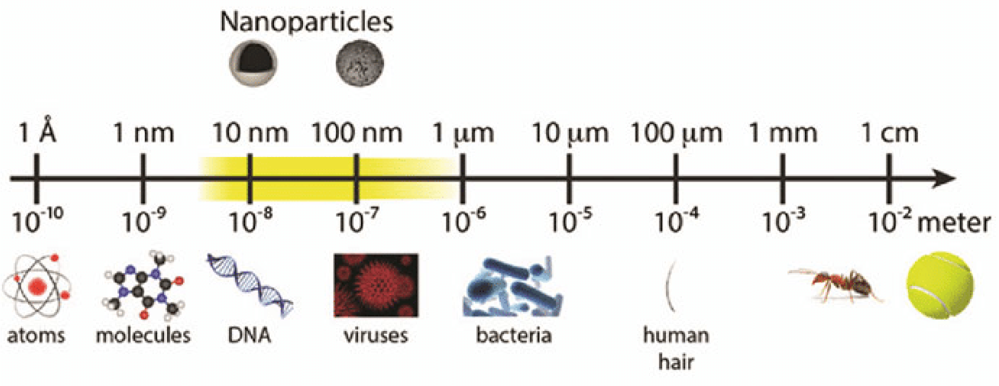

Fig. 1.1 Basic concept on length scale, illustrating size of nanomaterials.

Over the past few years, research has become more interested in the processing, structure, and characteristics of materials of grain sizes ranging from tens to few hundreds of nanometers. Researchers are discovering new methods to pattern and analyse materials at the nanoscale length scale, which is causing a revolution in materials science and engineering. There is a rapid development of new materials with excellent electrical, optical, magnetic, and mechanical capabilities for use in bioengineering, energy and environmental applications, and information technology [1].

Nanoscience is concerned with the synthesis, exploration, characterization, and application of nanostructured materials. Nanostructures act as a link between molecules and infinitely large bulk systems. Physical and chemical properties of nanomaterials can vary considerably from those of atomic-molecular or bulk materials of the same composition. The peculiarity of a nanomaterial's structural properties, energetics, responsiveness, dynamics, and chemistry are the cornerstone of nanoscience. Controlling the properties and responses of nanostructures can lead to the development of new devices and technologies [2].

Nanotechnology is the study and the manipulation of matter at length scales of the order of a few nanometers (100 atoms or so) to produce useful materials and devices. An emerging discipline in science is nanotechnology. Early in the 20th century, scientists realised that materials with ultrafine particle sizes have special features. At the annual meeting of the American Physical Society on December 29, 1959, Richard P. Feynman delivered the classic lecture titled "There's Plenty of Room at the Bottom," which launched a brand-new field called nanotechnology. He discussed small-scale manipulation and control of various things [3].

Feynman is referred to as the original pioneer of nanotechnology because of his vision. Feynman's remarkable insight sparked a great deal of debate and interest in engineering at the very small scale within the research community. However, due to a lack of appropriate tools and methodologies, it took the research community approximately three decades to realise his goal.

Another pioneer in nanotechnology who pushed the boundaries of imagination was Eric Drexler. He argued for using chemistry's potential to create molecular machines and predicted the profound effects. He discussed the value of taking an interdisciplinary approach to advance nanoscience and nanotechnology in his well-known book, “Engines of Creation: The Coming Era of Nanotechnology”. Pictures of these two pioneers are shown in figure 1.2.

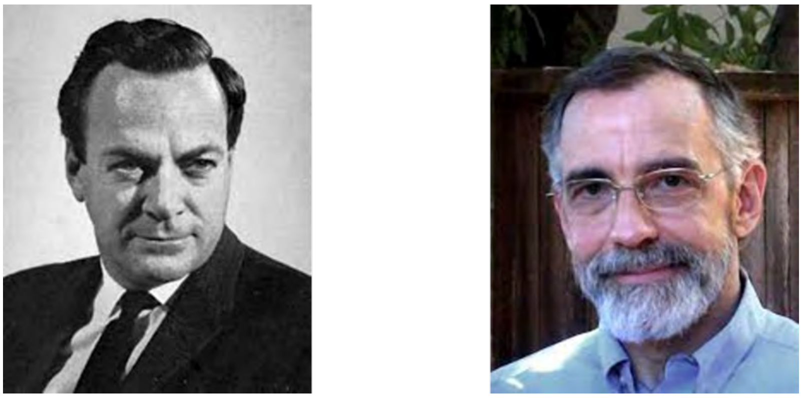

Fig. 1.2 Photographs of Richard P. Feynman and Eric Drexler.

Nanomaterials and Nanotechnology have seen tremendous growth in the twenty-first century. This field, however, is not new because its seeds have been sown for centuries. The stained-glass windows and Lycurgus cup are Medieval/Roman era examples that contain a few tens of parts per million (ppm) of silver and gold nanoparticles in the glass matrix and exhibit unique optical properties. For over a thousand years, the Chinese have used gold nanoparticles as an inorganic dye to add red colour to their ceramic porcelains. Faraday created a stable colloidal gold in 1857, which was destroyed during Second World War Colloidal gold has been and continues to be used to diagnose a variety of diseases and in the treatment of arthritis [4].

Norio Taniguchi coined the word "nanotechnology" in 1974 to describe the exact and perfect tolerances needed for top-down material machining and finishing.

The top-down method covers the steps taken to create the intended structure via mechanical or chemical means, starting with huge pieces of material. Chemical reactions that use atoms or molecules as their building blocks to create nanoparticles, nanorods, nanotubes, thin films, or layered structures are known as bottom-up processes. The well-known Moore's law, which was predicted in 1965. It states that “the dimension of a device halves approximately every 18 months and today’s transistors have well fallen in the nanometer range” [4]. In fact, Gordon Moore discovered in 1965 that between 1958 and 1965, the number of components in integrated circuits had doubled annually. The doubling duration then extended from a year to roughly 18 to 24 months. For instance, the 64 KB memory size 8080 microprocessor, which was first launched in 1974, included 4500 transistors. In contrast, the 2011 10-Core Xeon has 2.6 billion transistors, and the 2008-released Intel I7 Quadcore has 731 million transistors.

1.1.1 Natural and artificial nanoparticles

Today, nanotechnology and its many products are pervasive and play a crucial role in our products and way of life. These products range from shower stalls, bath tubs, and sinks to nanoscopic particles with better release qualities in medicines. Nanomaterials are broadly classified into natural and artificial nanomaterials.

Natural nanostructures are abounding in nanomaterials, and scientists are investigating their characteristics and potential applications. Natural nanomaterials include proteins and chitin (insects and crustaceans shells) as well as organic structures such as wing ribs and epidermal projections. Clays, carbon - containing soot (think carbon black), and natural inorganic thin films are also belonging to natural nanomaterials. As a result of these structures, nature demonstrates a wide range of behaviours, such as butterfly iridescence, surface wettability, and gecko foot adhesiveness. Some of the examples of natural nanomaterials are discussed below:

- The Lotus leaf is evidence of a surface capable of self-cleaning due to chemical and physical factors at the micro and nanometer scale.
- Nepenthes pitcher plant walls are so slippery that insects roll down and are devoured by juices pitcher plant at the bottom of the blooming. Because of its hydrophilic surface chemistry and surface roughness, the plant's rim is entirely wettable. These characteristics keep the insect's adhesive pads from making touch with the surface and causing it to slide down the plant.
- We all know that pigments are responsible for the colors we see, but nature has another way of producing color, which we call structural color. Some insect wings have hexagonal-packed array structures comprised of chitin that are organized. Wings can function as antireflective and self-cleaning coatings, give mechanical strength, improve aerodynamics, and serve as a diffraction grating that creates iridescence due to the wide range of spacing (from 200 to 1000 nm) between these structures.
- Nacre, the iridescent mother-of-pearl created by molluscs, is one of nature's hardest materials. Nacre is formed when mollusks deposit amorphous calcium carbonate ($CaCO_3$) onto porous layers of polysaccharide chitin. The mineral then crystallizes, forming stacks of $CaCO_3$ separated by organic material layers. Its strength is attributed to the molecules' brick-like construction (interlocking).
- The surface of a moth's eye features very minute bumps. They are hexagonal in shape and spaced a few hundred nanometers apart. Because these patterns are smaller than the visible light wavelength (350-800nm), the eye surface

has very low reflectance for visible light, allowing the moth's eye to absorb more light. Because these nanostructures absorb light so well, the moth can see far better than humans in dim or dark surroundings.

We are aware that nature is capable of creating a variety of intricate nanoscale structures, and researchers are currently examining the natural world to discover its nanoscale secrets. These same intricate structures are being produced using nature as a model.

Artificial nanomaterials are those that have been purposefully designed and synthesized by humans to possess specific desired features. Few examples of artificial nanomaterials are metal oxides, carbon-based materials, metallic, non-metallic particles, composites and ceramics.

1.1.2 Classification of nanomaterials

Nanomaterials are categorised according to the materials utilised in the synthesis process, the origin of the materials, and the structure or dimension of the nanomaterials. Figure 1.4 shows the classification of nanomaterials on different basis.

Siegel classified nanomaterials on the basis of their number of dimensions. According to him, nanomaterials are classified as zero-dimensional, one-dimensional, two-dimensional and three-dimensional nanomaterials which are shown in figure 1.3.

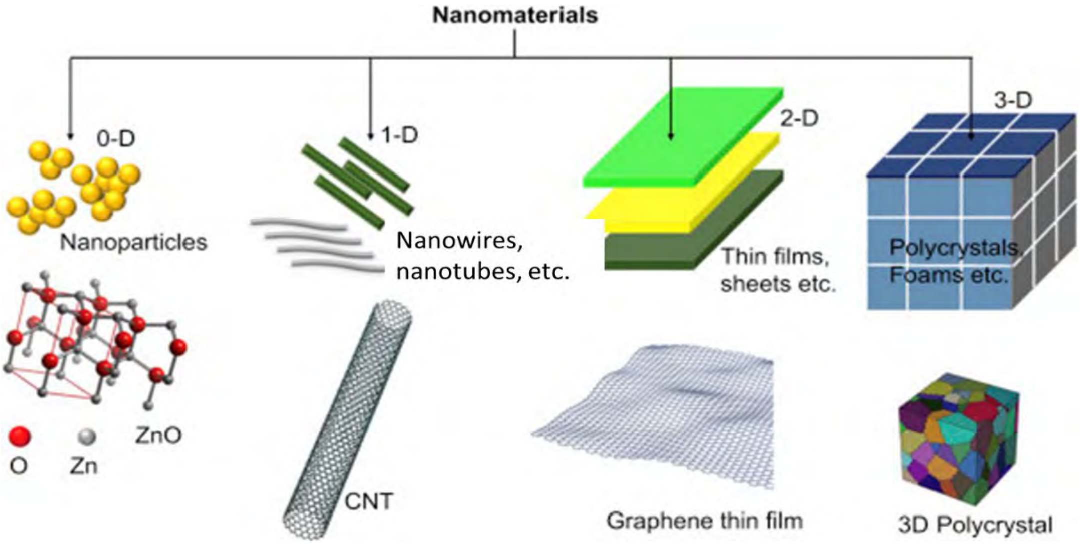

Fig. 1.3 Classification on the basis of their dimensions.

i) Zero-dimensional nanomaterials (0-D): All dimensions in 0-D nanomaterials are measured at the nanoscale (no dimensions are larger than 100 nm). 0D nanomaterials are typically nanoparticles and nanoclusters. They are also referred to as artificial atoms (or quantum dots) due to the discrete nature of their energy states. Silver and gold nanoparticles are examples of metallic nanoparticles, whereas CdS, CdSe, and CdTe quantum dots are examples of semiconductor nanoparticles. Nanoparticles can be spherical, cubic, or polygonal in shape and range in size from 1 to 100 nm. Kroto and his co-workers found fullerene as the most typical example. The smallest and most stable structure is fullerene (C_{60}), which has a high degree of symmetry. C_{60} has 60 carbon atoms in it. The C_{60} molecule, sometimes known as the "soccer ball molecule," has the appearance of a soccer ball. This molecule is made up of 20 hexagons and 12 pentagons with carbon atoms at its vertices [4].

ii) One-dimensional nanomaterials (1-D): In 1-D nanomaterials, two dimensions are in nanoscale and one dimension is out of nanoscale. Some examples of 1-D nanomaterials are nanotubes, nanorods, nanofibers, carbon nanotubes (CNTs) and nanofibers (CNFs).

ii) Two-dimensional nanomaterials (2-D): Here one dimension is in nanoscale range and the other two are outside the nanoscale. One of their dimensions is nanometer-scale, while their other two dimensions are significantly larger than their third dimension (i.e., thickness). Graphene, nanoclays, nanosheets, nanofilms, platelet-like structures, nanoflakes, and silicate nanoplatelets are a few examples.

ii) Three-dimensional nanomaterials (3-D): These materials have no dimensions that fall inside the nanoscale range. They are typically referred to as nanocrystals or equiaxed nanoparticles. The best illustration is the nanostructured bulk, which is made up of tiny blocks that range in size from 1 to 100 nm. Bulk nanomaterials, which are not confined to the nanoscale in any dimension, are another name for 3-D nanomaterials. All three of these materials' diameters are greater than 100 nm.

Nanomaterials are again classified into four types for better understanding. They are listed below:

i) Carbon based nanomaterials

ii) Metal based nanomaterials (Inorganic based nanomaterials)

iii) Dendrimers (Organic based nanomaterials)

iv) Composites

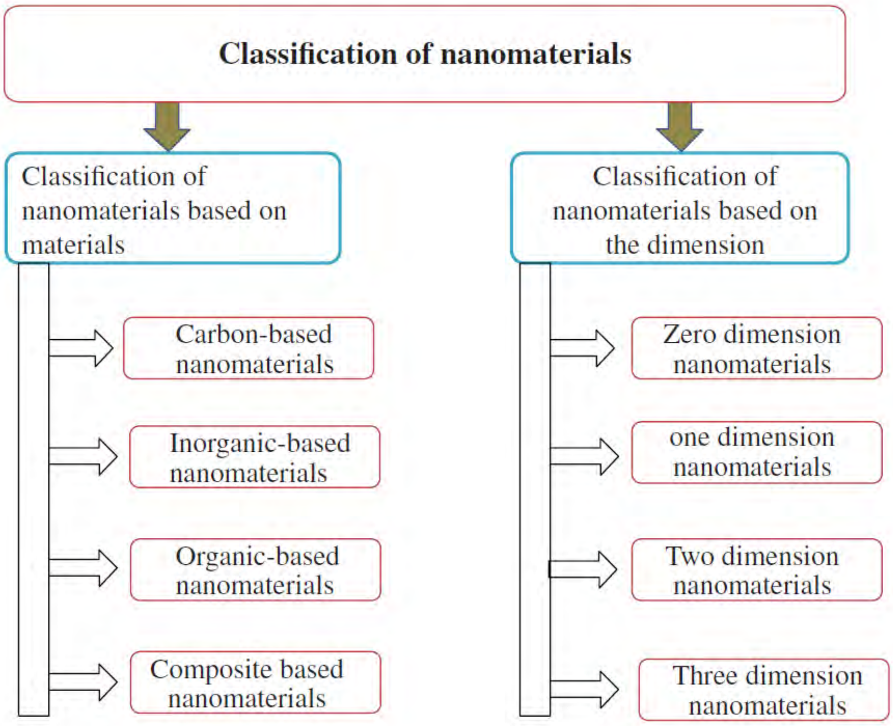

Fig. 1.4 Schematic diagram of classifications of nanomaterials.

i) Carbon based materials: These particular nanoparticles include carbon content and morphologically diverse materials can be seen. Carbon-based nanomaterials include spheres or hollow tubes, carbon nanofibers, graphene and Fullerenes.

ii) Inorganic based nanomaterials: Metals and metal oxides nanomaterials come in this group. Metals such as Au, Ag and Fe can be used to prepare them, as can metal oxides such as TiO_2, ZnO, and MnO_2. Silicon and ceramic materials are also used to prepare semiconductor nanoparticles.

iii) Organic based nanomaterials: Organic nanomaterials are composed of organic matter other than carbon and inorganic stuff. These nanomaterials are created via self-assembly or transformation of biological substances into the desired structure. In these materials, the noncovalent (weak) interaction is present.

iv) Composites: Composite nanomaterials are composed of an additional layer of nanoparticles. These nanomaterials are mixed with other nanoparticles, bulk materials, and more complex materials, such as metal frameworks. Composites can be manufactured from a variety of materials, including metal, ceramic, organic, inorganic, carbon-based, or bulk polymers. Depending on the synthesis and required qualities for the targeted applications, these materials have diverse morphologies.

1.1.3 Properties of nanomaterials

When nanomaterials are broken down to the nanoscale level, their characteristics undergo a dramatic change. The quantum size effect modifies the electrical characteristics of materials as we progress from the molecular to the nanoscale level. The increase in surface area to volume ratio at the nanoscale level causes changes in the mechanical, thermal, and catalytic properties of the materials. In comparison to bulk materials, nanoparticles have a larger surface area, high surface to volume ratio and several distinctive features. Different properties are used to define nanoparticle’s characteristics which are discussed here:

i) Electrical properties: Because of increased surface scattering, electrical conductivity drops with decreasing dimension [5]. It is possible to synthesis nanomaterials with desired electrical conductivity. In ceramics, the electrical conductivity decreases with increase in the size of nanomaterials and in metals, electrical conductivity increases with increase in the size of nanomaterials. Many insulator materials begin to behave as conductors at nanoscale scales. Similarly, as we go closer to the nanoscale size, we can see a lot of interesting quantum and surface phenomena. For example, silicon at bulk behaves like a semiconductor and the same material at nanoscale behaves like an electrical conductor.

ii) Thermal properties: The melting point of a crystalline substance is the temperature at which atoms, ions, or molecules shift from their periodic ordered form to the disordered state. Several studies show that the melting point of metals such as In, Sn, Pb, Bi, Cd, Al, Ag, and Au lowers as their size decreases, especially below 30 nm. Melting begins at the material's surface and is characterised by enhanced mobility of atoms or molecules in the top surface layers [4].

A material's specific heat is intimately related to its vibrational and configurational entropy, which is heavily influenced by nearest-neighbour configurations. The heat capacity of nanopowders is approximately 1.2-2 times greater than that of bulk materials in the temperature range of $10\ K \leq T \leq$ Debye temperature. The greater surface area of the nanopowders contributes to their increased heat capacity [4].

iii) Mechanical Properties: A material's elastic modulus is proportional to the strength of its atomic or molecular bonds. The elastic modulus increases as the bond strength increases. Typically, the elastic behaviours of crystalline materials are thought to be microstructure independent. A significant rise in vacancy and defect concentration, on the other hand, is projected to reduce the elastic modulus. The elastic modulus of nanoparticles was found to be lowered by 30% to 50% when compared to bulk materials due to very high fault concentration. The presence of a considerable volume percentage of grain boundary with a thickness of 1 nm or more is responsible for the significant decline in elastic modulus of nanocrystalline materials.

Hardness and strength: Plastic deformation of crystalline solids is attributed to dislocation movement. In polycrystalline materials, grain boundaries hinder dislocation migration. When the grain size of a given material decreases, the volume fraction of grain boundaries increases. This will increase the hardness and strength [4]. Mechanical properties like hardness, elasticity, adhesion, friction improves as the material size decreased to nano level [6].

iv) Magnetic properties: Materials are classed into diamagnetic, paramagnetic, and ferromagnetic based on their response to an external magnetic field. Nanomaterials are more magnetic than bulk. For example, sodium, potassium are paramagnetic at bulk and they become ferromagnetic at the nanoscale. Iron, nickel, cobalt are ferromagnetic at the bulk and at nano level they become super paramagnetic.

v) Optical properties: The optical characteristics of nanoparticles with sizes smaller than 10-15 nm, which is much smaller than the wavelength of light, are affected by size effects. The energy of interatomic interactions is high in semiconductors. The production of a weakly bound electron-hole pair, known as the Mott-Vanie exciton, may result from the electronic excitation of a semiconductor crystal [4]. The region of delocalisation of these excitons is far larger than the semiconductor's lattice constant. When a light beam incident on the surface of a material, it is either absorbed or scattered. Each of these phenomena is significant for a specific size of nanomaterial. This may result in different colour for particles of different size. Opaque substances at the bulk level become transparent at nano level. Copper shows this behaviour. Gold nanoparticles of different size show different colour.

vi) Structural properties: Nanomaterials have high surface to volume ratio. Atoms on the material's surface are generally more reactive than those in its center. Greater surface area suggests that the substance is more reactive. On a large scale, forces of attraction between surfaces may appear to be weak, but at the nanoscale, they are powerful. This could alter the surface morphology of crystal structures.

vii) Chemical properties: Nanoparticles' chemical characteristics are crucial. The stability, sensitivity, toxicity, corrosive and anti-corrosive, oxidation, reduction, antifungal, antibacterial, and disinfectant are some of the chemical properties of nanomaterials. The function of nanomaterials in chemical and biological engineering is determined by their chemical characteristics.

The most striking example of this is gold, which is the prototypical inert substance in its entirety. This is one of the factors contributing to its high value because it has a timeless quality and doesn't tarnish or corrode. Gold can be a potent catalyst when it is in the form of nanoparticles with diameters smaller than roughly 5 nm, notably for the oxidation of carbon monoxide (CO) [6].

1.1.4 Applications of Nanomaterials

Due to their interesting and advantageous characteristics, nanomaterials have a diverse range of applications. These are a few of them. [3]:

- Energy storage devices
- Defence and space
- Food and agriculture Industry
- Sensing
- Catalysis and degradation
- Medicine and drug delivery
- Water purification

- Hydrogen storage
- Electronic devices and technology
- Environment: to clean air
- Paints and other coatings
- Fabrics
- Cosmetics and consumer goods

The main advantage of using nanomaterials and nanotechnology in many applications are durable, lightweight, precise, stronger, less cost, more efficient, small size devices, faster.

1.2 Transition metal oxides

Electrochemical characteristics of the electrode material that are morphology dependent determine how well emerging energy storage technologies like supercapacitors and batteries perform. Transition metal oxides typically have distinctive morphologies that have an impact on how they are used in various energy applications. The several oxidation states of transition metal oxides make them promising electrode materials.

Since they exhibit many oxidation states for the redox reaction, transition metal oxides are thought to be ideal as the electrode materials for pseudocapacitors. These oxides provide quick electrochemical faradaic reactions between the electrode materials and electrolytes and store energy as electrostatic carbon compounds. The transition metal oxides used in electrochemical applications have the following characteristics: i) the oxide that is electrically conductive; (ii) the metal should continue to exist over a wide variety of oxidation states without going through any phase shifts that cause irreversible alterations to the 3D structure; and iii) protons and other cations, such as Na^+ and Li^+, can intercalate in and out of the oxide lattice during reduction and oxidation, enabling the simple interlinking of $O_2^- \leftrightarrow OH^-$. The electrolyte ions, generally OH^- or H^+ from electrode-solution travels into the interface under the electric field during charging and continues the electrochemical reaction.

i) NiO: Among all metal oxides, nickel oxide (NiO) has gotten a lot of interest because of its high theoretical specific capacitance of 2573 Fg^{-1}, huge surface area, low cost, good redox activity and environmentally friendly. People have previously prepared NiO with various architectures such as nanoflowers, nanoparticles, nanoplates, and mesoporous. Furthermore, electron transformation from bulk to nano porous or hollow structures has been reported to efficiently relieve strain caused during the ion insertion/desertion process, resulting in increased cycling performance. However, due to its low conductivity, pure NiO is unsuitable for applications requiring rapid electron transit. As a result, conductive additive materials like carbon nanotubes or graphene are commonly employed to increase the conductivity of electrode materials [7].

ii) CuO: Due to its non-toxicity, low cost, and earth abundance, CuO has attracted a lot of interest among potential metal oxides proposed for supercapacitor applications. CuO has been investigated as a potential electrode material for supercapacitors in a variety of geometries, but due to its smaller surface area and low electrical conductivity, it has a low specific capacitance. Many researches improved the efficiency of CuO-based supercapacitors by using compound mixes and different geometries of CuO nanomaterial. Graphene/CuO is one possible compound mixing combination. Due to excellent conductivity and high surface area of graphene, the combination of graphene with CuO will show a good result [8].

iii) ZnO: Due to its natural abundance, low cost, and environmental friendliness, ZnO has recently been explored as a viable contender for supercapacitor application, much like other metal oxides. ZnO's weak electrical conductivity, however, continues to be a significant issue and restricts rate capability for high power performance, impeding its widespread use in an energy storage system. Graphene and ZnO hybridization provide a potent method for obtaining high specific capacitance [9].

iv) Co_3O_4: A transition metal oxide with intriguing electrical, optical, electrochemical, and electrocatalytic properties is cobalt oxide (Co_3O_4). Co_3O_4-based nanocomposites have shown considerable promise in the field of supercapacitors because of its extremely high theoretical specific capacitance of 3560 Fg^{-1}[10], good conductivity, chemical durability, good corrosion stability, diverse morphology, excellent reversible redox reactions [10].

1.3 Carbon allotropes

Carbon is a light, simple element having just six electrons in each atom, two of which are core (1s) electrons and the remaining four (2sp) electrons accessible for bonding with other atoms. Carbon's naturally diverse forms are due to the slightly schizophrenic character of its chemical bonding by these four. It is the fourth most abundant element in the universe and the fifteenth most abundant element in the crust of the earth. It is an element in the periodic table with isomers ranging in dimension from zero to three. It is intriguing because sp^2 hybridization produces diverse nanoforms of carbon, including graphene, a single-atom thick 2D graphite. A special position has been reserved for carbon nanomaterials in nanoscience because of their remarkable thermal, electrical, chemical, and mechanical characteristics. Strong composite materials, energy storage and conversion, supercapacitors, smart sensors, gas sensors, targeted medication delivery, field emission devices, quantum wires, catalyst support, nanoelectronics, and paints are just a few of the many fields in which they have been used [11].

1.3.1 Graphite

Carbon can exist as crystalline or amorphous matter. Under normal conditions, all carbon allotropes are solid, with graphite being the most thermodynamically stable. Graphite is a carbon allotrope consisting of layers of hexagonally arranged carbon atoms in a planar condensed ring system which is shown in figure 1.5. Under normal circumstances, graphite is the most stable form of carbon and it occurs naturally. It is a poor conductor of both electricity and heat.

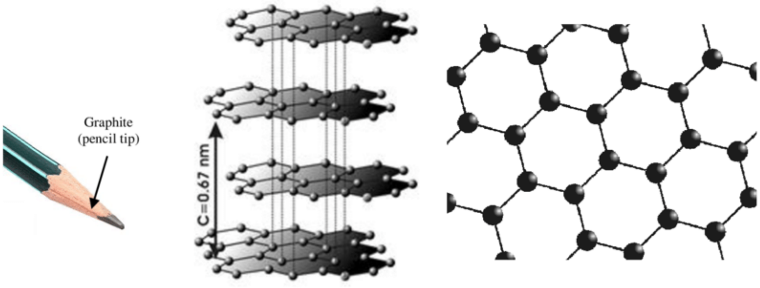

Fig. 1.5 Molecular structure of graphite.

The carbon atoms in graphite are organised in a hexagonal ring form. It is made up of graphene sheets, which are enormous molecules with incredibly strong covalent bonds. Orbits made up of two 2p orbitals and one 2s orbital ($2p_x$ and $2p_y$). In graphite, every carbon atom is sp^2 hybridised. Between the carbon atoms in the plane, this will create the bonds, which are known as strong covalent σ bonds. This strong covalent bond between carbon atoms in the plane are known as bonds. The graphite structure's weak bonding between adjacent layers is provided by the unmixed pure p_z orbital, also known as the π-orbital, which is perpendicular to this plane. Van der Waals bonding is another name for this flimsy interlayer connection. The network of carbon-carbon double bonds in a particular plane is explained by the overlap of the π-orbitals on nearby atoms, which also responsible for graphite's high electron mobility [11]. This is shown in the figure 1.6.

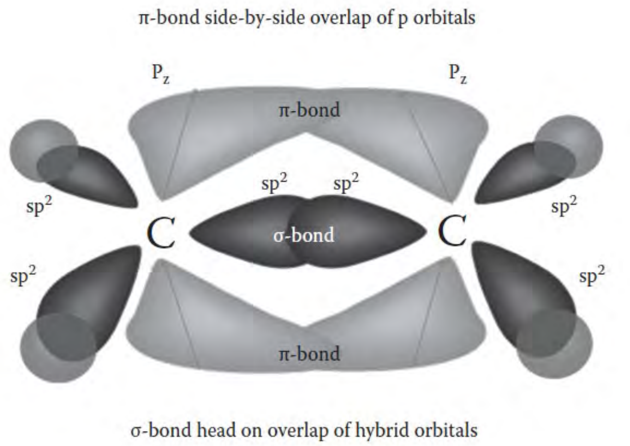

Fig. 1.6 Schematic diagram of hybridization of orbitals in graphite (Taken from ref. 11).

1.3.2 Graphene: Structure and properties

Prior to the isolation of monolayer graphene in 2004, it was thought that two-dimensional compounds could not exist because of thermal instability when separated. However, after graphene was separated, it was evident that it was possible, but scientists needed some time to figure out exactly how. Graphene has theoretically been studied for many years, but it was assumed that planar 2D graphene did not exist in a free form since freestanding graphene was thought to be thermodynamically unstable. In the year 2004, Sir Andre Konstantin Geim (physics) and Sir Konstantin Sergeevich Novoselov (physicist) collaborated on a simple but effective method for exfoliating a single layer of highly orientated pyrolytic graphite using ordinary scotch tape. The discovery of such remarkable material was honoured with the Nobel Prize in Physics in 2010. As a result, graphene has been identified as the origin of all graphitic forms, including graphite (3-D), carbon nanotubes (1-D), and buckyballs (0-D) [12].

Graphene a wonder material is essentially a single atomic layer of graphite, which is an allotrope of carbon composed of very closely linked carbon atoms arranged in a hexagonal lattice. It is a single-atom thick structure of sp^2-hybridized carbon atoms that are densely packed in a honeycomb crystal lattice**.** The figure 1.7 illustrates the structure of graphene. Graphene has recently sparked the interest of researchers in energy-storage systems due to its unique features, which include high electrical conductivity, high mechanical strength, extremely thin atomic thickness (of 0.345 nm) and a large specific surface area [7].

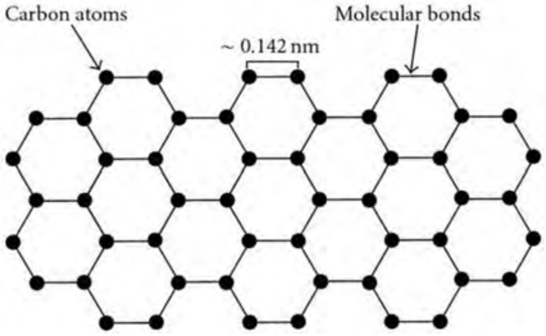

Fig. 1.7 Schematic representation of structure of graphene.

Graphene can be synthesized by different methods: Mechanical exfoliation by scotch tape method, Chemical exfoliation, reduction of graphene oxide, chemical vapour deposition and dry ice method [4]. Among this, we have followed reduction of graphene oxide. Because of its ability to convert graphene, scalability and low cost.

Properties of graphene: Since 2006, pristine graphene has revealed a number of intriguing features, leading to the development of several methods. The C-C bond length in graphene is 0.142 nm, with a strong binding in one layer but poor bonding between layers. A single sheet of graphene has a specific surface area of ~2630 m^2g^{-1} (Stoller et al., 2008). With a band gap value of ~0-0.25 eV, graphene has exceptional optical characteristics (> 97.7% transmittance) (Zhang et al., 2009). Other intriguing characteristics include a high Young's modulus (1.0 TPa) and a high carrier mobility (200,000 cm^2/Vs) (Geim and Novoselov, 2007). Because of its exceptional conducting capabilities, graphene and its composite materials can be used as semi-conductors. Enoki et al. (2005) explored the special magnetic behaviour of nanographene for potential applications in electrical and magnetic devices, including spin glass states, magnetic switching, and edge-state spin gas probing. Brief experimental research on the impact of isotopes on the thermal characteristics of graphene were published by Chen, S. et al. (2012), who discovered that the ratios of ^{12}C and ^{13}C are crucial for graphene's thermal conductivity (Chen, S. et al., 2012). Because of all these remarkable qualities, graphene is readily used in practical applications [13].

Applications of graphene:

The world's thinnest substance, graphene has a very high surface-to-volume ratio. The application of graphene in batteries and supercapacitors is therefore extremely promising. Batteries, supercapacitors, and even fuel cells may be able to store more energy and charge more quickly due to graphene. The advantages of using graphene in supercapacitors are high capacitance retention, fast charging, light weight, flexibility and high temperature range. Other applications are also listed below:

- Solar cells and fuel cells
- Transistors
- Waterproof electronics

- Touchscreens and flexible screens
- Hard drives and memories
- Elastic robots
- As a superconductor
- Optoelectronics
- Optical and security sensors
- Medicine and drug delivery
- Cancer treatment
- Food packing
- Water purification
- Crop protection
- Food security
- Coatings and sensors etc.

1.3.3. Graphene oxide

Benjamin Brodie documented the synthesis of graphite oxide (GO) for the first time in a short note published in Annales de Chimie in French in 1855 several years before graphene was discovered. He developed a method for producing graphite oxide. It involved the oxidation and exfoliation of natural crystalline graphite, which resulted in a significant amount of single layer graphene oxide. Unfortunately, no one knew about graphene at the time. Only after more than a century and a half after "The Rise of Graphene" was the ancient idea rediscovered as an efficient and low-cost method of producing the new fascinating and promising material [14].

Similar to graphite, graphite oxide too has a layered structure, but the oxygen-containing groups that decorate the plane of carbon atoms greatly increase the interlayer distance and make the atomic-thick layers hydrophilic. These oxidized layers may exfoliate in water when subjected to ultrasonic agitation. Graphene oxide is the name given to the exfoliated sheets if they only contain one or a few layers of carbon atoms, like graphene. [13]. The schematic representation of GO is shown in figure 1.8.

Because of the low cost and simple transformation from graphene oxide to graphene, graphene oxide (GO) is an intriguing material. The carbon layers are subsequently separated into single- or multiple-layer graphene by reduction. The most current techniques for producing GO rely on the apparent intercalation capacity of layered graphite. It increases the distance between flat carbon layers of crystalline graphite, allowing atoms of active metals and some types of oxidation agents to pass through, while also changing the surfaces of the layers with chemically bound functional groups. Finally, the complete disassembly of the graphitic crystal into distinct carbon monolayers with chemically changed surfaces is brought about by the action of suitable oxidising agents [15].

Strong acids (nitric and/or sulphur) and potassium chlorate are used in the synthesis of graphene oxide (by Brodie, Staudenmaier, and Hoffman). The most widely used Hummers—Offeman method employs a solution of concentrated H_2SO_4, $NaNO_3$, and $KMnO_4$. It produces a higher yield in less time than prior approaches [15].

Modified Hummers method has been implemented to prepare graphene oxide (GO). This approach yields a greater proportion of well-oxidized hydrophilic carbon material with a more uniform structure and a less disturbed basal plane of graphite. GO is made up of epoxy (C-O-C) trigonally bound in sp^2/partially sp^3 configurations, hydroxyl groups (-OH) shifted above or below the graphene plane, and certain carboxylic groups (-COOH) near the graphene plane's borders. Because of its unique

2-D structure and the inclusion of multiple oxygenated functional groups, GO has exceptional mechanical, optical, thermal, and electrical capabilities similar to graphene. GO, on the other hand, has a high sheet resistance of ~10^{12} Ω /cm^2. The presence of C-O-C and C=O groups in GO contributes to its intrinsic insulating characteristic. Chemical and heat treatments are necessary to reduce GO and eliminate these oxygen groups, resulting in an increase in electrical conductivity. The resulting product is referred to as a reduced graphene oxide (rGO) [4].

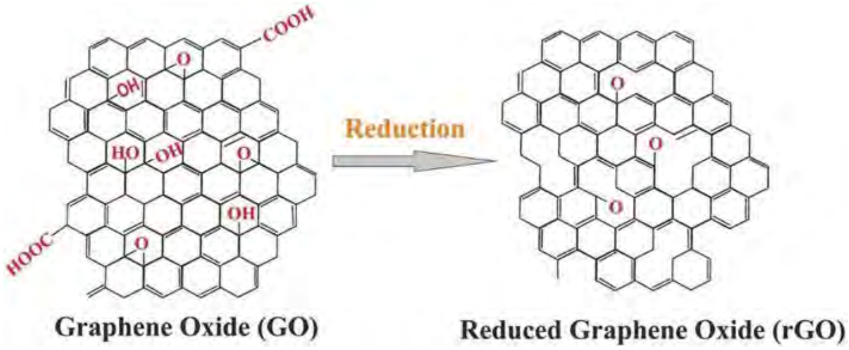

Fig. 1.8. Schematic representation of GO and rGO

One of the benefits of GO is how easily it disperses in water and the existence of oxygen functionality allows for the employment of other organic solvents as well as in other matrixes. This still holds true when combining the substance with ceramic or polymer matrixes to enhance their electrical and mechanical capabilities. However, due to the destruction of its sp^2 bonding networks, GO is sometimes referred to as an electrical insulator in terms of electrical conductivity.

1.3.3a Reduced graphene oxide (rGO)

Reduced graphene oxide is a form of graphene oxide (GO) that has had its oxygen content reduced through chemical, thermal, and other techniques. The schematic representation of structure of rGO is shown in figure 1.8. Because of the high surface reactivity of GO particles, a considerable portion of oxygen-containing functional groups can be easily removed from the basal plane. Multiple studies proposed the widest range of approaches for GO restoration. Existing techniques of converting GO to graphene can be categorised into three categories: physical (thermal), chemical, and hybrid, in which physical and chemical factors coexist [15].

Reduction is the well-known and visible reaction in which GO can be involved. The colour of the GO solution changes instantly from yellow brown to black, indicating the restoration of the conjugated sp^2 network and the development of the graphitic structure. Typical GO, on the other hand, never entirely restores the original graphene network. This is due to the fact that GO is already severely defective: existing flaws cannot be repaired during the reduction. After reduction, two types of species remain on the rGO planes: i) holes and (ii) certain oxygen functions [14].

i) Due to the loss of carbon atoms in the form of carbon dioxide, holes formed on GO planes throughout the production process.

ii) After chemical reduction, the oxygen functions that remain on GO are primarily carbonyls. Carbonyl groups cannot be easily reduced, but epoxides and tertiary alcohols are more or less successfully reduced. The production of carbonyls requires the breakage of C-C bonds. These defects are irreparable.

The most often used technique for reducing GO is the chemical approach. Hydrazine, borohydrides, and hydroquinone are the most often used reducing agents. However, this method's main disadvantage is that the chemicals utilised are hazardous, extremely toxic, corrosive, and flammable. Therefore, results are not encouraging for GO decrease. Green synthesis to reduce GO is of interest as a means of avoiding the use of toxic and environmentally hazardous reducing chemicals. Reducing agents include amla, clove, cinnamon, spinach, caffeine, baking soda, carrot root etc [16-24].

1.3.3 Applications of GO and rGO

GO and rGO are very useful and promising materials for many applications. Here is a list of few of them [13]:

1) Electronic devices: GO was used as a starting material for at least one component in the fabrication of several electrical devices. A graphene-based field effect transistor is one such device (FET). FETs based on rGO have been employed as chemical and biosensors. Functionalized rGO FETs have been employed as biosensors to detect the hormonal catecholamine chemicals avidin and DNA.

2) Energy storage devices: Due to their extraordinarily high surface area, GO and rGO are being evaluated for use as electrode materials in fuel cells, solar cells, batteries, and double-layered capacitors. GO production is simpler to scale up than other graphene compounds.

3) Biosensors: GO/rGO is a fluorescent substance that could be utilised for biosensing, early disease detection, and perhaps assisting in the discovery of cancer therapies and the detection of biologically relevant chemicals. GO has been successfully employed in fluorescent-based biosensors for the detection of DNA and proteins, promising improved HIV diagnosis.

4) Biomedical applications: GO is widely utilised in biomedicine, notably in drug delivery systems. Because it solely targets tumours but not healthy cells and has a low toxicity, GO is likely preferable to many other anticancer medications. Functionalized

nano-GO has been employed in various investigations on anticancer medication delivery.

5) Water purification: Water permeability via the membrane was attributed to GO structural swelling, which creates a water penetration channel between different GO layers. One atom thick GO layer allows water to "pop through the very, very small holes that are in the graphene and leave the salt behind." GO film has a permeability that is 100 times larger than the best competitive membrane on the market, despite being 500 times thinner than the strongest filter currently available in the market and ~1000 times stronger than steel. Ions from ordinary salts flow through the filter, but bigger ions are retained in the specimen.

6) Coating technology: rGO coatings that are totally impermeable to liquids, gases, and strong chemicals. Corrosive acids can be stored in glassware or copper plates that have been painted with this particular graphene "paint". To extend shelf life, medical packaging may use plastic films coated with graphene.

1.4 Supercapacitors

In today's world, electrical energy is critical to maintaining current living standards. Natural fossil fuel resources are depleting with each passing decade, so there is an urgent need for a shift to electric-powered vehicles and household consumption to address the future problems of everyday living. Furthermore, very high consumption of fossil fuels over the last few decades has resulted in catastrophic climatic changes due to the development of greenhouse gases, which can be avoided by shifting toward renewable energy generation, storage and utilization. Electrical energy is an extremely adaptable source of energy that may be used for transportation, as well as to power homes and industries, but it has a significant limitation in terms of storage, namely that it is rather difficult to store electric energy in a short period of time.

Fuel cells, batteries, solar cells, and supercapacitors are examples of well-known electrochemical energy storage systems. Among all these devices, supercapacitors have attracted more attention due to its high-power density, long cycle life, environmentally friendly, better reversibility and much safer than batteries [25-29].

Supercapacitors, also known as ultracapacitors or electrochemical capacitors (ECs), are charge storage devices that use the electrical double layer on the electrode/electrolyte interface to store charges. Their electrodes are typically made from large surface area materials with high porosity and good conductivity. Because of these features, supercapacitors can charge and discharge quickly, resulting in great power delivery in a short period of time, which has led to their increased application in portable devices.

1.4.1. History of Supercapacitors

Due to the fact that these technologies have been around for a while, recent trends reveal a growing demand for effective high energy density supercapacitors. In 1957, General Electric Corp. created the first supercapacitor based on an electrical double layer technology. Up until 1966, when scientists at the Standard Oil of Ohio Research Center (SOHIO) created the electrical double layer capacitor (EDLC), there had been little research done in this area. In their model, scientists created a supercapacitor using activated carbon electrodes dipped in an aqueous electrolyte on battery terminals. They took it a step further and tested organic electrolytes on the same system. In the year 1978, SOHIO was forced to licence its technology to Nippon

Electric Company (NEC) because there was no commercial activity in the supercapacitor field even as late as the early 1970s.

Although major manufacture did not begin until the 1980s, the device was first advertised as a "supercapacitor" for computer memory backup at NEC. With the advancement of technology, additional businesses such as Elna/Asahi Glass and Matsushita began making supercapacitors for watches, cameras, and portable gadgets. Around this time, they began producing organic electrolytes Dynacap EC for the US market. Elna/Asahi were the first to develop asymmetric capacitors using an electrical double layer electrode and a battery electrode to develop a high energy device.

During the 1990s, Panasonic produced their "Goldcap," and Maxwell Technologies produced their own versions called "Boostcaps." Since then, the latter has grown to be one of the top manufacturers of supercapacitors in the United States, where their impact can already be seen in the automotive and portable device industries. Recently, supercapacitor research has grown tremendously, with even more companies manufacturing their own variants [30].

1.4.2 Types of Supercapacitors

The importance of supercapacitors as an energy storage device grew considerably in the latter decade of the twentieth century, and considerable improvements were made in the sector. Several investigations [United States Pat., 1996] by Conway et al. and others have explored and identified the underlying chemistry, as well as created the model for charge storage. Supercapacitors are classified into three varieties based on their charge storage mechanism (shown in figure 1.9): electrochemical double layer capacitors (EDLCs, non-Faradic electrostatic storage) and pseudocapacitors (Faradic, redox reaction-based capacitors). Also, there is a type of supercapacitor called as a hybrid supercapacitor, which combines both storing techniques. Each class has a distinctive charge storage mechanism that defines it.

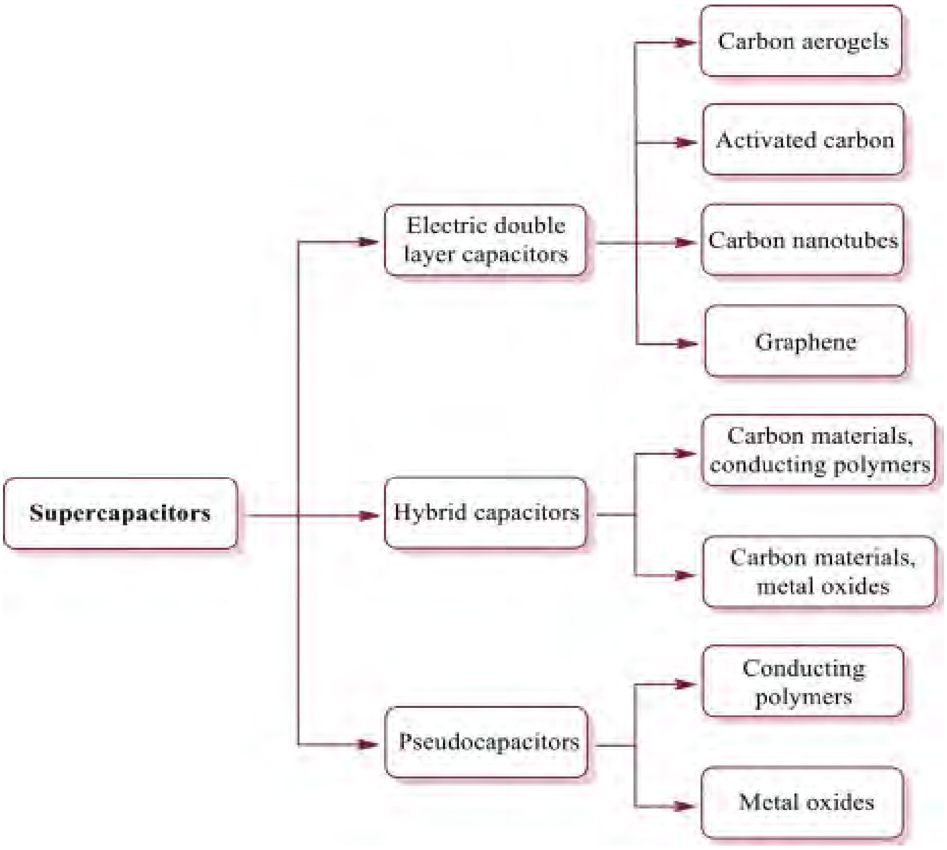

Fig. 1.9 Classification of supercapacitors.

Carbon-based materials are used for electrodes in Electric double layer capacitors (EDLC). Charges are not transferred between the electrode and the electrolyte in this case. Instead, charge accumulation will occur between the electrode and electrolyte interface, making charge storage highly reversible. As a result, the cycle stability improves, but the capacitance value is low. Pseudocapacitors, on the other hand, have a high capacitance but a low cycle stability due to continuous redox reaction. The combined use of EDLC and pseudocapacitor electrode materials has been shown to be an effective strategy for achieving high performance.

Transition metal oxides and conductive polymers are being carefully explored as potential materials for pseudocapacitors. Transition metal oxides have a high specific capacitance, and conducting polymers have a high intrinsic conductivity, making them a unique possibility for high-performance supercapacitors [31, 32]. Unfortunately, due to the repetitive swelling and shrinking of the polymer chains during the doping/dedoping process, conducting polymers have poor cycling-stability performance compared to metal oxides [33-36].

One of the most extensively researched metal oxides for usage in supercapacitors is hydrous ruthenium oxide (RuO_xH_y or RuO_2-xH_2O), which has a specific capacitance as high as 720 Fg^{-1}. This is because a variety of favourable properties such as high operating potential window, various oxidation states, highly reversible redox processes, high proton conductivity, good thermal stability, extended cycle life, metallic-type conductivity, and high-rate capability [37]. However, due to their high cost and environmental issues, alternative metal oxides such as manganese oxide, nickel oxide, cobalt oxide, zinc oxide, copper oxide and others have been favoured.

1.4.3 Principle, construction and mechanism of charge storage

i) EDLC: Electrochemical energy storage technologies have various advantages over other kinds of energy storage. For example, because they are not subject to Carnot constraints, they are more efficient, modular, and versatile, as evidenced by numerous recent publications on rechargeable lithium-ion batteries and microfuel cells (Frackowiak 2008, Shiraishi 2002, Lee 2010 and Morishita 2008). Furthermore, with increasing environmental contamination, electrochemical energy generation and storage will play a crucial role in reducing reliance on limited fossil fuel reserves.

Electrochemical capacitors work on the same principles as electrostatic capacitors. A typical capacitor consists of two conducting plates separated by a dielectric that store energy in the form of electrical charge. When an electric potential is supplied across the conductors, electrons begin to flow and charge accumulates on each conductor. When the potential is withdrawn, the conducting plates remain charged until they come into contact again, at which point the energy is discharged. The capacitance of a capacitor is the amount of charge that can be stored in relation to the strength of the applied potential. It is a measure of the capacitor's energy storage capability. The capacitance of a capacitor depends on the area of the plates and the separation distance between them and relation is given in equation (1.1)

$$C = \varepsilon \frac{A}{d} \quad \ldots\ldots\ldots\ldots\ldots\ldots \text{(1.1)}$$

Where C is the capacitance, A is the area of the plate, d is the distance between the two plates, ε is the dielectric constant. The energy stored in a capacitor is given in equation (1.2)

$$E = \frac{1}{2} CV^2 \quad \ldots\ldots\ldots\ldots\ldots\ldots \text{(1.2)}$$

Here V is the electric potential.

In a similar way, Supercapacitors also known as electric double layer capacitors store electrical charge. Instead of charge accumulation on two conductors separated by a dielectric, charge accumulates at the interface between a conductor's surface and an electrolytic solution (shown in figure 1.10). The collected charge thus forms an electric double-layer, with each layer separated by a few Angstroms. Helmholtz proposed the double-layer model in 1853, in which the double-layer consisted of two charge monolayers, can be used to estimate capacitance. The first layer formed on the charged electrode, and the second layer is made up of ions in the electrolyte.

A double layer capacitor is made up of two electrodes, a separator (ion permeable membrane) and an electrolyte. The electrolyte is a solution of positive and negative ions in water. A separator separates the two electrodes.

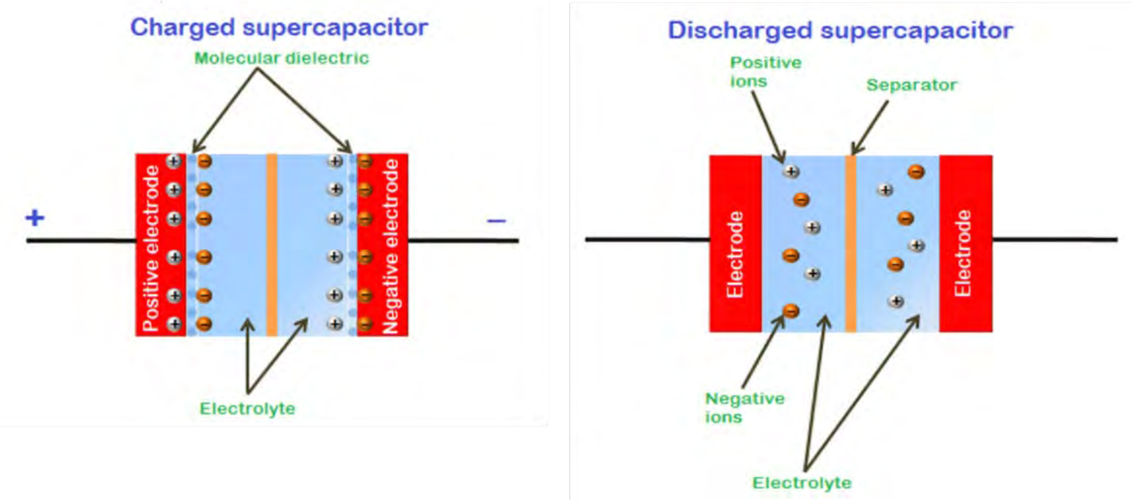

Fig. 1.10 Schematic representation of charged and discharged EDLC.

At the point where the electrode surface and electrolyte solution meet, opposite charges are formed. Each supercapacitor electrode generates two electric charge layers. One charge layer with one polarity (positive or negative) is created on the surface of the electrode, while another charge layer with opposite polarity is formed in the electrolyte solution near the electrode surface (negative or positive). A monolayer (layer one molecule thick) of solvent or water molecules separates these two charge levels.

The double layer capacitor begins charging when voltage is applied to it in such a way that the positive terminal of the battery is linked to the one side electrode and the negative terminal of the battery is connected to another side electrode. The positively charged electrode exerts a strong attractive force on the negatively charged ions in the electrolyte. As a result, negatively charged ions migrate toward the positively charged electrode. Similarly, the positively charged electrode exerts a significant attractive force on the positively charged ions in the electrolyte. As a result, positively charged ions migrate toward the negatively charged electrode. An electrical double layer forms at the interface of the electrode and the electrolyte, stores energy. In a typical setup, the composition of the electrolyte, the morphology of the electrode, and the voltage across the two electrodes all influence the nature of this double layer, which in turn influences the capacitance of the electrode. The total capacitance is the result of two capacitors in parallel given in equation (1.3)

$$\frac{1}{C} = \frac{1}{Ca} + \frac{1}{Cb} \quad \ldots\ldots\ldots\ldots\ldots \text{(1.3)}$$

ii) Pseudocapacitors: Pseudocapacitors are another category of supercapacitor that use the Faradic or reversible redox reaction to store energy. When an atom loses an electron, it gets oxidised, becomes more positive. When an atom gains an electron, it gets reduced, becomes more negative.

Redox processes occur at the surface of the electrolyte and are divided into three categories: i) underpotential deposition (adsorption pseudocapacitance), ii) redox pseudocapacitance, and iii) intercalation pseudocapacitance. When two-dimensional Faradic processes involve reversible adsorptions and removal of atoms from metal surfaces, underpotential deposition results. When reversible redox processes occur at the electrode surface, redox pseudocapacitance occurs. Ions are electrochemically intercalated into the structure of redox materials in the case of intercalation pseudocapacitance.

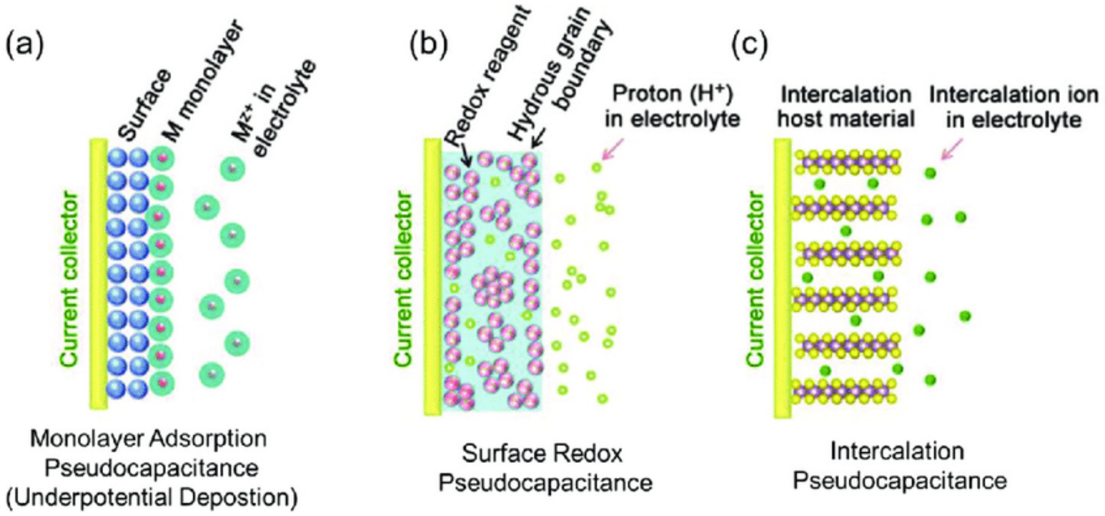

Fig. 1.11 Schematic representation of pseudocapacitors

The charged atoms or ions in the electrolyte flow toward the electrode that is oppositely charged when voltage is supplied to the pseudo-capacitor. Two electric layers, or electric double layers, are created between the electrode's surface and the nearby electrolyte. Electrolyte molecules stand between these two electric levels. Along with the capacitance that results from the double-charge layer's separation, reactions that can take place on the electrode's surface can also contribute to capacitance. The charge necessary to promote this redox reaction at the interface of electrode and electrolyte depends on the potential. The schematic diagram of mechanism of charge storing of a pseudocapacitor is shown in figure 1.11.

Electrolytes

Along with the two electrodes, an electrolyte also contributes significantly to the functioning of the capacitor by its effects on ion supplementary, electric charge conduction, and electrode particle adhesion. There are three categories of electrolytes for supercapacitors, namely i) Aqueous electrolyte, ii) Organic electrolyte and iii) Ionic electrolyte.

The electrolyte used in a supercapacitor is just as essential as the electrode material. The attainable cell voltage of a supercapacitor will be determined by the electrolyte's breakdown voltage, and thus the possible energy density (which is voltage dependant) will be restricted by the electrolyte. The power density of a cell is heavily influenced by electrolyte conductivity.

Aqueous electrolytes have a small voltage window as low as 1.2 V, which is extremely low in comparison with organic electrolytes, organic electrolytes are frequently advised. But organic electrolytes, which are thought to be less conductive, more expensive, usually flammable, and more toxic. Aqueous electrolytes (such as KOH, NaOH, H_2SO_4, Na_2SO_4 etc) have the advantages of high-ionic conductivity, low cost, non-flammability, non-corrosiveness, safety, and convenient assembly in air. Ionic liquids electrolytes are also used to make a variety of electrodes and devices.

Separator

The separator inhibits electrical contact between the two electrodes, but it is ion-permeable, allowing for ionic charge transfer. The separator should have a high electrical resistance, a high ionic conductivity, and a low thickness for optimal supercapacitor performance.

Energy density and power density

The amount of energy per unit mass obtained from charged supercapacitor is the Energy density. The energy density can be calculated by equation (1.4)

$$E = \frac{1}{2m} CV^2 \quad \Longrightarrow \quad E = \frac{1}{2} C_s V^2 \quad \ldots\ldots\ldots\ldots\ldots\ldots (1.4)$$

Where E is the energy density (Wh Kg^{-1}), C_s= C/m is the specific capacitance in Fg^{-1}, V is the potential window in V.

The time rate of energy transfer per unit volume is the power density and it explains how rapidly the device's reserved energy can be transferred to an external load. It can be calculated by using equation (1.5)

$$P = \frac{E}{t} 3600 \quad \ldots\ldots\ldots\ldots\ldots\ldots (1.5)$$

Here P is the power density (W Kg^{-1}), E is the energy density (Wh Kg^{-1}) and t is the discharge time (s).

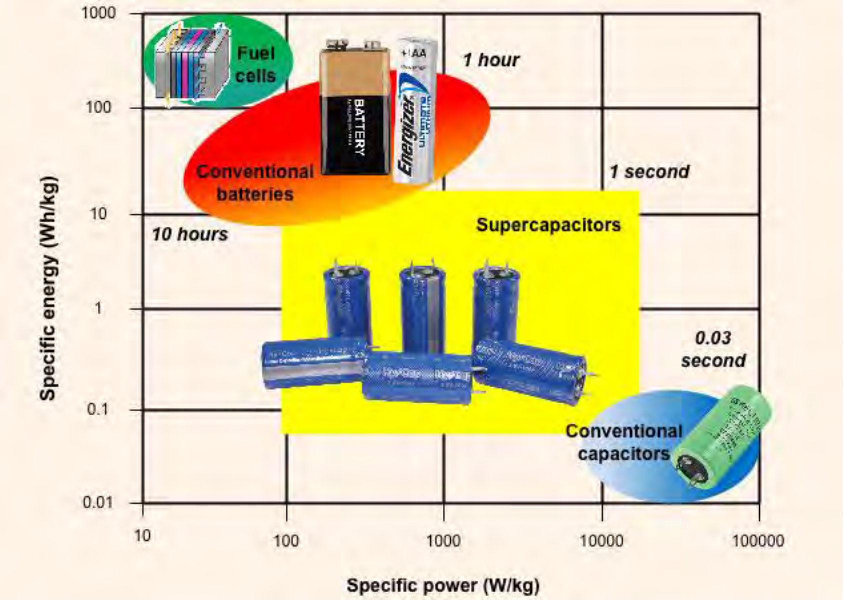

Fig. 1.12 Ragone plot of various energy storage devices

Supercapacitors have high power density but low energy density compared to that of battery. Figure 1.12 shows the graph of specific energy (energy density) versus power density (specific power) for various energy storage devices. This plot is called as Ragone plot. This shows the energy density and power density comparison of different energy storage devices. Supercapacitor bridged the gap between capacitors and batteries.

1.4.4 Applications of supercapacitors

Electrochemical supercapacitors are still a new technology that is not yet used extensively. This was initially a result of their low power and energy capacities, which limited their employment to low-power, low-energy applications like memory backup. However, major improvements in energy and power density have recently been accomplished, and EDLCs are finding more and more use in novel applications. The EDLC can be used as an energy storage component in the following scenarios [39, 40]:

- Backup power sources: In consumer appliances, supercapacitors have long been used as a temporary backup power source. It can be used as a backup power source in electronic boards, memory, and microcomputers. The primary power source in a backup power application will be a normal load.
- Memory backup: Nowadays, many appliances include digital parts with memory, so even a very brief interruption in the power supply would result in the loss of any data that has been saved. In these circumstances, a supercapacitor can serve as the power source for a brief amount of time while preserving data. Because of the long lifetime, EDLCs are an excellent choice for backup power supplies.

- Electric vehicles: In electric vehicles (EVs) and hybrid electric vehicles (HEVs), supercapacitors are used to supply high power for a short period of time and to store regenerative braking energy. This sort of supercapacitor application can reduce the number of batteries or the size of the internal combustion engine (ICE). The same type of combination can be used in ships and aeroplanes.

  The transportation industry is the largest market for supercapacitors. In India, BEST (Brihan Electric Supply and Transport) introduced emission-free electric buses at the end of October 2017. The motors generate back emf during braking. This return emf is used as regenerative energy to charge the supercapacitors. Supercapacitors, when paired with a battery, extend battery life while decreasing battery size. Buses in Shanghai employ supercapacitors as their only power source (it is recharged every third stop in 1-2 min with the help of regenerative energy being produced by braking). China has shown the rest of the world that this technology can be used on a massive scale.
- Power quality: EDLCs can be utilised as the energy storage device in systems aimed to improve power distribution reliability and quality. Such systems necessitate the use of a DC energy storage device from which energy can be extracted and stored.
- Battery improvement: A growing number of portable electronic gadgets, such as laptops and cell phones, use batteries as power sources. Many of these devices demand high-power, pulsed currents, and current profiles with short, high-current bursts reduce battery performance. Using supercapacitors in combination with a battery is thus the best approach.
- Electromechanical actuators (in Spacecraft and submarines): Electromechanical actuators can control thrust vectors for spacecraft launches or operate as flood-

control actuators on submarines. Most actuation systems require pulsed currents with high peak power but relatively low average power consumption.

- Remote power from renewable source: Remote power supply that get their energy from intermittent sources like wind or solar radiation require energy storage to ensure that energy is always accessible. In such cases, EDLCs provide several advantages over the typically used battery.

1.5 Motivation

Due to the rapidly expanding global economy, there exists few problems that are caused by a considerable increase in the usage of fossil fuels worldwide. The first one is the rapid consumption of existing fossil fuel reserves, and the second is the associated environmental issues, such as rising greenhouse gas emissions and general air and water pollution. These factors form the foundation of a widespread global concern about the future, sustainable growth, and health of our society's ecology. The critical need to develop and scale up sustainable, clean energy sources and associated technologies is acknowledged globally. To efficiently gather these intermittent energy sources, corresponding energy conversion and energy storage systems must be developed. Electrochemical supercapacitors are useful in this regard.

Objectives:

- Synthesis of GO, rGO, metal oxides and rGO/metal oxides composites.
- Characterization of the prepared samples.
- Electrode preparation.
- Electrochemical studies for all the prepared samples.

Methodology:

- Modified Hummer's method was implemented for the preparation of GO and reduction of GO has been done by using amla extract, followed green approach.
- Metal oxides (NiO, CuO, ZnO, Co_3O_4) nanoparticles were prepared by solution combustion method (SCM) with different fuel ratio.
- rGO/metal oxide nanocomposites were prepared by sonochemical method.
- Structural characterization of the synthesized samples was investigated by XRD, FTIR, Raman spectrometer, SEM, TEM and EDAX.
- Electrochemical measurements (CV, GCD, EIS) were done for all prepared samples.

References

[1] Vladimir Pokropivny, Rynno Lohmus, Irina Hussainova, Alex Pokropivnyl, Sergey Vlassov, *Introduction to nanomaterials and nanotechnology*, 2007, (Tartu University press, Tartu).

[2] Yury Gogotsi, *Nanomaterials Handbook*, 2006, (Taylor & Francis Group, Florida).

[3] B.S. Murthy, P. Shankar, Baldev Raj, B.B Rath, James Murday, *Textbook of Nanoscience and Nanotechnology*, 2013 (Universities Press Private Limited+Spinger, India).

[4] Rajendra Kumar Goyal, *Nanomaterials and Nanocomposites*, 2018, (Taylor & Francis, Newyork).

[5] Guozhong Cao, *Nanostructures and Nanomaterials*, 2004 (Imperial College Press, London).

[6] Chris Binns, *Introduction to nanoscience and nanotechnology*, 2010, (Wiley, New Jersey).

[7] Yong Jiang, Dandan Chen, Jinsong Song, Zheng Jiao a, Qiliang Ma, Haijiao Zhang, Lingli Cheng, Bing Zhao, Yuliang Chu, *Electrochimica Acta*. **91** (2013) 173.

[8] Y.Y. Ian Bu, Ray Huang, *Ceram. Int.* DOI: http://dx.doi.org/10.1016/j.ceramint.2016.08.136.

[9] Zijiong Li, Ping Liu, Gaoqian Yun, Kai Shi, Xiaowei Lv, Kun Li, Jianhua Xing, Baocheng Yang, *Energy*, DOI: http://dx.doi.org/10.1016/j.energy. 2014.03.003.

[10] Shuo Huang, Yuhong Jin, Mengqiu Jia, *Electrochimica Acta*. **95** (2013) 139.

[11] Rakesh Behari Mathur, Bhanu Pratap Singh, Shailaja Pande, *Carbon Nanomaterials*, 2017, (Taylor & Francis group, Florida).

[12] Plawan Kumar Jha, A thesis on '*Chemically reduced graphene oxide for Supercapacitor Applications*', IISER-Pune, India (2018).

[13] Sekhar Chandra Ray, *Applications of Graphene and Graphene-oxide based Nanomaterials*, 2015, (Elsevier, UK).

[14] M. Ayrat Dimiev, Siegfried Eigler, *Graphene oxide*, 2017, (Willey, UK)

[15] T. Artur Dideiki, Alexander Y. Vul, *Front. Phys.* **6** (2019) 1.

[16] D.R. Madhuri, K. Kavyashree, Ashok R Lamani, H.S. Jayanna, G. Nagaraju, Shridhar Mundinamani, *Materials Today: Proceedings*. **49** (2022) 865.

[17] D. Suresh, Udayabhanu, H. Nagabhushana, S.C. Sharma, *Mater*. *Lett*. **142** (2015) 4.

[18] D. Suresh, P.C. Nethravathi, H. Udayabhanu, S.C.S. Nagabhushana, *Ceram. Int*. **41** (2015) 4810.

[19] T. Kuila, S. Bose, P. Khanra, Ananta Kumar Mishra, Nam Hoon Kim, Joong Hee Lee, *Carbon* **50** (2012) 914.

[20] V.u. Thu Ha Thi, T.T.T. Tran, H.N.T. Le, P.H.T. Nguyen, Ngoc Quynh Bui, Nadine Essayem, *Bull. Mater. Sci*. **38** (2015) 667.

[21] M.T.H. Aunkora, I.M. Mahbubula, R. Saidurb, H.S.C. Metselaar, *RSC Adv*. 6 (2016) 27807.

[22] S. Thakur, N. Karak, *CARBON* **50** (2012) 5331.

[23] Z. Khosroshahi, M. Kharaziha, F. Karimzadeh, A. Allafchian, *AIP Conf. Proc*. **1920** (2018) 020032.

[24] C.M.J. Fernandez-Merino, L. Guardia, J.I. Paredes, S. Villar-Rodil, P. Solıs-Fernandez, A. Martınez-Alonso, J.M.D. Tascon, *J. Phys. Chem. C*. **114** (2010) 6426.

[25] K. S. Novoselov, A. K. Geim, S. V Morozov, D. Jiang, Y. Zhang, S. V Dubonos, I. V Grigorieva, A. A. Firsov, Science. 306 (2004) 666.

[26] K. Geim, *Science*. **324** (2009) 1530.

[27] Y. Zhang, Y.-W. Tan, H. L. Stormer, and P. Kim, *Nature* **438** (2005) 201.

[28] J. Wu, W. Pisula, and K. Müllen, *Chem. Rev.* **107** (2007) 718.

[29] M. J. Allen, V. C. Tung, and R. B. Kaner, *Chem. Rev.* **110** (2010) 132.

[30] Alfred Tawirirana Chidembo, A thesis on '*Advanced graphene-metal oxide nanostructured composites for supercapacitors*', University of Wollongong, Australia (2014).

[31] J. K. Gan, Y. S. Lim, A. Pandikumar, N.M. Huang, H.N. Lim, *RSC Advances*, **5** (2015) 12692.

[32] W. M. Chang, C. C. Wang, C. Y. Chen, *Electrochem. Acta.*, **212** (2016) 130.

[33] J. K. Gan, Y. S. Lim, N. M. Huang, H. N. Lim, *RSC Adv.*, **5** (2015) 75442.

[34] H. Zhuo, Y. Hu, Z. Chen, L. Zhong, *Carbohydr. Polym.*, **215** (2019) 322.

[35] Z. Yang, J. Ma, B. Bai. A. Qiu, D. Losie, D. Shi, M. Chen, *Electrochem. Acta.*, **322** (2019) 134769.

[36] X. Li, M. Zhou, H. Xu, G. Wang, Z. Wang, *J. Mater. Sci.*, **49** (2014) 6830.

[37] Yan Wang, Jin Guo, Tingfeng Wang, Junfeng Shao, Dong Wang, Ying-Wei Yang, Nanomaterials, **5** (2015) 1667-1689.

[38] Muhammad Amirul Aizat Mohd Abdah, Nur Hawa Nabilah Azman, Shalini Kulandaivalu, Yusran Sulaiman, *Materials and Design*. **186** (2020) 108199.

[39] Adam Marcus Namisnyk, A thesis on '*A survey of electrochemical supercapacitor Technology*', University of Technology, Sydney (2003).

[40] Arsalan Haider Noor, A thesis on '*Graphene Based Material for Supercapacitance Application*' Capital university of science and technology, Islamabad (2021).

2.1 Introduction

There are numerous techniques for preparing various types of nanomaterials such as colloids, clusters, powders, tubes, rods, wires, thin films, and so on. Some of the existing conventional techniques for synthesising various types of materials are optimised to produce novel nanomaterials, while others are developed. Nanotechnology is a multidisciplinary field. To synthesise nanomaterials, various physical, chemical, biological, and hybrid techniques are available. There are numerous possibilities for each type. The technique used is determined by the material of interest, the type of nanomaterial (zero dimensional (0-D), one dimensional (1-D), or two dimensional (2-D), as well as their size and quantity [1]. Top-down and bottom-up approach are the main approaches for the synthesis of nanomaterials.

Top-down approach

Top-down methods start with a larger-scale pattern that is reduced to nanoscale after a series of operations are performed on it. Top-down approaches based on material grinding. As a result, these processes are subtractive. Because the mechanical devices used to shape objects have stiff and hard parts, these methods are not appropriate for soft samples. The main disadvantage of these methods is that they require large installations and a lot of money to build. As a result, these methods are quite costly. Furthermore, the growth rate is slow, making these methods unsuitable for large-scale production. Top-down methods, on the other hand, are ideal for laboratory experimentation.

Top-down methods use a 'force' (e.g., mechanical force, laser) to break down bulk materials into nanoparticles. Some of the methods in top-down approach are listed in the figure 2.1. 'Ball milling' is a popular method for mechanically breaking down bulk materials into nanomaterials. Furthermore, nanoparticles can be created through laser ablation, which uses short pulses of light. To ablate a target, pulse lasers (such as femtosecond lasers) are used (solid). The most common top-down methods for nanomaterial synthesis are mechanical ball milling, thermal decomposition, and laser ablation [2].

i) Ball milling or Mechanical milling:

Mechanical milling is a low-cost method for producing nanomaterials from bulk materials. Ball milling is an efficient method in producing phase blends and is useful in the production of nanocomposites. Mechanical milling is used to make oxide- and carbide-strengthened aluminium alloys, wear-resistant spray coatings, aluminum/ nickel/ magnesium/ copper nanoalloys, and a variety of other nanocomposite materials [3].

ii) Electrospinning:

Electrospinning is one of the most basic top-down methods to produce nanostructured materials. It is commonly used to create nanofibers from a wide range of materials, most notably polymers. Coaxial electrospinning was a significant breakthrough in electrospinning. Coaxial electrospinning is an efficient and straightforward top-down method for producing core-shell ultrathin fibres on a large scale. These ultrathin nanomaterials can have lengths of several centimetres. This technique has been used to create core-shell and hollow polymer, inorganic, organic, and hybrid materials [3].

iii) Lithography:

Lithography, which uses a focused light beam or beam of electrons, is a useful tool for developing nanoarchitectures. There are two types of lithography: masked lithography and maskless lithography. Using a specific mask or template, nanopatterns are transferred over a large surface area in masked nanolithography. Photolithography, nanoimprint lithography, and soft lithography are all examples of masked lithography. Scanning probe lithography, focused ion beam lithography and electron beam lithography are all examples of maskless lithography. Without the use of a mask, arbitrary nanopattern writing is performed in maskless lithography. Ion implantation with a focused ion beam in conjunction with wet chemical etching can be used to create 3D freeform micro-nano-fabrication [3].

iv) Sputtering:

Sputtering is a technique for creating nanomaterials that involves bombarding solid surfaces with high-energy particles such as plasma or gas. Sputtering is thought to be an efficient method for creating thin films of nanomaterials. Sputtering deposition involves the bombardment of the target surface with energetic gaseous ions, which causes the physical ejection of small atom clusters depending on the incident gaseous-ion energy. Sputtering can be accomplished in a variety of ways, including magnetron, radio-frequency diode, and DC diode sputtering. Sputtering is typically performed in an evacuated chamber and sputtering gas is introduced into it. A high voltage is applied to the cathode target, causing free electrons to collide with the gas, resulting in gas ions. The ions which are positively charged are strongly accelerated in the electric field towards the cathode target, which they repeatedly strike, resulting in the ejection of atoms from the target's surface. Sputtering is an interesting technique because the sputtered nanomaterial composition is the same as the target material with fewer impurities, and it is less expensive than electron-beam lithography [3].

v) Arc discharge method:

The arc discharge method can be used to create a variety of nanostructured materials. Fullerenes, carbon nanohorns (CNHs), carbon nanotubes, few-layer graphene (FLG), and amorphous spherical carbon nanoparticles are some of the carbon-based materials produced. The arc discharge method is extremely important in the production of fullerene nanomaterials. During the formation process, two graphite rods are adjusted in a chamber with a constant helium pressure. It is critical to fill the chamber with pure helium because the presence of moisture or oxygen inhibits fullerene formation. Arc discharge between the ends of the graphite rods drives carbon rod vaporisation. The conditions under which arc discharge occurs are important in creating new types of nanomaterials. The circumstances under which various carbon-based nanomaterials are formed using the arc discharge method. As their growth mechanisms differ, different carbon-based nanomaterials are collected from different positions during the arc discharge method. Under different atmospheric conditions, different morphologies of single-wall carbon nanohorns (SWCNHs) can be obtained. Graphene nanostructures can be efficiently created using the arc discharge method. The conditions present during graphene synthesis can have an impact on its properties. Graphene sheets prepared using a hydrogen arc discharge exfoliation method are found to be superior in terms of electrical conductivity and thermal stability when compared to those obtained using an argon arc discharge exfoliation method [3].

vi) Laser ablation:

This is one of the fundamental methods for preparing nanoparticles from various precursor solvents. The metallic solution is mixed in a liquid medium while being exposed to a laser beam, and the condensed metallic solution produces nanoparticles ranging in size from 1-100 nm. This method offers an alternative to conventional chemical reduction methods for the synthesis of nanoparticles. Various types of toxic substances are produced during the synthesis process by chemical methods. As a result, this method is environmentally friendly, cost effective, and does not generate toxic by-products. Laser ablation produced stable nanoparticles from organic solvents as well as water. This method does not require any toxic chemicals or stabilising agents. As a result, it is a green method of producing nanoparticles [3].

vii) Thermal Decomposition:

The nature of this method is endothermic. The main reaction in this method takes place in the presence of heat. Nanoparticle synthesis is dependent on deposition and the breaking of chemical bonds within compounds in the presence of heat. The specific decomposing temperature is the temperature at which the reactant metal compounds decompose. Pressure and reaction time are also important parameters in the decomposition reaction. The decomposing reactant generates stable nanoparticles of a small size [2].

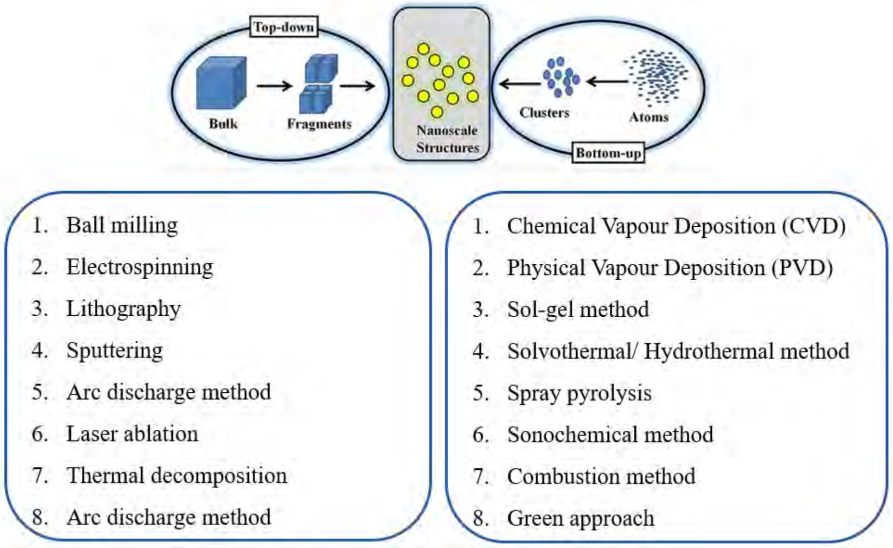

Fig. 2.1 Synthesis of nanomaterials from top-down and bottom-up approaches.

Bottom-up approach

The bottom-up method begins at the atomic level and progresses to the production of nanostructures with subsequent atom/molecule self-assembly. Nanomaterials with well-defined morphology, size, shape and chemical composition are created through the growth and self-assembly of atoms and molecules acting as building blocks. The two main types of bottom-up techniques for the synthesis of nanomaterials are known as solid-phase and liquid-phase techniques. Chemical (such as CVD and thermal breakdown) or physical solid phase techniques are both possible (PVD) [1].

A bottom-up method promises a higher possibility of obtaining nanostructures with fewer defects, a more homogenous chemical composition and better short-range and long-range ordering. This is due to the fact that the bottom-up method is primarily motivated by the reduction of Gibbs free energy, resulting in the production of nanostructures and nanomaterials that are closer to a thermodynamic equilibrium state.

Contrarily, a top-down strategy is more likely to cause internal stress as well as surface defects and contaminations [4].

The bottom-up methods used to prepare nanomaterials are sol-gel, co-precipitation, alkaline precipitation, and hydrolysis, are done in the liquid phase. These techniques also include liquid/liquid techniques (chemical reduction, indirect reduction, biological reduction, spray drying, spray pyrolysis, and solvothermal). Some of the bottom-up methods are listed in the figure 2.1. Now a more thorough explanation of the available methods is discussed here.

i) Chemical Vapour Deposition (CVD):

The preparation of nanomaterials widely uses CVD technique. Its prime application is the creation of solid thin film coatings for surfaces. The production of high purity bulk materials, powders, and composite materials is another use of this technique. The main factors impacting the quality of the deposition include the sort of reactor (hot wall or cold wall reactors), reaction temperature (200 to 1600° C), reaction pressure (from sub-torr to above atmospheric pressure), reaction rate, and precursor concentration [2].

Chemical vapour deposition is a hybrid process that uses chemicals in the vapour phase to create coatings of various inorganic or organic materials. It is frequently used in industry due to its affordability, convenience of processing, capacity to deposit a variety of materials, and relatively easy instrumentation. Nanocrystalline or single-crystalline films are conceivable under specific deposition conditions. There are numerous CVD variations, including Plasma Enhanced CVD, Atomic Layer Epitaxy, Metallo Organic CVD, and Vapour Phase Epitaxy (PECVD). Their source gas pressure, geometrical design, and temperature range are different [1].

However, the fundamental CVD process can be thought of as the movement of reactant gas or reactant vapour towards the substrate, which is kept at a high temperature where the reactant cracks into various products that diffuse on the surface, go through a chemical reaction at the proper site, nucleate, and grow to form the desired material film. In order to remove the by-products from the substrate, they must be returned to the gaseous phase. Even reactor walls are susceptible to deposition in a hot wall setup. The design of cold walls avoids this. Additionally, a hot wall setup allows for gas phase reactions, which are prevented by a cold wall setup [1].

ii) Physical Vapour Deposition (PVD):

PVD and CVD both are used to produce thin films on the substrate. As their names suggest, the fundamental distinction between these two processes is that PVD uses physical forces to make thin films, whereas CVD uses chemical reactions to form thin films. During the PVD process, no chemical reactions take place. CVD, on the other hand, employs a source material with substantially lower purity because it is combined with volatile precursors. The deposition process begins when this mixture is injected into the chamber containing the substrate to be coated.

PVD is a vacuum deposition technology that is commonly used in the semiconductor industry to create thin films and coatings. In this process, the target contains an evaporation source that acts as a cathode, vaporizing the material from a solid or liquid source. The atomic particles evaporate after being heated with an electron beam.

The collision between the released particles and the gas molecules put into the chamber causes the particles to accelerate. This generates plasma, which then travels via the deposition chamber and a vacuum pump to the surface, where it condenses, resulting in the development of a thin coating. PVD can be utilized to create both thin films and multi-layered coatings. The thickness of these films could range from a few hundred to thousands of nanometers [2].

PVD methods can be divided into two categories based on the source of removing the species from the target: evaporation and sputtering. The growth species are evacuated from the source by thermal methods in evaporation, whereas atoms or molecules are dislodged from a solid target by the impact of plasma. Because evaporation deposition of thin films is performed at a low pressure (10^{-3}-10^{-10} torr), atoms and molecules in the vapor phase do not collide with one other prior to arriving at the substrate because the mean free path is very broad in comparison to the source-to-substrate distance. As a result, the film's quality is relatively low [5].

The size, morphology, and yield of the clusters are determined by three fundamental parameters: i) the rate at which atoms are supplied to the region of supersaturation where condensation occurs, (ii) the rate at which energy is removed from the hot atoms via the condensing gas medium, and (iii) the rate at which clusters are removed from the supersaturated region once nucleated. This method has several advantages, including a higher production rate (60 g/h), high purity of final products, a high yield (~75%), a flexible technique, the ability to produce a wide range of compounds (metals, alloys, ceramics, intermetallic compounds, semiconductors, composites, and so on) and controlled particle size distribution [5].

iii) <u>Sol-gel method</u>:

As the name implies, sol gel consists of two types of materials or components, 'sol' and 'gel.' Sol gels have been known to us since M. Ebelman invented them in 1845. However, it is only in the last one or two decades that there has been significant interest in it, both in the scientific and industrial fields, as a result of the discovery of the numerous advantages it has over other procedures. To begin with, sol gel production is typically a low-temperature process. This results in decreased energy use and pollutants. It is hardly unexpected, then, that it is a desired step in nuclear fuel production. Despite the fact that the sol-gel technique produces highly pure, well-controlled ceramics, it competes with alternative processes like as CVD or metalloorganic vapours derived ceramics.

As the name implies, sol gel consists of two types of materials or components, 'sol' and 'gel.' Sol gels have been known to us since M. Ebelman invented them in 1845. However, it is only in the last one or two decades that there has been significant interest in it, both in the scientific and industrial fields, as a result of the discovery of the numerous advantages it has over other procedures. To begin with, sol gel production is typically a low-temperature process. This results in decreased energy use and pollutants. It is hardly unexpected, then, that it is a desired step in nuclear fuel production. Despite the fact that the sol-gel technique produces highly pure, well-controlled ceramics, it competes with alternative processes like as CVD or metalloorganic vapours.

Metal oxides are often synthesized using the sol-gel process in three stages.

Stage 1: The precursor salt undergoes hydrolysis, resulting in the creation of a hydroxide solution.

Stage 2: the hydroxide solution is condensed such that three-dimensional gel structures are created.

Stage 3: Based on the drying technology used, the prepared gel is exposed to the drying process, which results in the development of xerogel or aerogel.

iv) Solvothermal method:

The solvothermal approach is frequently used at supercritical temperatures above 300° C. However, in recent years, some studies have been using this approach for nanocrystal production under relatively mild conditions (i.e., temperatures below 300° C). So far, the solvothermal technology has been used to synthesis a variety of nanomaterials such as metals, metal oxides, semi-conductors, alloys, composites, hydroxides, zeolites, and ceramics with various morphologies such as nanoparticles, nanospheres, nanosheets, nanotubes, nanorods, and so on.

In the solvothermal approach, numerous organic solvents with varying properties may be used as a reaction medium in addition to water. As a result, the potential for developing novel materials is relatively high in this synthesis method. Because the organic solvent has the dual role of providing the reaction medium and generating a solvent-reactant complex in the solvothermal technique, selecting an adequate solvent is critical. When choosing a solvent for this procedure, several criteria should be considered, including molecular weight, density, heat of evaporation, melting temperature, boiling point, dipole moment, polarity and dielectric constant. Organic solvents commonly employed in solvothermal techniques include ethyl alcohol, methyl alcohol, butanol, propanol, heptanol, Ethylene glycol benzyl alcohol and others [2].

v) Hydrothermal method:

This synthesis process is suitable for producing nano to micro size particles on a big scale. It is a very old process that was most likely invented by the German scientist

Robert Bunsen in 1839 to produce crystals of strontium and barium carbonates. In this procedure, necessary chemical precursors are dissolved in water and placed in a vessel constructed of steel or another suitable metal that can resist high temperatures of up to 300^o C and high pressures of more than 100 bars. The autoclave is commonly equipped with temperature and pressure controls, as well as measuring gauges.

When it is difficult to dissolve the precursors at low or room temperature, the approach is advantageous. If the material has a high vapour pressure at its melting point or crystalline phases are not stable at melting point, the process can be used to grow nanoparticles. This approach can also produce homogeneity in the shapes and sizes of the nanoparticles. Hydrothermal synthesis has produced a variety of oxide, sulphide, carbonate, and tungstate nanoparticles. Forced hydrolysis is a version of the hydrothermal synthesis process. In this situation, dilute solutions (10^{-2} to 10^{-4} M) of inorganic metal salts are often utilized, and hydrolysis is performed at temperatures higher than 150^o C.

vi) Spray pyrolysis:

Spray pyrolysis is a method of converting liquid to particle that occurs in the vapor phase at a slightly high temperature. A solution containing dissolved precursor is sprayed into a vector gas in the form of small droplets onto the surface of a heated substrate in this process. It is critical to choose appropriate chemical reactants such that undesirable products evaporate at the deposition temperature. Because solutions or sols are utilized in this procedure, it is categorized as a liquid phase method. Spray pyrolysis is widely utilized in industrial applications because it is simple, inexpensive, adaptable and can be easily developed for large-scale deposition.

As spray pyrolysis is a non-contact technique, numerous layers or films can be placed without harming the underlying layers. A spray pyrolysis setup consists of two basic components: a furnace to heat the substrate and a spray gun to spray the solution onto the substrate. The process is cost-effective since it is performed in a continuous way under atmospheric pressure, as opposed to other procedures like as sol-gel and CVD, which are performed in many steps and under vacuum pressure. Furthermore, because of the chemical flexibility of this process, improved ceramics and films might be produced [2].

Four major phases are predicted in the spray pyrolysis process:

1) Droplets are formed from a precursor solution.
2) As a result of evaporation, droplet size shrinks.
3) Oxides are produced from precursors.
4) The solid particles are then created.

Droplets are often formed with the aid of air interference (two-fluid atomization) or without the assistance of air interference (ultrasonic atomization). The advantage of two-fluid atomization is that it has a high throughput, which ultrasonic atomization does not have. Ultrasonic atomization, on the other hand, resulting in a small size distribution, contrary to the former, which results in a broad size range.

vii) Co-Precipitation:

It is a simple, economical and industrially viable technique and one of the oldest wet chemical processes for the synthesis of nanomaterials is co-precipitation. In this approach, a specific ion is precipitated fractionally, followed by the precipitation of other ions in its vicinity. Hydroxides, sulphates, chlorides, carbonates, and oxalates are the most commonly employed precipitants in the aforementioned procedure. One can tailor the process to get nano or micro materials by adjusting the value of pH, temperature, precipitating agent and solvents [2].

viii) Solution Combustion Synthesis (SCS):

Solution combustion synthesis is a fast and simple technique with significant time and energy savings. This method is directly employed in the manufacture of high purity, homogenous oxide powders. The combustion synthesis technique is based on thermodynamic concepts employed in the field of propellants and explosives, and its extrapolation to the combustion synthesis of ceramic oxides, as well as its thermodynamic interpretation, has been thoroughly explored by several researchers. The effectiveness of this process is closely related to the composition of a suitable fuel or complexing agent in water and an exothermic redox reaction between the fuel and the oxidant.

Based on the exothermicity of the redox reaction, solution combustion synthesis uses metal salts as oxidants, such as nitrates, sulphates, and carbonates, and fuels as reducing reagents, such as urea, glycine, sucrose, and starch. The released heat from the combustion reaction provides the energy required for the synthesis of oxides, culminating in temperatures exceeding 3000° C in some situations. The most evident advantage of SCS is its ability to save time and energy. When the reagent combination is burned, the high self-generated energy may convert precursors into the relevant oxides without the need for extra external energy. As a result, the products are manufactured in a matter of minutes. Due to their intrinsic qualities, porous materials are easily affordable to SCS. Because of their enormous surface areas available for reactions, interfacial transport, and/or dispersion of active sites, porous materials have been widely used for energy storage including supercapacitors, lithium-ion batteries, hydrogen and methane production, solar cells and fuel cells, sensing, adsorption, catalysis and separation [6].

Apart from the two most obvious benefits of time/energy efficiency and well-developed porosity, SCS has the following advantages [6]:

i) the instrumentation's simplicity and low cost, as well as the ease with which the SCS can be scaled-up.

ii) the potential to create goods with various functionalities and structural makeups, such as metals, intermetallics, metal-matrix composites, cermets, solid solutions, carbides, nitrides, borides, ceramics, and oxides.

iii) the potential to create ternary or quaternary oxides with high purity, which would be extremely challenging to do otherwise due to the complex structures and slow rate of solid-state reactions.

iv) the potential to create ternary or quaternary oxides with high purity, which would be extremely challenging to do otherwise due to the complex structures and slow rate of solid-state reactions.

v) Materials with a large active surface area can be created for heterogeneous photocatalysts using SCS, which is advantageous for the transfer and separation of charge carriers.

vi) Complex oxides will develop in a homogenous mixed solution at a high reaction temperature. Additionally, this technique can use raw materials that are safe for the environment.

ix) Sonochemical method:

In chemistry, ultrasound has become a valuable tool. The interaction of ultrasound waves (pressure wave) with a liquid medium leads to the formation of ‘cavities’ in liquid. These cavities undergo continuous compression and rarefactions when they interact with positive and negative pressure cycles. This goes on until the cavities reach a critical radius, which is determined by the frequency of ultrasound.

When solutions are exposed to intense ultrasound, acoustic fields implosively collapse bubbles in solution, producing high-temperature and high-pressure fields at the bubble’s cores (shown in figure 2.2). Acoustic cavitation is the name given to this phenomenon. The reactivity of the precursors is increased in this process by taking advantage of the high amount of energy generated when bubbles break in a liquid. Bubbles are created by utilizing ultrasonic waves with frequencies ranging from 20 KHz to 2 MHz [1]. It is an alternate approach for enhancing chemical reactions in liquids by heating and/or pressurizing them. Ultrasound is a very interesting approach for the synthesis of metal nanoparticles, with features such as a fast reaction rate and the capacity to create very small metal particles. On the other hand, metal nanoparticles generated by sonochemical reduction, have larger size distributions. Some efforts to adjust particle size and size distribution have been reported utilizing varied initial metal concentrations, surfactant types, and coexisting alcohol types [7].

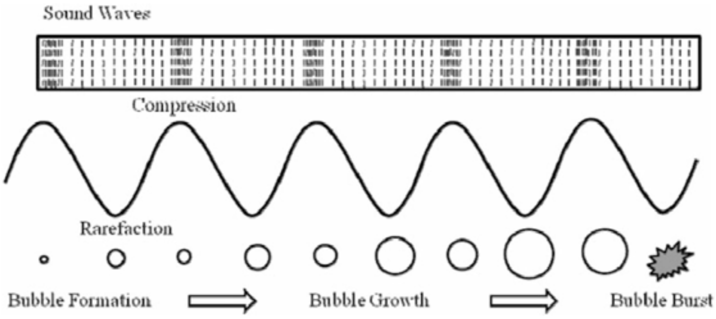

Fig. 2.2 Sine wave formed by compression and refraction of ultrasound wave [1].

Although it is unclear how nanoparticles can be created using the sonochemical approach, it is widely agreed that the formation, development, and collapse of bubbles in liquids is the most essential pathway for producing the reactions. While travelling through the liquids, ultrasonic waves form very small bubbles that increase until they reach a critical size and then burst, releasing very high energy to locally reach a temperature of 5,000^{o} C and a pressure a few hundred times that of atmospheric pressure. The solute in the liquid must diffuse to the expanding bubble for the reaction to occur in the gas phase. The reaction can also occur in the liquid phase at exploding bubble where in the interfacial region surrounding the bubble (~200 nm distance) the temperature as high as ~1,600^{o} C can be reached. Typically, the size of a bubble can be from ten to few tens of microns. Careful use of the solvents and solutes are very important. Non-volatile liquids would prevent formation of bubbles, which is desired, as only reactants should find their place inside the bubble in the form of vapour. Solvents should be inert and stable to ultrasonic irradiation. Interestingly, the cooling rates also can be as high as 10^{11} ^{o}C or more.

Advantages of Sonochemical method

- Ultrasound assisted synthesis aids in preparation of uniformly distributed and uniformly sized nanocomposites in short time and utilizing less energy as compared to methods such as mechanical milling, electrodeposition etc.
- High reaction rates can be achieved.
- Enhanced properties such as crystallinity, dissolution, filtration, kinetics can be observed.
- Higher value of specific capacitance of a supercapacitor can be expected.
- It is environmentally friendly.
- 5 g graphite powder and 2.5 g sodium nitrate were combined and treated with 120 mL of H_2SO_4 (95 %).
- The container was placed in an ice bath for 30 minutes while the mixture was stirred.
- Added 15 g of potassium permanganate and kept at a temperature of less than 20° C.

2.2 Synthesis of graphene oxide by modified Hummer’s method

Modified Hummer's approach was utilized to synthesize GO from natural graphite powder with no additional purification.

- The stirring was continued all night and 150 mL of DI water was gradually added. As soon as the DI water was added, the reaction temperature was quickly raised to 98° C.
- Then 50 mL of 30% hydrogen peroxide was added.
- The product was allowed to cool before being washed with 5% hydrochloric acid, then with DI water, and finally dried.
- Brown coloured powder was formed. It was kept in an airtight container.

The pictures of different steps involved in the synthesis are shown in the figure 2.3.

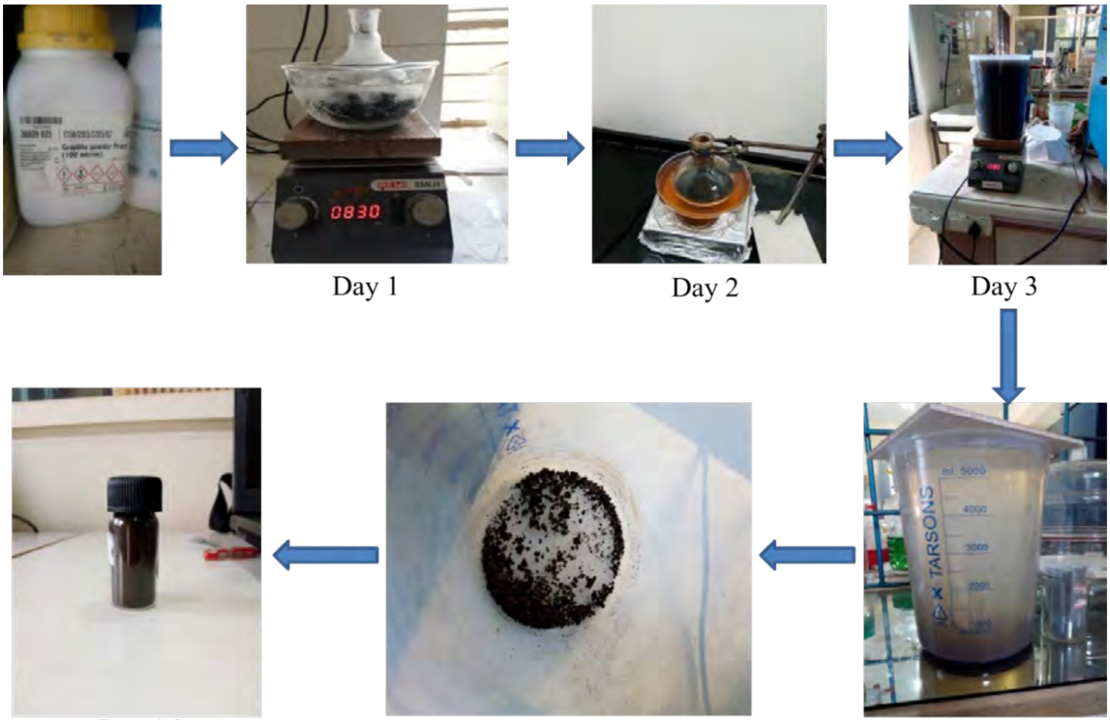

Day 1 Day 2 Day 3

Day 16 Day 13 Day 6

Fig. 2.3 Different steps involved in the preparation of GO.

2.3 Reduction of graphene oxide by green approach

Green nanotechnology is described as the technology used to make clean technology that can lessen environmental concerns while simultaneously improving human health conditions [8]. It is associated with the use of nanotechnology products and the manufacturing process. Green nanotechnology creates new nanoproducts with superior qualities. The primary goal of developing new nanoproducts is to improve sustainability and make them more environmentally friendly.

Now a days, the green method of synthesizing reduced graphene oxide using plant extracts has attracted the interest of the research community more than the traditional method of employing chemicals. The green method has advantages such as less cost and environmental friendliness. The reduction of graphene oxide is carried out in this study using Phyllanthus Emblica, often known as amla. This fruit is produced throughout the country and is high in vitamin C (478.56 mg/100 mL). The benefit of utilizing Vitamin C is that it is made up of simply carbon, oxygen, and hydrogen. As a result, the possibility of introducing heteroatoms into the reduced graphene oxide is reduced.

Preparation of amla extract

Different steps to prepare amla extract are explained below and shown in figure 2.4

- Phyllanthus Emblica (Amla) was obtained from the local market.
- Fresh fruits were washed and wiped gently and the pulp was ground (without seeds) using a laboratory mixer.

- The ground amla and DI water were taken in a ratio of 1:10 (i.e., 1 mg in 10 mL of DI water) in a round-bottomed flask and kept it in a reflux arrangement for about 4 hours at 70°C. The extract was filtered and dried.

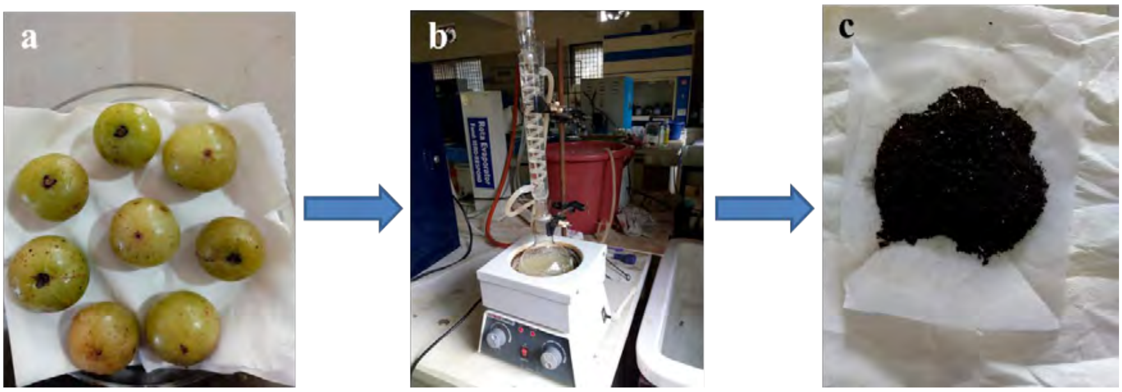

Fig. 2.4 a) Fresh fruits of amla, b) Ground amla in reflux system,

c) Amla extract in powder form

Preparation of rGO

50 mg of GO powder is dispersed in 50 mL of DI water and ultrasonicated for 40 minutes. This suspension was properly mixed with amla extract solution and then heated for 30 minutes. Finally, it was washed with DI water and dried. Black coloured powder was formed and stored in an airtight container.

The procedure of preparation of rGO is given in flowchart and shown in figure 2.5.

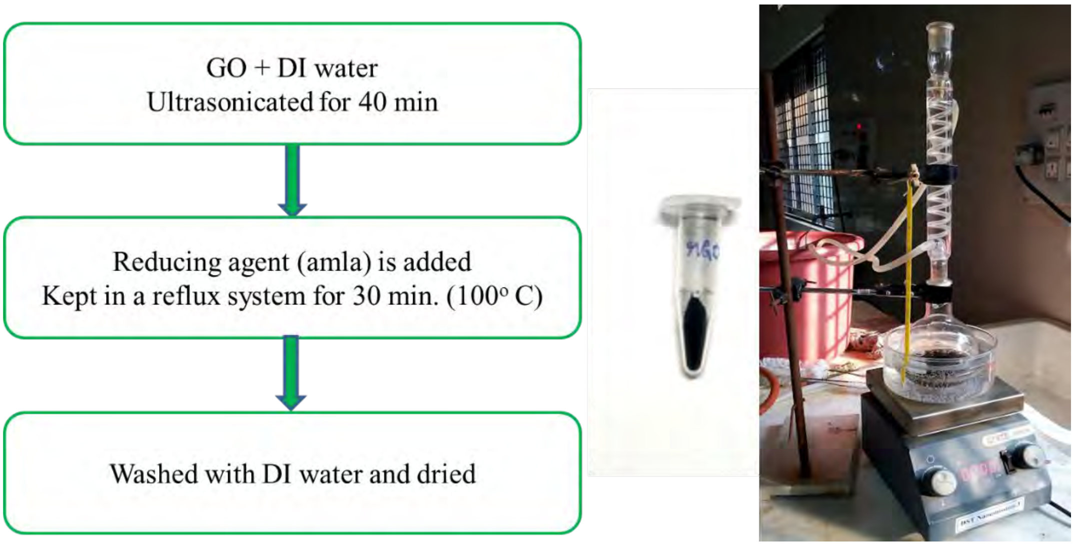

Fig. 2.5 Flow chart of steps involved in the preparation of rGO (black coloured powder).

2.3.1 Reduction Mechanism

Phyllanthus Emblica, generally called as gooseberry, provides therapeutic and nutritional benefits for regaining lost physical and mental power [9]. This is because of the amla fruit's high antioxidant content. This antioxidant activity is owing to the high vitamin C or ascorbic acid content. In comparison to lime, apple, grapes, and pomegranate, amla fruit juice contains the most vitamin C (478.56 mg/100 mL) [10]. According to research, the additional components of amla include sugar, gallic acid, flavonoids, and polyphenolic chemicals. Ascorbic acid functions as a redox buffer, reducing and then neutralizing reactive oxygen species. We successfully synthesized reduced graphene oxide using amla fruit extract as a reducing agent.

Though amla has several constituents, vitamin C, often known as ascorbic acid, plays a key role in the reduction process. Hydroxyl, epoxy and carbonyl are the primary functional groups of GO. The reaction of the epoxy group with the polyhydroxy functional groups of ascorbic acid results in the epoxy group ring-opening. Ring expansion caused by condensation with loss of water molecules. More rearrangement to cause GO deoxygenation. In the case of a hydroxyl group, condensation is once again responsible for ring formation. The synthesis of graphene moiety is then caused by ring cleavage, which facilitates green reduction. The oxidized version of ascorbic acid may generate π-π stacking between rGO sheets, preventing agglomeration [11].

2.4 Synthesis of metal oxides by solution combustion method

Solution combustion method was implemented for metal oxides with metal nitrates were the starting material and amla extract as a fuel. The flowchart for the synthesis of metal oxide is shown in the figure 2.6.

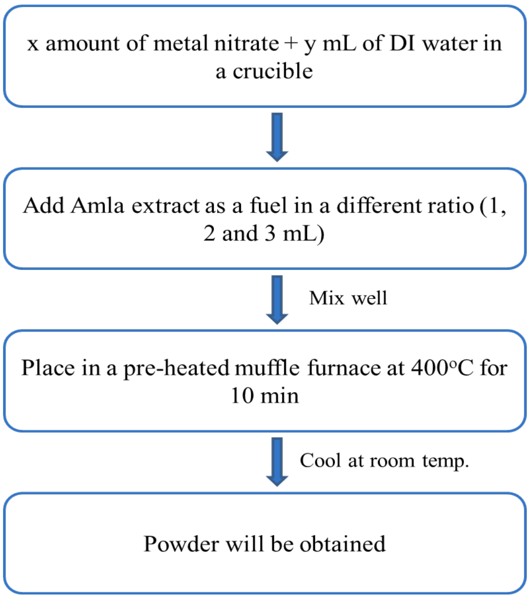

Fig. 2.6 Flow chart for synthesis of metal oxides by solution combustion method.

2.4.1 Synthesis of NiO

NiO was synthesized from nickel nitrate by solution combustion method which is shown in figure 2.7.

- 2.95 g of $Ni(NO_3)_2.H_2O$ was taken in a crucible and mixed with 5 mL of DI water.

- 1, 2 and 3 mL of amla extract (0.5 g of amla extract was dispersed in 50 mL of DI water in a beaker, then it was subjected to continuous stirring for 30 min) was added to the crucible.

Fig. 2.7 Formation of NiO from Nickel nitrate.

- The solution was mixed vigorously until the homogenous solution was obtained and kept it in a pre-heated muffle furnace using long crucible tongs for 10 min at a temperature of 400° C.

- Black colored powder was formed as a result. The powder was crushed well using mortar and pestle and kept it in an airtight container until further use.

2.4.2 Synthesis of CuO

- 2.41 g of $Cu(NO_3)_2.3H_2O$ was taken in a crucible and mixed with 5 mL of DI water.
- 1, 2 and 3 mL of amla extract (0.5 g of amla extract was dispersed in 50 mL of DI water (maintained 1:10 ratio) in a beaker, then it was subjected to continuous stirring for 30 min) was added to the crucible.
- The solution was mixed vigorously until the homogenous solution was obtained and kept it in a pre-heated muffle furnace using long crucible tongs for ~10 min at a temperature of 500^o C.
- Black colored powder was formed as a result. The powder was crushed well using mortar and pestle and kept it in an airtight container until further use.

2.4.3 Synthesis of ZnO

- 2.94 g of $Zn(NO_3)_2.6H_2O$ was taken in a crucible and mixed with 5 mL of DI water.
- 1, 2 and 3 mL of amla extract (0.5 g of amla extract was dispersed in 50 mL of DI water in a beaker, then it was subjected to continuous stirring for 30 min) was added to the crucible.
- The solution was mixed vigorously until the homogenous solution was obtained and kept it in a pre-heated muffle furnace using long crucible tongs for ~10 min at a temperature of 400^o C.

- White colored powder was formed as a result. The powder was crushed well using mortar and pestle and kept it in an airtight container until further use.

2.4.4 Synthesis of Co_3O_4

- 1 g of $Co(NO_3)_2.6H_2O$ was taken in a crucible and mixed with 10 mL of DI water.
- 1, 2 and 3 mL of amla extract (0.5 g of amla extract was dispersed in 50 mL of DI water in a beaker, then it was subjected to continuous stirring for 30 min) was added to the crucible.
- The solution was mixed vigorously until the homogenous solution was obtained and kept it in a pre-heated muffle furnace using long crucible tongs for ~10 min at a temperature of 450^o C.
- Black colored powder was formed as a result. The powder was crushed well using mortar and pestle and kept it in an airtight container until further use.

2.5 Synthesis of rGO/metal oxides composites sonochemical method

Sonochemical method is a powerful synthesis process for producing inorganic nanoparticles. The chemical impacts of ultrasonic irradiation result from acoustic cavitation, which causes the fast development, expansion, and implosive collapse of tiny bubbles in liquid media. And the collapse of bubbles produces an immediately strong thermal energy and pressure pulse in a very short time. When liquids are treated with ultrasound, a new environment for chemical reactions can be created. Furthermore, the sonochemical approach adheres to green chemistry principles.

In this study, we have prepared rGO/metal oxide nanocomposites by sonochemical method. The carbon material in the composite form not only improves the electrical conductivity of the composites, but it also acts as a "space barrier" to suppress particle aggregation and maintain the structural integrity of the composites. Graphene has recently been used as an excellent carbonaceous addition material. The chemical impacts of ultrasonic irradiation result from acoustic cavitation, which causes the fast development, expansion, and implosive collapse of tiny bubbles in liquid media. And the collapse of bubbles produces an immediately strong thermal energy and pressure pulse in a very short time. When liquids are treated with ultrasound, a new environment for chemical reactions can be created. Furthermore, the sonochemical approach adheres to green chemistry principles [12].

2.5.1 Synthesis of rGO /NiO

rGO/NiO composite was prepared by a simple sonochemical method.

- 100 mg of GO was dissolved in DI water and ultrasonicated for 40 min.
- 1.5 mL of amla extract solution was added and sonicated for 40 min.
- As prepared solution was kept in a heating mantle for 35 min.
- 400 mg of NiO was added after it comes to room temperature and again ultrasonicated for 40 min.
- Washed this solution for several times and then kept it for drying T 50^o C for 3 hrs, collected the powder sample.

2.5.2 Synthesis of rGO /CuO

A simple sonochemical method was implemented for the synthesis of rGO/CuO composite.

- 100 mg of GO was dissolved in DI water and ultrasonicated for 40 min.
- 1 mL of amla extract solution was added and sonicated for 40 min.
- As prepared solution was kept in a heating mantle for 35 min.
- 500 mg of NiO was added after it comes to room temperature and again ultrasonicated for 40 min.
- Washed this solution for several times and then kept it for drying T 50^o C for 3 hrs, collected the powder sample.

2.5.3 Synthesis of rGO /ZnO

rGO/ZnO composite was prepared by sonochemical method.

- 100 mg of GO was dissolved in DI water and ultrasonicated for 40 min.
- 1 mL of amla extract solution was added and sonicated for 40 min.
- As prepared solution was kept in a heating mantle for 35 min.
- 500 mg of NiO was added after it comes to room temperature and again ultrasonicated for 40 min.
- Washed this solution for several times and then kept it for drying T 50^o C for 3 hrs, collected the powder sample.

2.5.4 Synthesis of rGO /Co_3O_4

A simple sonochemical method was implemented for the synthesis of rGO/Co_3O_4 composite.

- 300 mg of GO was dissolved in DI water and ultrasonicated for 40 min.
- 2 mL of amla extract solution was added and sonicated for 40 min.
- As prepared solution was kept in a heating mantle for 35 min.
- 300 mg of NiO was added after it comes to room temperature and again ultrasonicated for 40 min.
- Washed this solution for several times and then kept it for drying T 50^o C for 3 hrs, collected the powder sample.

2.6 Summary

Graphene oxide has been prepared by most common ‘modified Hummer’s method’ because it is more hydrophilic in nature, no toxic gases are released from the byproducts during the reaction, less time is required for oxidation and easy to exfoliate the final product in water. In most of the cases, GO is reduced via chemical methods that employ various reductants such as hydrazine and sodium borohydride. These components are corrosive, flammable, and highly poisonous, posing a risk to personnel health and the environment. To avoid all these issues, we have followed green approach for the reduction of GO and successfully synthesized rGO by Phyllanthus Emblica (amla) extract as a reducing agent. All the metal oxides are synthesized by solution combustion method with amla extract as a fuel. The rGO/metal oxide nanocomposites are prepared by a simple sonochemical method. All the preparation methods are quite simple, environmentally friendly and no toxic gases are liberated during the reaction.

References

[1] K. Sulabha Kulakarni, *Nanotechnology: Principles and Practices (3^{rd} Edition),* 2015, (Springer, Newyork, USA).

[2] Neha Srivastava, Manish Srivastava, P. K. Mishra and Vijai Kumar Gupta, *Green Synthesis of Nanomaterials for Bioenergy Applications*, 2021, (John Wiley & Sons Ltd. UK).

[3] Nadeem Baig, Irshad Kammakakam, Wail Falath, *Mater. Adv.* **2** (2021) 1821.

[4] Guozhong Cao, *Nanostructures & Nanomaterials*, 2004, (Imperical College Press, London).

[5] Rajendra Kumar Goyal, *Nanomaterials and Nanocomposites*, 2018, (Taylor & Francis, Newyork).

[6] Fa-tang Li, Jingrun Ran, Mietek Jaroniec, Shi Zhang Qiao, *Nanoscale*, **7** (2015) 17590.

[7] [7] Toshiyuki Fujimoto, Shin-ya Terauchi, Hiroyuki Umehara, Isao Kojima, William Henderson, *Chem. Mater.* **13** (2001) 1057.

[8] Marcelo L. Larramendy, Sonia Soloneski, *Green Nanotechnology Overview and Further Prospects*, 2016, (AvE4EvA MuViMix Records), ISBN-10: 953-51-2410-2, ISBN-13: 978-953-51-2410-8.

[9] P. Goel, D. Agarwal, *Int. Medico-Legal Rep. J.* **3** (2020) 104.

[10] B. C. Variya, A. K. Bakrania, S.S. Patel, *Pharmacol. Res.* **111** (2016) 180.

[11] D. R. Madhuri, K. Kavyashree, Ashok R Lamani, H. S. Jayanna, G. Nagaraju, Shridhar Mundinmani, *Materials Today: Proceedings*, **49** (2022) 865.

[12] Kaipeng Wu, Diwei Liu, Weiwei Lu, Kuibao Zhang, *Ultrason Sonochem.* **45** (2018) 167.

3.1 Introduction

In order to characterize small materials or structures at the nanometric scale, specialized characterization methods are usually required. The development of some crucial advancements in traditional characterization techniques created for bulk materials has been the foundation for the majority of the characterization of nanomaterials and nanostructures. For instance, X-ray diffraction (XRD) has been extensively used to determine the crystallite size, crystal structure, lattice constants, and crystalline nature of nanoparticles, nanowires, and thin films. To determine the size, shape and presence of defects in these materials, analysis of nanoparticles has often used scanning electron microscopy (SEM), transmission electron microscopy (TEM), and electron diffraction [1].

There are two fundamental approaches for determining particle size, particle size distribution, morphology, and composition: direct method and indirect method. The direct method examines the particles and takes exact measurements of their dimensions, whereas the indirect method takes advantage of the relationship between particle behaviour and size. UV-vis, XRD, Fourier transform infrared spectroscopy (FTIR), and Raman spectroscopy techniques are considered indirect methods for determining information related to particle size, composition, structure, crystal phase, and characteristics of nanoparticles. Whereas SEM and TEM are the direct methods for determining the size and morphological aspects of nanoparticles [2].

Individual nanostructure characterization and modification necessitate not only high sensitivity and accuracy, but also atomic-level resolution. As a result, diverse microscopy techniques will be essential in the characterization and measurement of nanostructured materials and nanostructures. Instrument miniaturization is clearly not the main difficulty. Physical qualities and short-range forces, which may not play a substantial role in macroscopic characterization may have a significant impact at the nano scale.

3.2 X ray diffraction method

3.2.1 Introduction

The term "X-rays" refers to electromagnetic radiations with wavelengths ranging from 10^{-3} nm to 10 nm. W. Rontgen discovered X-rays in 1895 and gave them that name because their properties were unknown at the time. X-rays are commonly utilized nowadays to picture the inside of optically opaque objects, such as in medical radiography, computed tomography, and security scanners. X-rays can also disclose material properties such as crystal structure, phase transition, crystalline quality, orientation, and internal stress. Because of the interaction between X-rays and matter, this is conceivable. X-rays with wavelengths less than 0.1-0.2 nm are referred to as hard X-rays, whereas those with larger wavelengths are referred to as soft X-rays. The X-rays used in materials analysis are hard X-rays [3].

X-rays are effective for assessing the interior condition of crystalline materials for two reasons. First, hard X-rays penetrate all substances deeply, however the depth of penetration varies depending on the substance. Metals, while optically opaque, can be transparent or translucent to hard X-rays. Second, the wavelengths of X-rays are substantially shorter than those of visible light. This allows for the investigation of microscopic structures that would otherwise be invisible under a standard microscope. Hard X-rays, in instance, have wavelengths comparable to the size of atoms. As a result, they might be diffracted by atoms that are arranged in a regular pattern within the substance. The internal structure of crystalline materials can be revealed at the atomic level by monitoring the diffraction direction and intensity.

X-rays are produced when electrons that have been accelerated to extremely high speeds rapidly decelerate. They are normally created using an X-ray tube with two metal electrodes: a cathode (electronic source) and an anode (metal target). The cathode is kept at a high negative voltage (-V), while the anode is kept at ground potential. An electric current pass through a tungsten filament within the cathode, heating it and producing electrons. Electrons generated by the hot filament are accelerated toward the metal target by a high electric potential in the 20-60 KV range. When electrons collide with a target, they lose kinetic energy, which is radiated as X-rays. All of these procedures take place within an evacuated glass shell. The maximal energy of the generated X-ray photons is restricted by the energy of the incident electrons, which is equal to the applied voltage times the electron charge. The creation of X-rays is a time-consuming procedure. The following relationship determines the highest X-ray frequency and lowest wavelength attainable at a given voltage V [3].

$$eV = h\nu = h\frac{c}{\lambda} \quad \text{………} \ (3.1)$$

Equation 3.1 represents an extreme case in which the electron energy is completely turned into photon energy. However, most electrons endure many collisions and lose a portion of their energy, generating photons with less energy than hν. As a result, the X-ray spectrum produced by the tube contains a wide range of wavelengths (and frequencies), which is referred to as continuous radiation or white radiation. The intensity of the emitted radiation varies constantly with wavelength. The intensity at a fixed wavelength is determined by the operating voltage of the tube as well as the composition of the target metal.

3.2.2 Principle

Powder XRD is a popular method for determining the crystal structure, lattice parameter, stresses, and crystallite size of nanoparticles. Here we have used to determine the crystal structure, crystallite size and d-spacing of the prepared sample. It is the most commonly used indirect approach for estimating crystallite size. The fundamental principle of X-ray diffraction is the constructive interference of monochromatic X-rays with a crystalline material. A cathode ray tube generates these X-rays, which are then filtered to produce monochromatic radiation, collimated to concentrate, and directed toward the sample.

When monochromatic x-rays incident on a crystal, the atomic electrons in the crystal are vibrated. They are accelerated with the same frequency as the incident ray's frequency. These accelerated electrons generate radiation with the same frequency as the incident x-rays in all directions. These radiations may interfere constructively or destructively, resulting in a diffraction pattern (i.e. maxima and minima) in specific directions. A monochromatic x-ray beam with a typical wavelength is impinge on an object in XRD. If Bragg's law (Equation 3.2) is satisfied, the x-rays are diffracted by the crystalline phases in the specimen.

$$n\lambda = 2d \sin\theta \quad \ldots\ldots\ldots\ldots\ldots (3.2)$$

where d is the crystalline phase separation between atomic planes and λ is the x-ray wavelength and n is the integer. The intensity of diffracted x-rays is measured as a function of the diffraction angle 2θ and the orientation of the specimen. This diffraction pattern is used to identify the crystalline phases of the specimen and to measure the crystallite size.

3.2.3 Instrumentation

Deby, Scherrer and Hull developed this method independently. The crystalline material is ground to powder form in this process, demonstrating that the crystallites take random orientation. Powder diffraction measurement equipment has not altered much since it was invented in the late 1940s. The utilization of the minicomputer for control, data gathering, and data processing is the primary difference in modern instrumentation.

A powder X-ray diffractometer mainly consists of an X-ray source (often an X-ray tube), a sample stage, a detector and a method for varying the angle. The X-ray is focused at an angle θ on the sample, while the detector opposite the source measures the intensity of the X-ray it receives at a distance of 2θ from the source route which is shown in figure 3.1. The incidence angle is then gradually increased, while the detector angle always remains 2θ degrees above the source path.

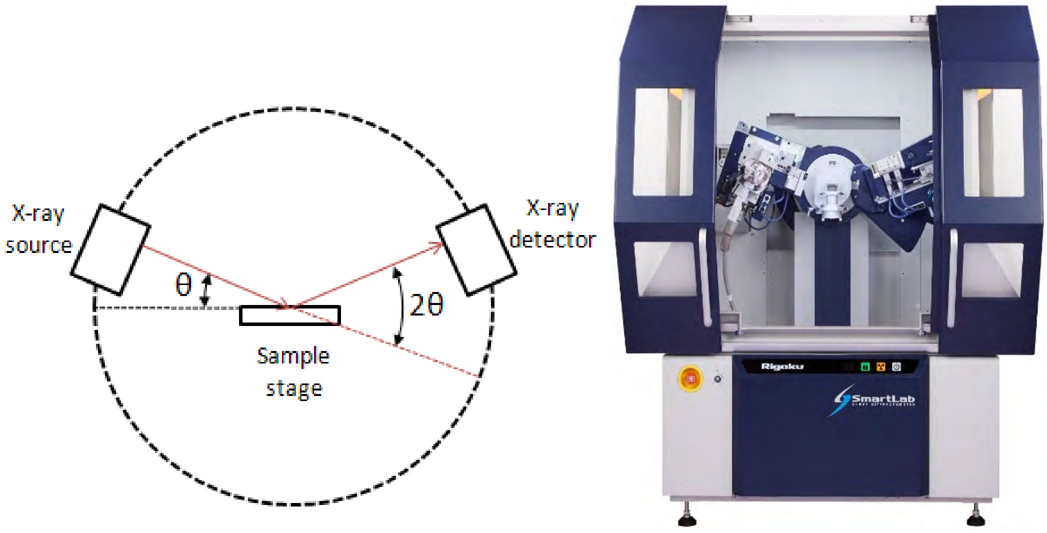

Fig.3.1 Schematic diagram of powder XRD method and photograph of the instrument.

In a cathode ray tube, X-rays are produced by burning a filament to produce electrons, accelerating the electrons toward a target using a voltage, and hitting the target material with electrons. Characteristic X-ray spectra are created when electrons have enough energy to displace inner shell electrons of the target material. These spectra are made up of multiple components, the most prevalent of which being K_α and K_β. K is made up, in part, of $K_{\alpha1}$ and $K_{\alpha2}$. $K_{\alpha1}$ has a slightly shorter wavelength than $K_{\alpha2}$ and twice the intensity. The particular wavelengths are unique to the target substance. The target materials which can be used are Cu, Fe, Mo, Cr. Filtering with foils or crystal monochromators is necessary to generate monochromatic X-rays for diffraction. $K_{\alpha1}$ and $K_{\alpha2}$ have similar wavelengths, hence a weighted average of the two is employed. CuK_α radiation = 1.5418 Å is the most popular target material for single-crystal diffraction. These X-rays are collimated before being directed at the material. The intensity of the reflected X-rays is measured when the sample and detector are rotated. When the incident X-rays impinging on the sample satisfy the Bragg Equation, constructive interference occurs and an intensity peak occurs. This X-ray radiation is recorded and processed by a detector, which transforms it to a count rate, which is then output to a device such as a printer or computer monitor.

An X-ray diffractometer's geometry is such that the sample rotates at an angle θ in the direction of the collimated X-ray beam, while the X-ray detector is mounted on an arm to collect the diffracted X-rays and rotates at an angle of 2θ. A goniometer is the instrument used to maintain the angle and spin the sample. For common powder patterns, data is captured at 2θ angles ranging from 5° to 90°, which are predefined in the X-ray scan.

3.2.4 Experimental

The well-known Debye Scherrer equation (equation 3.3) is used to calculate crystallite size,

$$D = \frac{K\lambda}{\beta \cos\theta} \quad \ldots\ldots\ldots (3.3)$$

where D is the crystallite size, K is the Scherrer constant, λ is the wavelength of X-ray used, β is the "full width at half maximum" of the sharp peaks, and θ is the angle measured. The Scherrer constant (K) in the calculation compensates for particle shape and is commonly assumed to be 0.9 [2]. d-spacing value is calculated using Bragg's law (equation 3.2).

3.2.5 Results and discussion

To study the structure of the prepared sample and to calculate the d-spacing value, X-ray diffraction studies are used. The XRD pattern of GO and rGO is shown in Figure 3.2. Diffraction peaks for GO can be seen at 2θ ~ 10^o (001 reflection) is the characteristic peak and 42.3^o (pdf number: 44-558). d-spacing of GO is calculated to be 9.286 nm. Amla extract was used to reduce the prepared GO. The rGO diffraction peak is displaced from 10^o to 26^o, and the d-spacing is decreased to 3.41 nm. This decrease in d-spacing clearly indicates the elimination of oxygen-containing functional groups between the graphene sheets.

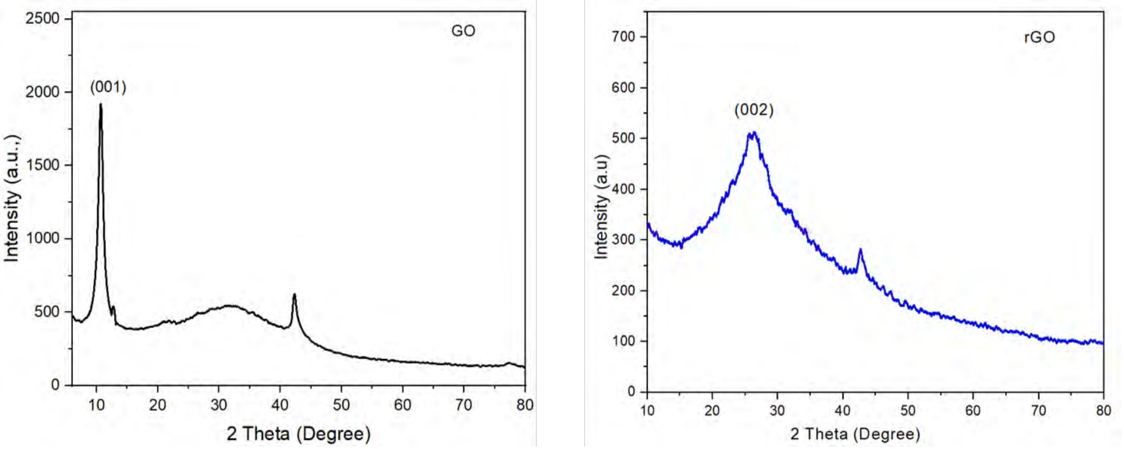

Fig. 3.2 XRD pattern of GO and rGO.

To study the structure of the prepared sample and to calculate the d-spacing value, X-ray diffraction studies are used. The XRD pattern of GO and rGO is shown in Figure 3.2. Diffraction peaks for GO can be seen at 2θ ~ 10° (001 reflection) is the characteristic peak and 42.3° (pdf number: 44-558). d-spacing of GO is calculated to be 9.286 nm. Amla extract was used to reduce the prepared GO. The rGO diffraction peak is displaced from 10° to 26°, and the d-spacing is decreased to 3.41 nm. This decrease in d-spacing clearly indicates the elimination of oxygen-containing functional groups between the graphene sheets.

Figure 3.3 shows the XRD pattern of bare metal oxides: NiO, CuO, ZnO and Co_3O_4 at different fuel ratio. NiO is prepared with fuel amount (amla extract solution) 1mL, 2mL and 3mL. All three samples show peaks at same 2θ value but a slight change in the intensity and width of the peaks. The diffraction peaks are corresponding to rhombohedral structure (JCPDS Number- 22 – 1189). Peaks appearing at 2θ ≈ 37.3°, 43.4°, 62.9°, 75.3°, 79.4° can be indexed as (111), (200), (220), (311), (222) respectively. The average crystallite size of bare NiO is calculated by Scherer's formula and is found to be 21.49 nm, 24.84 nm and 25.7 nm respectively. This increase in crystallite size with increase in fuel quantity is due to increase of flame temperature this will assist the crystal growth [4].

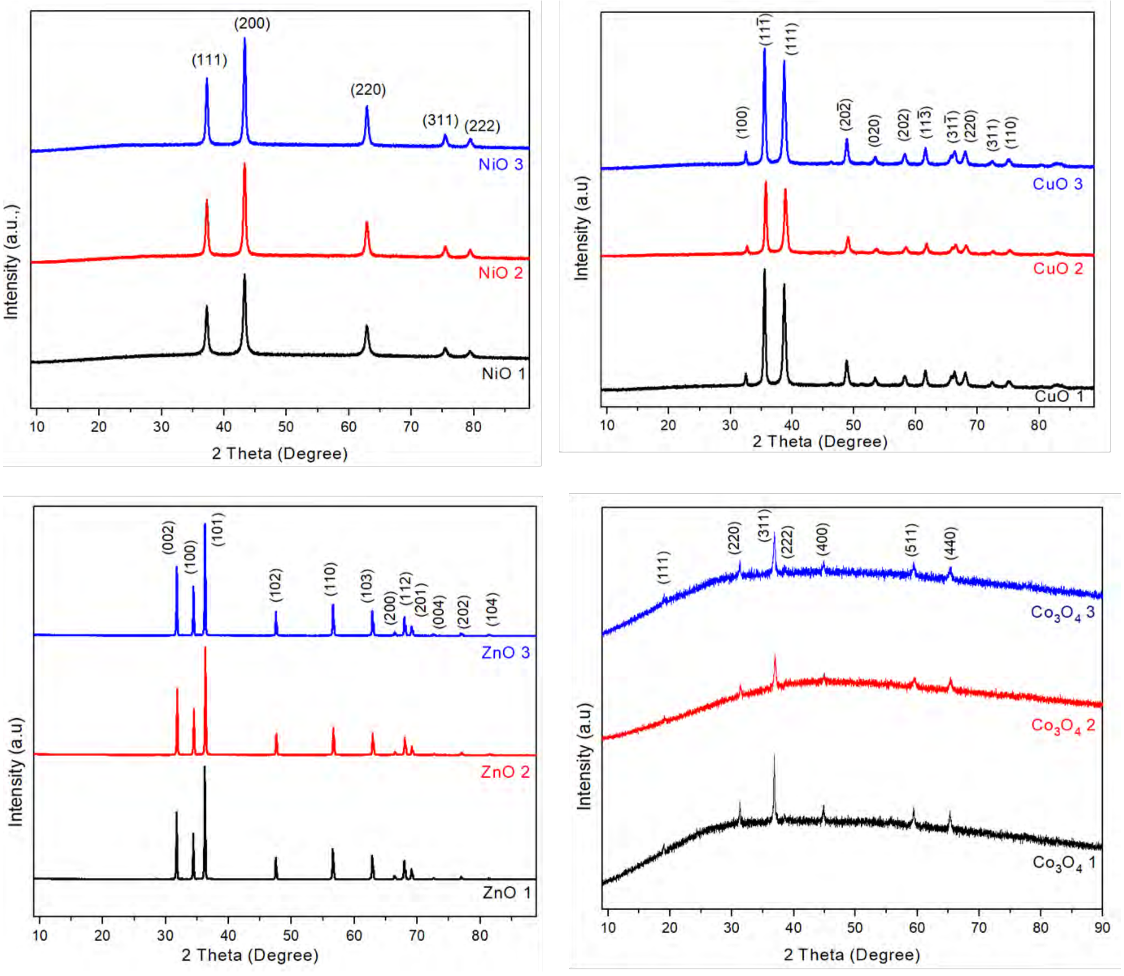

Fig. 3.3 XRD pattern of NiO, CuO, ZnO and Co_3O_4 at different fuel ratio.

CuO is prepared with fuel amount 1mL, 2mL and 3 mL. Here also all the three samples show the same values of 2θ and slightly different intensity and width of peaks. The diffraction peaks are observed at 2θ ≈ 32.6º, 35.7º, 39º, 46.46º, 49.05º, 53.75º, 58.54º, 61.75º, 66.45º, 68.29º, 72.57º, 75.25º, 82.82º and is corresponds to monoclinic structure (JCPDS number 5-661). The average crystallite size of CuO for fuel amount 1mL, 2mL and 3 mL is calculated to be 29.68 nm, 27.25 nm and 21.47 nm respectively.

ZnO is prepared with fuel amount 1mL, 2mL and 3 mL. Here also all the three samples show the same values of 2θ and slightly different intensity and width of peaks. The diffraction peaks are observed at 2θ ≈ 31.8º, 34.5º, 36.3º, 47.6º, 56.6º, 62.9º, 66.5º, 68.05º, 69.19º, 72.5º, 77.04º and is corresponds to hexagonal crystal structure (JCPDS number 36-1451). The average crystallite size of ZnO for fuel amount 1mL, 2mL and 3 mL is calculated to be 60.04 nm, 58.22 nm and 59.80 nm respectively. Initially the crystallite size decreases with increase in the fuel quantity. This is because it is determined by the number of moles of gaseous products released. As the fuel-to-oxidant molar ratio increases, the agglomerates disintegrate and extra heat is transported away from the system, inhibiting particle growth and producing nanoparticles of smaller size [4].

Co_3O_4 is prepared with fuel amount 1mL, 2mL and 3 mL. Here also all the three samples show the same values of 2θ and slightly different intensity and width of peaks. The diffraction peaks are observed at 2θ ≈ 19.11º, 31.5º, 44.96º, 59.58º, 65.4º and is corresponds to cubic structure (JCPDS number 1-1152). The average crystallite size of Co_3O_4 for fuel amount 1mL, 2mL and 3 mL is calculated to be 44.5 nm, 31.07 nm and 29.70 nm respectively.

Figure 3.4 shows the XRD images of composite materials (rGO/NiO, rGO/CuO, rGO/ZnO and rGO/Co_3O_4). All the graphs clearly depicts that the peaks are similar to that of bare metal oxides and the diffraction peaks are observed at same 2θ values. No shift is observed in 2θ values of any of the composite material. This indicates that the GO is well reduced.

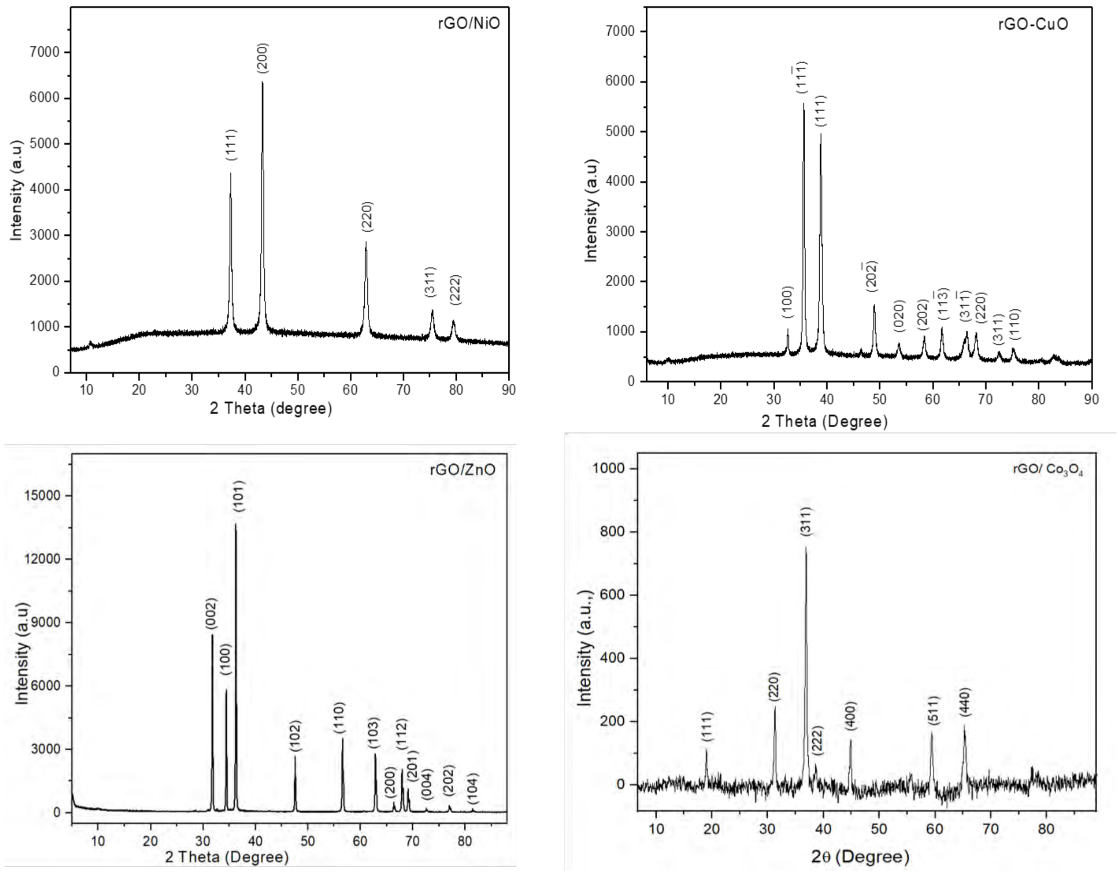

Fig. 3.4 XRD pattern of rGO/NiO, rGO/CuO, rGO/ZnO and rGO/Co_3O_4 composites.

3.3 Fourier transform infrared spectroscopy (FTIR)

3.3.1 Introduction

Fourier transform infrared spectroscopy (FTIR) is a popular method for detecting functional groups in pure substances and mixtures. The FTIR analysis method scans test samples using infrared light to observe chemical characteristics. FTIR is concerned with the vibration of molecules. Each functional group has its own unique vibrational energy, which can be utilized to identify a molecule when all of the functional groups are combined. As a result, FTIR microscopy is ideal for sample identification, multilayer film characterization, and particle analysis.

The vibrational energy of atoms or groups of atoms in a substance is associated with infrared spectroscopy. It is highly impossible that two substances might have the same infrared spectrum. As a result, the FTIR spectrum is referred to as a molecule's fingerprint. The FTIR spectra of nanoparticles differs significantly from that of the bulk material due to their extremely high surface-to-volume ratio. Furthermore, the huge number of atoms that make up the surface of nanoparticles might influence the vibrational spectra, which has distinct properties from that of the bulk.

FTIR analyses organic and inorganic substances quantitatively and qualitatively. FTIR creates an infrared absorption spectrum to identify chemical bonds in a molecule. The spectra generate a sample profile, a unique molecular fingerprint that may be used to screen and scan samples for a variety of components. FTIR is a powerful analytical tool for discovering functional groups and analysing covalent bonding data. FTIR is an infrared spectroscopy-based equipment. It is the most recent and favoured form of dispersive spectrometer. Its high precision, accuracy, speed, improved sensitivity, ease of operation, and sample non-destructiveness are all reasons for its success.

3.3.2 Principle

Infrared spectroscopy is based on the idea that molecules vibrate at certain frequencies. It ranges from 4000 to 400 cm^{-1}. These frequencies are in the infrared region of the electromagnetic spectrum. When IR radiation incident on a sample, it absorbs radiation at frequencies similar to its molecular vibration frequencies while transmitting radiation at other frequencies. Infrared spectrometers measure the frequencies of absorbed radiation and produce an infrared spectrum, which is a plot of absorbed energy against frequency. Because diverse materials have dissimilar vibrations and produce distinct infrared spectra, a specific molecule can be identified. FTIR gives both qualitative and quantitative information of a sample.

3.3.3 Instrumentation

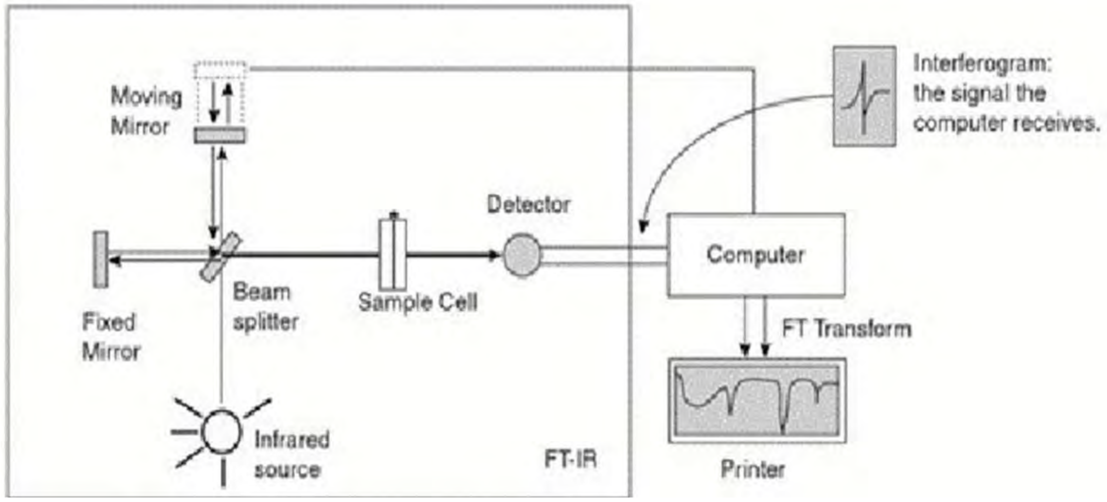

Fig. 3.5 Schematic diagram of FTIR spectroscopy.

FTIR manufacturers utilize a variety of interferometer designs. The Michelson interferometer is the oldest and possibly most frequent form of interferometer in use today. It is named after Albert Abraham Michelson (1852-1931), who invented the interferometer in the 1880s and was later awarded the Nobel Prize in Physics for his findings with it [5]. Figure 3.5 depicts the optical design of a Michelson interferometer. Four arms make up the Michelson interferometer. In Figure 3.5, the bottom arm has the infrared source and a collimating mirror that collects the light from the source and aligns its rays. A fixed mirror is located on the left arm of the Michelson interferometer. This is in contrast to the interferometer's top arm, which contains a moving mirror that can move up and down. The sample and detector are located in the interferometer's right arm. An optical device known as a beam splitter is at the heart of the interferometer. A beam splitter is intended to transmit some of the incident light while reflecting some of the incident light. The light transmitted by the beam splitter is directed toward the fixed mirror. In Figure, while the light reflected by the beam splitter is directed toward the moving mirror. The light beams that reflect from these mirrors return to the beam splitter and are recombined into a single light beam that leaves the interferometer, interacts with the sample and then reaches the detector, which is Fourier transformed into a frequency spectrum by a computer - a function of signal intensity versus frequency or wavenumber. The photograph of FTIR spectroscopy is shown in figure 3.6.

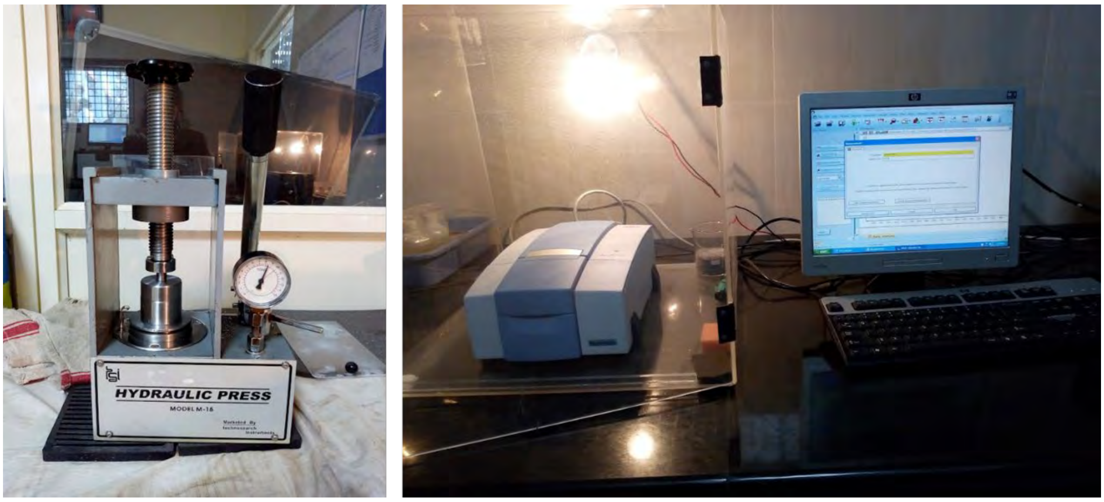

Fig. 3.6 Photographs of Hydraulic press for Pellet making and FTIR spectroscopy.

3.3.4 Experimental

Transmission is the simplest technique, but it necessitates the most sample preparation. The interferometer's light passes through a sample, with the desired beam path through the sample determined by the state (solid, liquid, or gas). Solids can be pressed using either a KBr pellet containing the sample or a diamond anvil cell. The sample for liquids can be injected into a liquid cell or applied to an IR transparent window or card. After being introduced into a gas cell, gases can be monitored. To avoid condensation inside the cell, gas cells are frequently heated.

Since KBr is optically transparent to light in the IR measurement region, it is utilized as a carrier for the IR spectrum sample. So that there would be no interference with absorbance. In order to prepare pellets, the sample concentration in KBr should be between 0.2% and 1%. Because the pellet is thicker than a liquid film, a lower concentration in the sample is needed (Beer's Law). A concentration that is too high usually makes it difficult to obtain clear pellets. The IR beam is completely absorbed or scattered by the sample, resulting in very noisy spectra.

3.3.5 Results and discussion

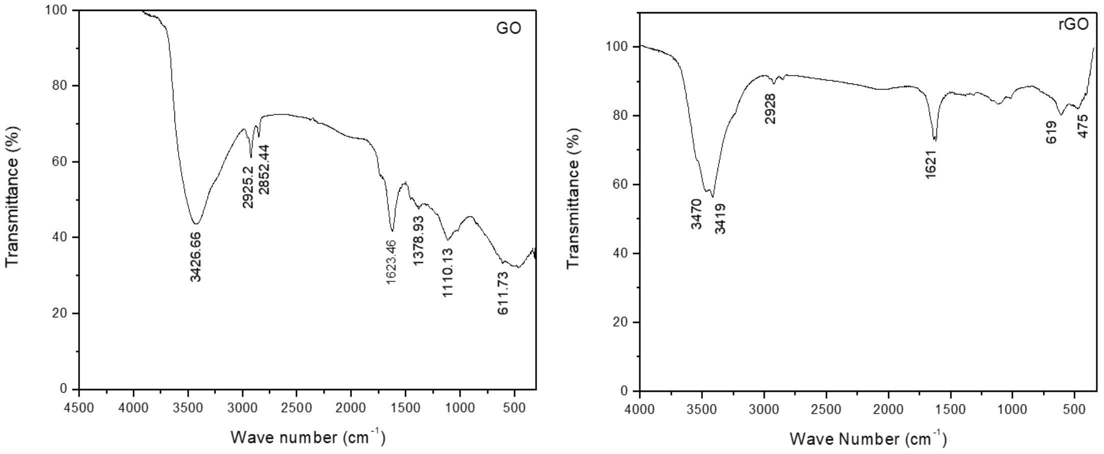

Fig. 3.7 FTIR spectra of GO and rGO.

The functional groups of GO and rGO are studied using FTIR spectra which are shown in figure 3.7. FTIR spectra of GO shows a large peak at 3426 cm^{-1}, which is caused by the existence of an O-H stretching vibration in the hydroxyl group. This peak can also be detected in the rGO spectra, but at a lower intensity. This shows that the partial elimination of the hydroxyl group. Small peaks at 2900 cm^{-1} imply heterocyclic compound C-H stretching. Carbonyl groups in the molecule have a strong bond at 1623 cm^{-1}. The appearance of a signal at 1110 cm^{-1} suggests that the C-O molecule is stretching.

rGO's FT-IR spectra is quite close to that of GO, but it can be seen that the intensity of all the peaks is lessened. There are no new peaks visible after the reduction of GO. This means that amla and its derivatives are fully removed by rGO washing. Based on these insights, we can note that the majority of the oxygen-containing groups in GO nanosheets are removed by using amla as a reducing agent in the reduction process.

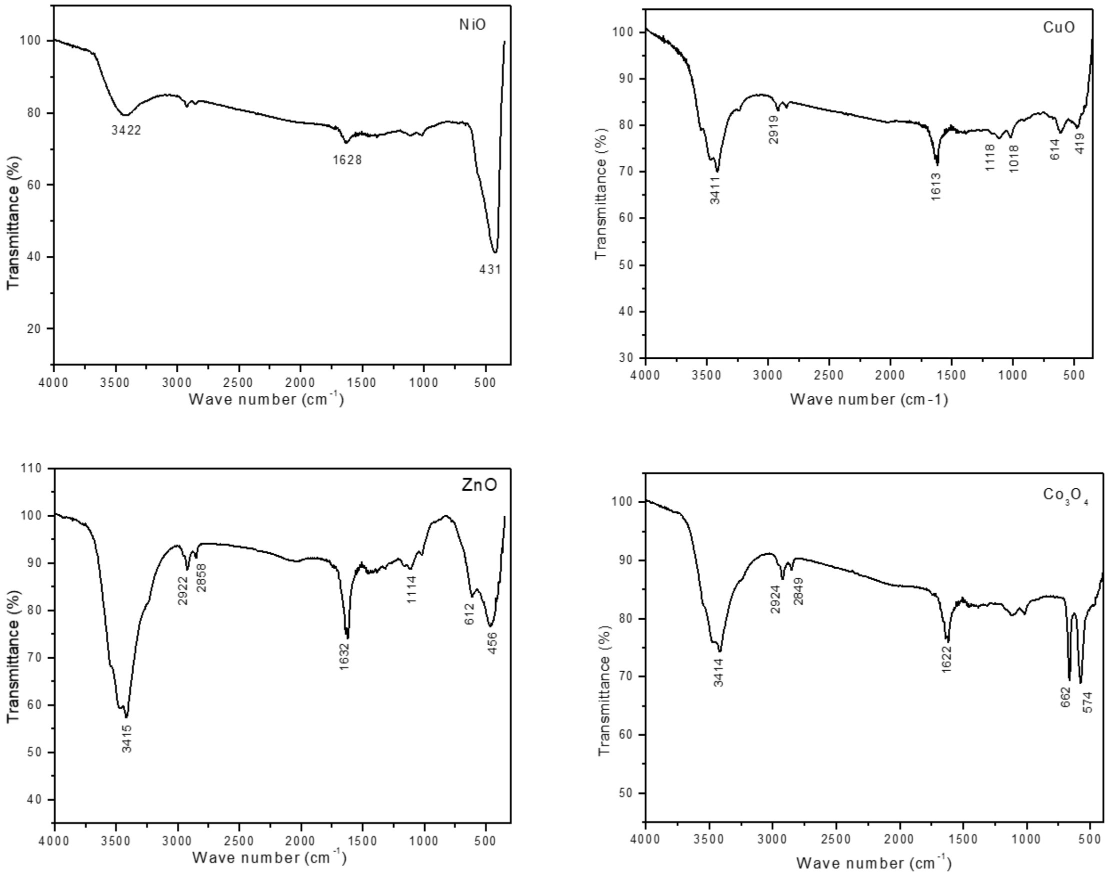

Fig. 3.8 FTIR spectra of bare NiO, CuO, ZnO and Co_3O_4.

Figure 3.8 shows the FTIR spectra of bare NiO, CuO, ZnO and Co_3O_4. FTIR spectra of NiO shows a broad peak at 3422 cm^{-1} confirms the presence of O-H stretching vibration of hydroxyl group. A small peak at 1628 cm^{-1} attributed to carbonyl group. A high intense peak at 435 cm^{-1} supports the presence of Ni-O stretching vibrations [6].

FTIR spectra of CuO having a broad peak at 3411 cm^{-1} which attributes to the presence of O-H stretching vibration of hydroxyl group. The peak at 2919 cm^{-1} attributed to O-H stretching vibration. 1613 cm^{-1} attributed to carbonyl group. 614 cm^{-1} 419 cm^{-1} confirms the presence of Cu-O. It is the characteristic stretching vibration of Cu-O [7].

FTIR spectra of ZnO is having peak at 3415 cm^{-1} indicates the presence of O-H group, Carboxylic group form the peak at 2922 cm^{-1}. The stretching vibration of C=O form the aldehyde group at 1632 cm^{-1}. The peak at 456 cm^{-1} s the characteristic peak of Zn-O stretching vibration [8].

FTIR spectra of Co_3O_4 has an intense peak at 3414 cm^{-1} confirms stretching vibration of O-H group. Carboxylic group form the peak at 2924 cm^{-1}. Narrow peak at 1622 cm^{-1} attributes to C=C stretching vibration. Two strong peaks at 662 $cm^{-1}$and 574 cm^{-1} confirms the presence of Co_3O_4 [9].

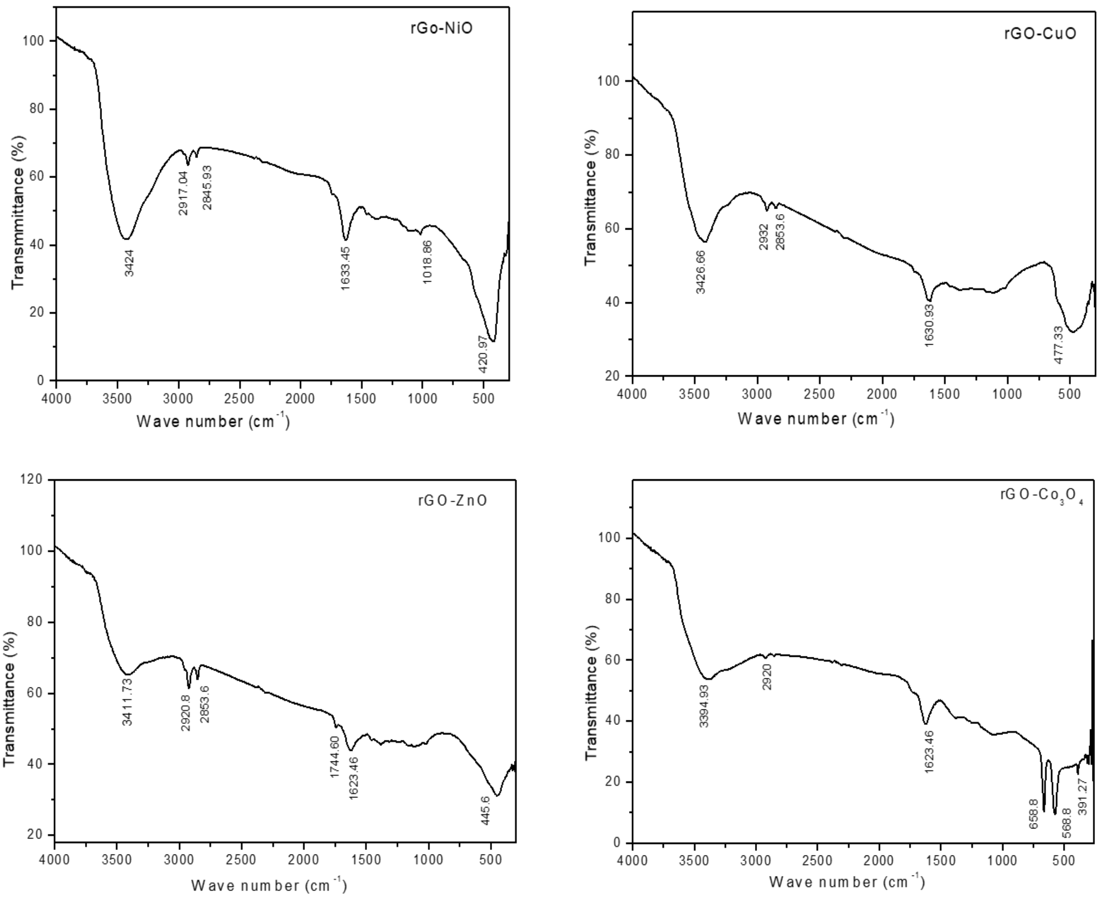

Fig. 3.9 FTIR spectra of rGO/NiO, rGO/CuO, rGO/ZnO and rGO/Co_3O_4 composites.

The FTIR spectra of the rGO/NiO, rGO/CuO, rGO/ZnO and rGO/Co_3O_4 are shown in figure 3.9. The FTIR spectra of the rGO/NiO composite is quite similar to that of GO, although the strength of all peaks has been reduced. The occurrence of a peak at 435 cm^{-1} supports the presence of Ni-O stretching vibrations. This indicates that the reduction of GO has occurred in the composite material. Similarly, the composite materials rGO/CuO, rGO/ZnO and rGO/Co_3O_4 are also having these peaks but with decreased intensity as that of the GO. This indicates that GO is well reduced. It can be clearly seen that the peaks at the lower wave number region confirms the presence of metal oxides.

3.4 Raman spectroscopy

3.4.1 Introduction

Raman spectroscopy is a type of spectroscopy that relies on the inelastic scattering of monochromatic light, typically from a laser source. The frequency of pictures in monochromatic light changes due to inelastic scattering as they contact with the sample. Laser light photos are absorbed by the sample and then reemitted. The Raman effect occurs when the frequency of the reemitted photons is shifted up or down in contrast to the original monochromatic frequency. The molecule will be excited from the ground state to a virtual energy level, then relax into a vibrationally excited state, resulting in Stokes Raman scattering. If the molecule was already in a high vibrational energy state, the Raman scattering is referred to as anti-Stokes Raman scattering [10].

Raman spectroscopy is based on the phenomenon known as Raman scattering, which was discovered in 1928 by the Indian scientist Raman [2]. The inelastic scattering of monochromatic photons (UV, visible, or near IR) by a material is measured using Raman spectroscopy. Raman scattering has been shown to be sensitive to isotope composition, crystal structure, biomolecular interactions, and noncovalent molecule interactions.

As long as the selection rules allow, the energy difference between the scattered and incident light, known as the Raman shift (typically expressed by a wave number), equals the vibrational or phonon frequencies of the sample. The spectrum is commonly shown as the difference between the intensity of Raman scattered light and the Raman shift. Raman shifts generally arise in the hundreds to thousands of per centimeter range. If the incident light is visible, the detected signal is usually apparent. The Stokes-Raman signal is most frequently detected and has a lower energy (or frequency) than the incident light frequency [2].

Raman spectrophotometers are classified into two major categories based on their application: lab-based spectrophotometers and in-field, in-situ, or down-field use Raman spectrophotometers, which comprise portable and hand-held devices as well as remote or stand-off systems. The essential principle is the same in each situation, and these systems varied by the adaptability of an instrument, as well as the size and relative cost of its components. On-site Raman spectrophotometers use smaller components. Raman spectrophotometers for on-site analysis and research are available in benchtop, handheld, portable, remote, and stand-off configurations. In the late 1980s, commercial Fourier Transform-Raman spectrophotometers (FT-Raman) were introduced to improve the detecting system capable of overcoming the limits of charge-coupled devices and other detectors for working in the near-IR region. [11].

3.4.2 Principle

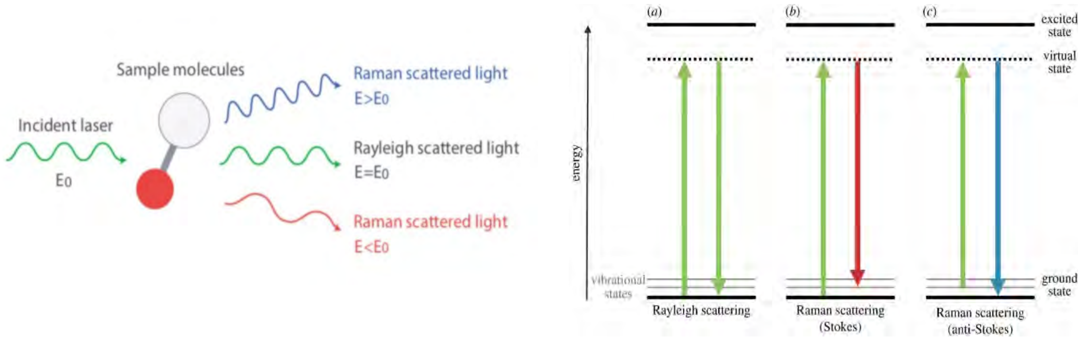

Fig.3.10 Schematic representation of scattering of light and Energy level diagram.

The great majority of photons are dispersed or scattered at the same energy as the incident photons when light interacts with molecules in a gas, liquid, or solid. The Raman effect is based on light scattering, which includes elastic scattering at the same wavelength as the incident light as well as inelastic scattering at different wavelengths caused by molecular vibrations. Rayleigh scattering is the elastic scattering, whereas Raman scattering is the inelastic scattering.

The Raman shift is the difference in energy between incident and dispersed light. The Raman spectrum is represented by the vertical axis intensity of scattered light and the horizontal axis wavenumber of the Raman shift. The schematic representation is shown in the figure 3.10.

3.4.3 Instrumentation

Raman spectroscopy is becoming more frequent in pharmaceutical facilities. Over the last decade, technological improvements have resulted in the development of increasingly smaller Raman spectrometers that require only a single tabletop of laboratory space [12].

A photon interacts with a molecule through Rayleigh scattering (elastic scattering), polarizing the electron cloud and bringing it to a "virtual" energy state. This is incredibly brief (on the range of 10^{-14} seconds), and the molecule quickly returns to its ground state, emitting a photon. When this is released in any direction, it scatters. However, because the molecule is returning to its original form, the energy released in the photon must be the same as the energy from the initial photon. As a result, the wavelength of the scattered light is the same. Rayleigh scattering thus provides no information about the sample's vibrational energy levels.

Fig.3.11 Instrumentation and photograph of Raman spectroscopy.

Raman scattering differs from other types of scattering in that it is inelastic. Light photons lose or gain energy during the scattering process, causing their wavelength to increase or decrease as shown in figure 3.11. If a molecule is excited from a ground state to a virtual state and then comes back to a ground state vibrational level, then a scattered photon has less energy than the incident photon and hence has a longer wavelength. This is known as Stokes scattering. If the molecule is in a vibrational state before scattering and subsequently returns to its ground state, the scattered photon has greater energy and thus a shorter wavelength. This is referred to as anti-Stokes scattering [12].

a) Laser excitation: A laser of appropriate strength, wavelength, and stability is used to illuminate the sample. Examples include diode pumped solid state lasers (most often 1064 nm and 532 nm, although many more wavelengths are also available) and stabilized NIR diode lasers (usually 780-820 nm) with powers ranging from a few tens of mW to 1 W. These lasers are generally small, sturdy, and dependable.

b) Excitation delivery to sample: The exciting laser light can be delivered to the sample by a typical optical system of mirrors and lenses, or via fiber optic cables that can span tens of meters (due to the absorption in optical fiber, this is not possible with mid-IR absorption spectroscopy). A lens system directs the exciting light onto or into the sample and collects the Raman scattered light that results.

c) Collecting and filtering scattered light: Due to the weakness of the effect, efficient collection of scattered light is critical in Raman spectroscopy. To achieve a large collecting angle, the collection optics (fiber optics) must be placed as close to the sample as feasible and have a big aperture. The collected scattered light must next be spectrally filtered to remove the Rayleigh scattered component, or else the Raman signal will be swamped. This function can be performed using a variety of optical narrow band rejection or edge filters.

d) Detectors: To detect Raman scattered light, a sensitive, low noise detector is required. Cooled charged couple device (CCD) cameras are the detector of choice for UV-NIR excitation slow scan. However, such a detector is often the most expensive component of a Raman system. Recent advancements in indium gallium arsenide phosphide array detectors show potential for IR stimulated Raman spectroscopy.

e) Spectral analysis: The captured Raman light must next be analyzed spectroscopically. A low stray light, dispersive spectrometer with a bandpass filter arrangement or a Fourier transform (FT) type spectrometer can be used for this. A dispersive spectrometer is typically recommended for excitation wavelengths ranging from the ultraviolet to 820 nm, but an FT system is typically required for excitation wavelengths more than 820 nm. For example, 1064 nm Nd: YAG (Neodymium–doped yttrium–aluminium–garnet).

3.4.4 Experimental

All Raman spectroscopy was done using Horiba Scientific Raman spectrometer, with dry samples on a glass substrate. Wavelength of the laser source used was 532 nm. G band and D band are located and the ratio of intensity of D band to G band i.e., I_D/I_G ratio was noted.

3.4.5 Results and discussion

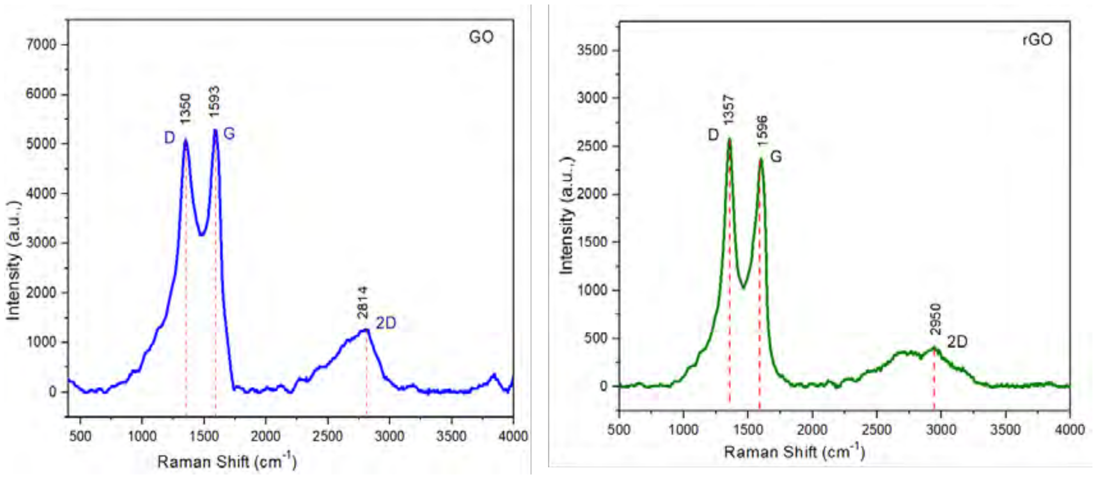

Fig. 3.12 Raman spectra of GO and rGO.

Raman spectroscopy is an important method for characterizing graphite and graphene materials because it is highly sensitive to the material's electrical structure [13]. It allows us to explore the bonding properties of diverse carbon compounds in a non-destructive manner. Figure 3.12 depicts the Raman spectra of GO and rGO. D and G bands exist at 1350 cm^{-1} and 1593 cm^{-1}, respectively. The D band is a result of structural defects and disorder, whereas the G band is formed by the E_{2g} mode created by first-order Raman scattering of sp^2 carbon atoms. The I_D/I_G ratio of GO is 0.956, and the rGO ratio is 1.08. This increase in the I_D/I_G ratio after reduction by amla extract implies the presence of disordered domains during GO reduction. This increase in the I_D/I_G ratio value is consistent with the observations made for other reducing agents.

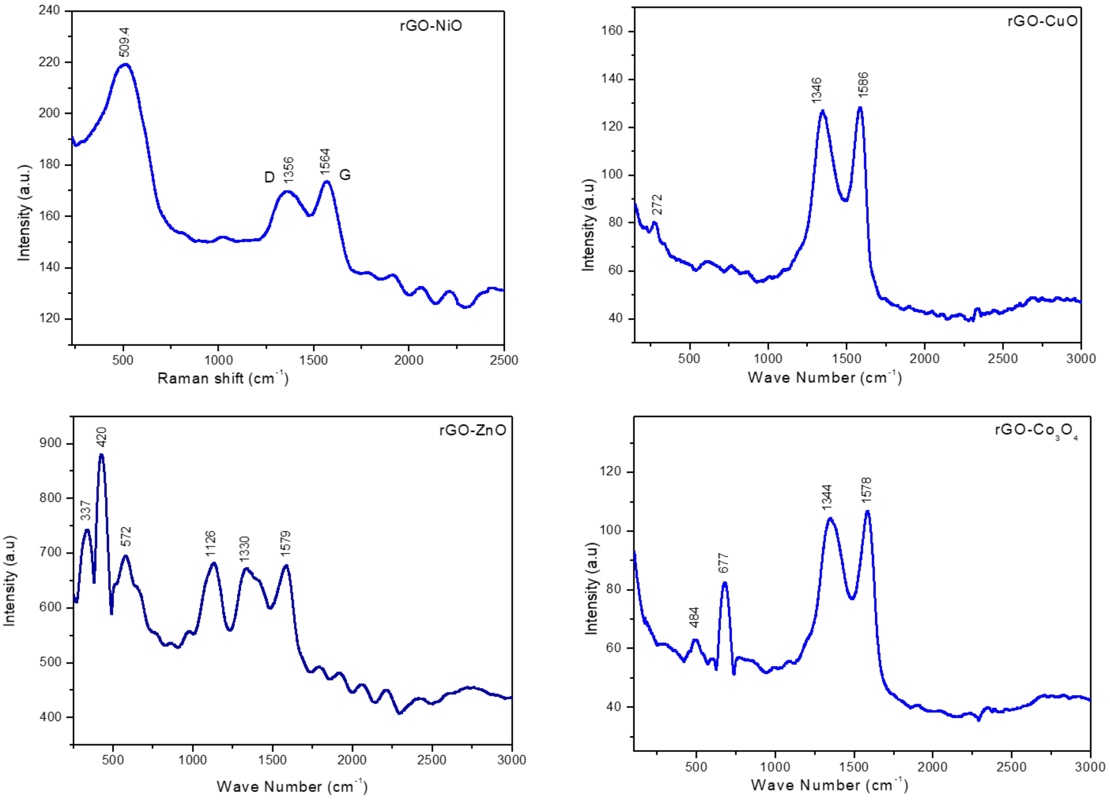

Fig. 3.13 Raman spectra of rGO/NiO, rGO/CuO, rGO/ZnO and rGO/Co$_3$O$_4$ composites.

Figure 3.13 depicts the Raman spectra of rGO/NiO composite. In the graph above, the peak at 1564 cm^{-1} is referred to as the G band, and it is caused by the E_{2g} phonon mode of sp^2 carbon atoms. The peak at 1356 cm^{-1} is attributable to the D band, which reveals the disorderness in the sample. The 2D band which is created by second order zone boundary phonons, has a less powerful peak at 2817 cm^{-1}. The presence of G and D bands in this sample clearly confirms the presence of rGO in the composite. The peak in the composite at roughly 505.88 cm^{-1} is attributable to NiO shaking peaks. When the Raman spectrum of rGO/NiO composite is compared to the Raman spectrum of GO, the G band in the composite material is slightly moved towards the lower wave number side due to de-oxygenation in GO [14, 15]. This definitely indicates that the GO has been reduced to rGO. The intensity ratio of D band and G band (I_D/I_G ratio) calculated for rGO/NiO composite is about 0.97.

Raman spectra of rGO/CuO composite is shown in figure 3.12. It shows two distinct bands at 1346 cm^{-1} (D-band) and 1586 cm^{-1} (G-band), respectively. The D-band is connected with in-plane bond stretching motion of pairs of carbon sp^2 atoms (the E_{2g} phonons) and exhibits sp^2 domain defects, whereas the G-band is associated with A_{1g} symmetry breathing modes or -point phonons. The I_D/I_G ratio increased from 0.956 in the GO to 0.985 in the composite. This implies that the defect concentration in the GO has got increased during the composite material's production process. The Raman studies of the CuO sample has a band at 272 cm^{-1}, which is in good agreement with earlier findings [16, 17].

Raman spectra rGO/ZnO composite is shown in figure 3.12. Along with D band and G band at 1330 cm^{-1} and 1579 cm^{-1}, ZnO has characteristic peaks at 572 cm^{-1}, 420 cm^{-1} and 337 cm^{-1}. The Raman shift of 443 cm^{-1} corresponds to ZnO nonpolar optical phonons (E2), while the Raman shifts of 337 cm^{-1} and 572 cm^{-1} correspond to transversal optical (TO) modes with A_1 symmetry and longitudinal optical (LO) modes, respectively. The second-order modes are found between 1050 and 1200 cm^{-1} [18]. The I_D/I_G ratio is calculated to be 0.99.

Raman spectra of rGO/Co_3O_4 is shown in figure 3.12. Here D band is observed at 1344 cm^{-1} and G band is observed at 1578 cm^{-1}. The peaks attributed to 484 cm^{-1} E_g active mode and 677 cm^{-1} attributed to A_{1g} active mode of Co_3O_4 [9]. The I_D/I_G ratio has been calculated and it is found to be 0.97.

3.5 Scanning electron microscopy

3.5.1 Introduction

Max Knoll and Ernst Ruska devised the electron microscope in Berlin, Germany in 1931. They developed electron microscopes in order to obtain higher resolution images than an optical microscope could provide. Optical microscopes have a theoretical resolution limit of 200 nanometers, while by 1944, SEMs had a theoretical resolution limit of just 2 nanometers. This implies they'll be able to capture higher detailed photographs of objects than optical microscopes can.

Scanning electron microscopes (SEM) have become powerful and adaptable tools for material characterisation, particularly in recent years as the size of materials utilized in many applications has been shrinking. SEM is a form of electron microscope used for investigating the surfaces of solid objects. It employs a beam of focussed electrons of relatively low energy as an electron probe that is scanned over the specimen on a regular basis. It creates detailed, enlarged pictures of objects by scanning their surfaces.

SEM generates a variety of signals at the surface of solid specimens by using a focussed beam of high-energy electrons. The signals produced by electron-sample interactions provide information about the sample such as its exterior morphology (texture), chemical composition, and the crystalline structure and orientation of the materials that comprise the sample. In most applications, data are collected across a specific area of the sample's surface, and a 2-dimensional image displaying spatial changes in these properties is generated. Using traditional SEM techniques, areas spanning in width from 1 cm to 5 microns can be scanned in scanning mode. SEM can efficiently characterize objects down to a few nanometres in resolution, with image magnifications ranging from 10 to over 300,000. SEM can provide useful information on chemistry, crystal orientation, and internal stress distribution in addition to surface topography [1].

3.5.2 Principle

SEM works by directing an electron beam at a sample target and collecting the signals produced by their interaction. The electron beam scans the material in a raster pattern in scanning electron microscopy. The electron source first generates electrons at the top of the column. These are emitted when the thermal energy of the source material exceeds the work function. The positively charged anode then accelerates and attracts them. The entire electron column must be placed in vacuum. The electron source, like all other components of an electron microscope, is sealed inside a specific chamber to maintain vacuum and protect it from contamination, vibrations, and noise. Many kinds of signals are formed when an electron beam (energy 5-30 KeV) impinges on a specimen, including secondary electrons (SEs) and back scattered electrons (BSEs). When electrons contact with the positively charged nucleus, they are scattered at huge degrees (from 0° to 180°). These elastically scattered electrons are commonly referred to as BSEs. Some electrons scatter inelastically as a result of kinetic energy loss during interactions with orbital shell electrons. Incident electrons have the potential to knock weakly bound conduction electrons out of the sample. SEs are the name given to these electrons. SEs and BSEs are commonly utilized for SEM topography imaging. When a negative voltage is given to the collector screen, only BSEs signal is recorded while low-energy SEs are repelled. The electrons caught by the scintillator/photomultiplier are amplified and used to generate a SEM image [2].

3.5.3 Instrumentation

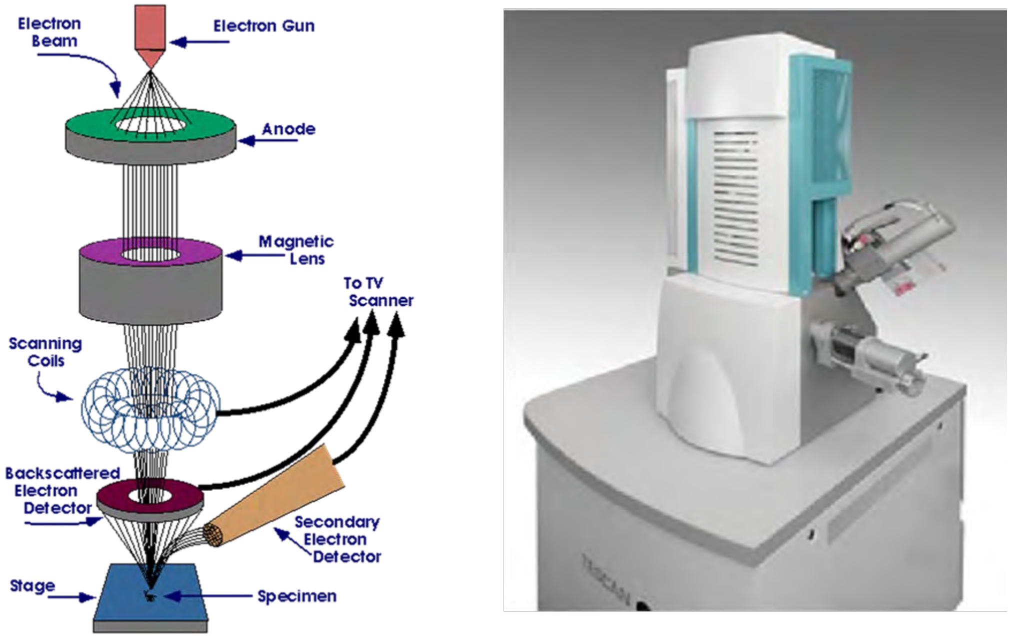

Fig. 3.14 Schematic diagram and Photograph of SEM.

The schematic diagram and a photograph of a SEM is shown in the figure 3.14. An electron beam is thermionically emitted from an electron gun fitted with a tungsten filament cathode in a standard SEM. Tungsten is commonly used in thermionic electron guns because it has the greatest melting point and lowest vapor pressure of any metal, allowing it to be electrically heated for electron emission, and because it is inexpensive. Other types of electron emitters include lanthanum hexaboride (LaB6) cathodes, which can be used in a typical tungsten filament SEM if the vacuum system is updated, and field emission guns (FEG), which can be cold-cathode emitters or thermally assisted Schottky emitters covered in zirconium oxide.

The magnetic lens, often known as the condenser lens, is a SEM's second component. It is used in order to focus the electron beam that the electron gun emits. The electrons are compressed as they pass through the lens, which is comprised of wire coils that produce an electromagnetic field. One or two condenser lenses focus the electron beam, which has an energy range of 0.2 KeV to 40 KeV. The beam is deflected in the x and y axes by pairs of scanning coils or deflector plates in the electron column, often in the final lens, it scans in a raster fashion over a rectangular region of the sample surface.

The interaction volume, which is a teardrop-shaped area of the specimen that extends from less than 100 nm to around 5 μm into the surface, is where the electrons from primary electron beam lose energy when they repeatedly interact in random scattering and absorption. The size of the interaction volume is determined by the landing energy of the electron, the atomic number of the specimen, and the density of the specimen. The energy exchange between the sample and the electron beam causes high-energy electrons to be reflected by elastic scattering, secondary electrons emitted by inelastic scattering, and electromagnetic radiation emitted, all of which can be detected by specialized detectors. The beam current absorbed by the specimen can also be monitored and used to generate pictures of the specimen current distribution. Different types of electronic amplifiers are employed to amplify the signals, which are shown as brightness fluctuations on a computer monitor (or, for vintage models, on a cathode-ray tube). The resulting image is a distribution map of the intensity of the signal being emitted from the scanned area of the specimen since each pixel of computer video memory is synced with the position of the beam on the specimen in the microscope. Most recent instruments acquire digital images whereas earlier microscopes used film to capture images.

3.5.4 Experimental

The surface morphology of synthesized samples was studied by SEM images using VEGA3 TESCAN microscope.

3.5.5 Results and discussion

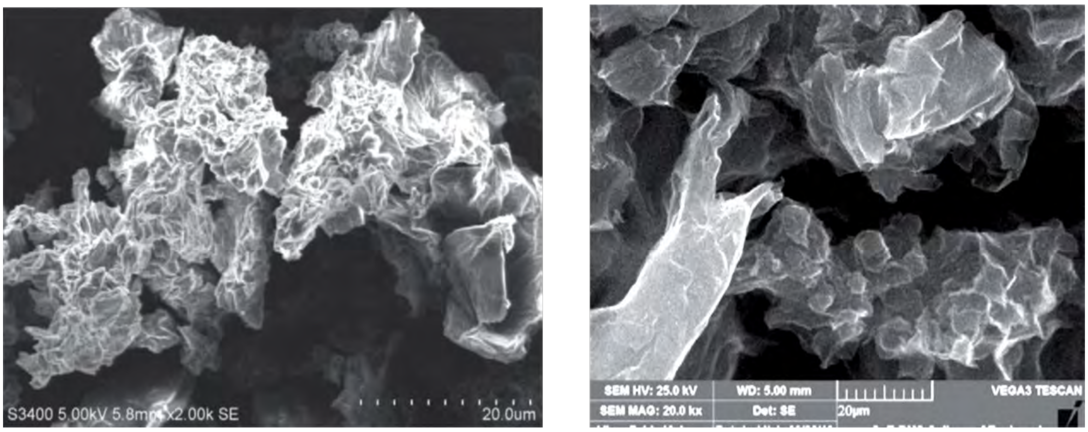

Fig. 3.15 SEM images of GO and rGO

SEM images provide the descriptions of the morphological studies. The SEM image of GO and rGO are depicted in the figure 3.15. These figures illustrate that the surface morphology of GO is wrinkled. It is made up of clusters of closely grouped wrinkled sheets that have been assembled randomly. These wrinkled GO sheets have been loosely connected to one another.

SEM image of rGO depicts that there is no longer much curl, but there is still some surface wrinkling. The rGO is stacked in a few layers. The partial folding of sheet borders minimizes the total surface energy of the sheets [19]. This variation in morphology ensures that the structure is altered after reduction process.

SEM image of bare NiO is depicted in the above figure 3.16. SEM was used to examine the surface morphological properties of produced nanoparticles. The data show that the NiO nanoparticles are spherical in shape. We can see that the particles are strongly agglomerated and form a cluster of nanoparticles. The presence of certain bigger nanoparticles could be attributable to the fact that NiO nanoparticles agglomerate due to their high surface energy and surface tension of the ultrafine nanoparticles.

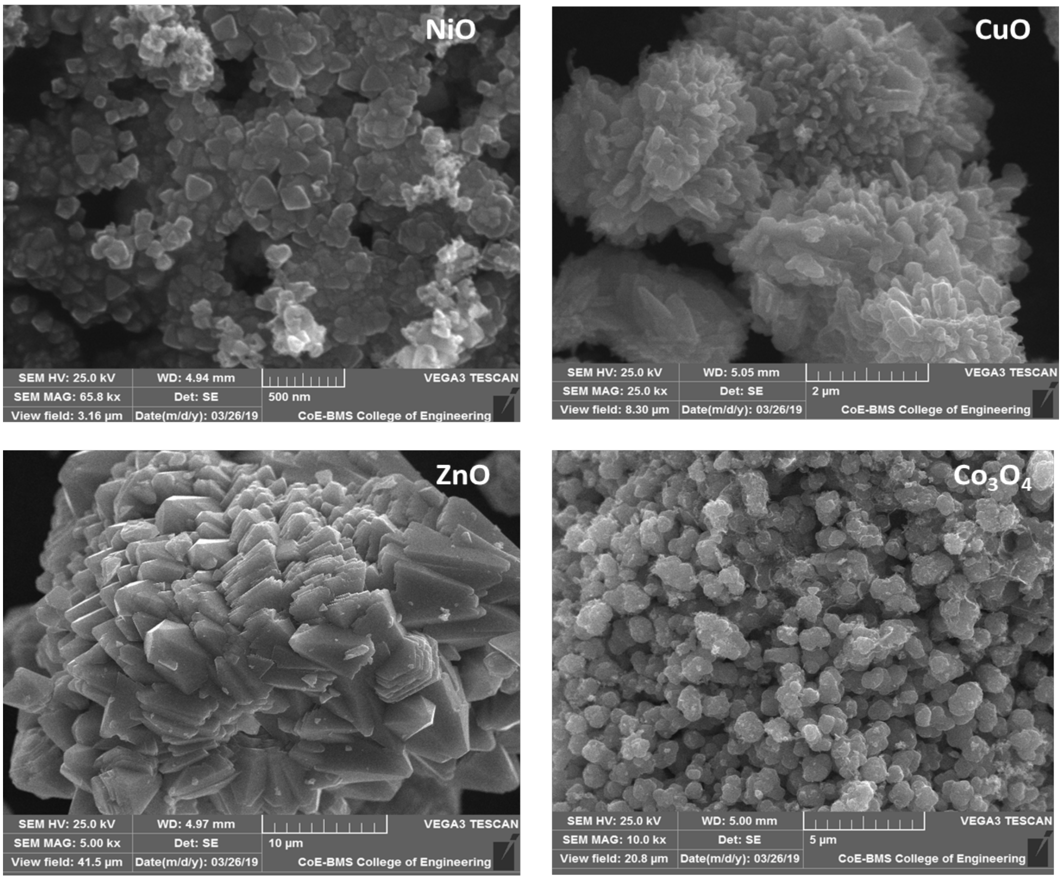

Fig. 3.16 SEM images of bare NiO, CuO, ZnO and Co_3O_4.

SEM image of bare NiO is depicted in the above figure 3.16. SEM was used to examine the surface morphological properties of produced nanoparticles. The data show that the NiO nanoparticles are spherical in shape. We can see that the particles are strongly agglomerated and form a cluster of nanoparticles. The presence of certain bigger nanoparticles could be attributable to the fact that NiO nanoparticles agglomerate due to their high surface energy and surface tension of the ultrafine nanoparticles.

Figure 3.16 shows the SEM image of the CuO. A flower-like hierarchical architecture can be seen, and the one-of-a-kind nanoflowers are assembled by ultrathin nanosheets. These nanosheets, however, are closely staggered with respect to each other.

SEM image of ZnO is depicted in the figure 3.16. A cluster of discs of hexagonal and other shapes are observed. These cluster of discs are having common coupling base.

Figure 3.16 depicts the morphology of prepared Co_3O_4 nanospheres that were seen with numerous, uniform-sized Co_3O_4 nanosphere agglomerated together.

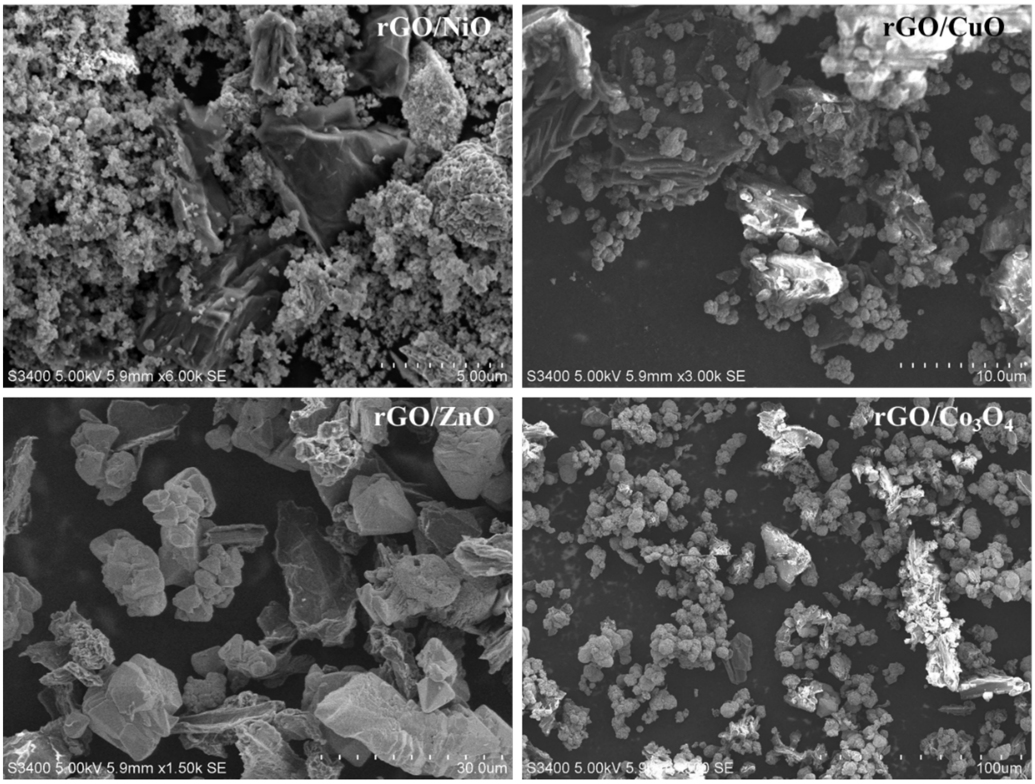

Fig. 3.17 SEM images of rGO/NiO, rGO/CuO, rGO/ZnO and rGO/Co_3O_4 composites.

Figure 3.17 depicts the SEM image of rGO/NiO composite material. Here it can be clearly seen that NiO nanoparticles are present on partially wrinkled surface of rGO. NiO nanoparticles decorated surface of rGO will increase the effective surface area and prevents the agglomeration and restacking of graphene layers. Similarly, CuO, ZnO and Co_3O_4 are also decorated on the partially wrinkled rGO surface.

3.6 Transmission electron spectroscopy

3.6.1 Introduction

A beam of highly energetic electrons is used in transmission electron microscopy (TEM), a microscopy method, to pass through a specimen with a nanometer-thickness. During the interaction of the electron beam with the specimen, data on the many characteristics of the specimen, including but not limited to the materials size, shape, crystallinity, composition, and elemental mapping, can be collected.

The TEM uses electrons rather than light to carry out the same fundamental operations as the light microscope. The best resolution feasible for TEM images is many orders of magnitude better than that from a light microscope because the wavelength of electrons is significantly shorter than that of light. As a result, TEMs may show even the tiniest details of interior structure, even at the level of individual atoms.

A TEM was first put into commercial production in 1936 in the UK by the Metropolitan Vickers company. However, the German Siemens Company's 1938 prototype, which had a spatial resolution of 10 nm, was responsible for the first regular manufacturing of TEM [20].

TEM has multiple imaging modes that enable examination of specimens from various aspects. Bright-field TEM, in which images are generated directly by transmitted electrons, is the most commonly employed imaging mode seen in the literature. Under this mode, the size, shape, uniformity, and dispersity of nanomaterials can be directly observed. Dark-field TEM allows one to use diffracted electrons from a specific set of crystal planes to image materials and is often used to locate defects in crystals. High-resolution TEM (HRTEM) has been extensively used to study the lattice structure of crystals [21].

3.6.2 Principle

TEM uses a high energy electron beam (100 KeV and 1 MeV) to obtain information from a sample about its morphology, composition, and crystal structure. In TEM, pictures are created by concentrating an electron beam on a very thin specimen (thickness of about 60-100 nm), which transmits information about the materials. In a TEM, a thin sample or fine powder sample is uniformly interacted with a collimated beam of accelerated electrons with high energy over the illuminated area. The electrons are either scattered or pass through the sample unaffected as they move through it. Both elastic and inelastic scattering are possible. By blocking the diffracted electrons that were deflected away from the microscope's optical axis using an aperture, the transmitted electron beam creates contrast on the fluorescent screen. The crystalline structures of nanomaterials interact with the electron beam mostly by diffraction rather than absorption, though the intensity of the transmitted beam is heavily influenced by the density and thickness of the material. The orientation of the crystal's atomic planes with respect to the electron beam affects the strength of the diffraction as well. An image with variable contrast is produced when the transmitted electron beam hits a fluorescent screen or a charge-coupled device (CCD) camera.

3.6.3 Instrumentation

TEM is a type of electron microscope that has three vital parts: (1) an electron gun, which produces the electron beam, and the condenser system, which focuses the beam onto the object, (2) the image-producing system, which comprised of the objective lens, movable specimen stage, and intermediate and projector lenses, which focus the electrons passing through the specimen to form a real, highly magnified image, and (3) the image-recording system, which converts the electrons passing through the specimen to form a fluorescent screen for seeing and focusing the image, as well as a digital camera for permanent records, are typically used in image-recording systems. A vacuum system, including pumps, gauges, and valves, as well as power supply, is also required.

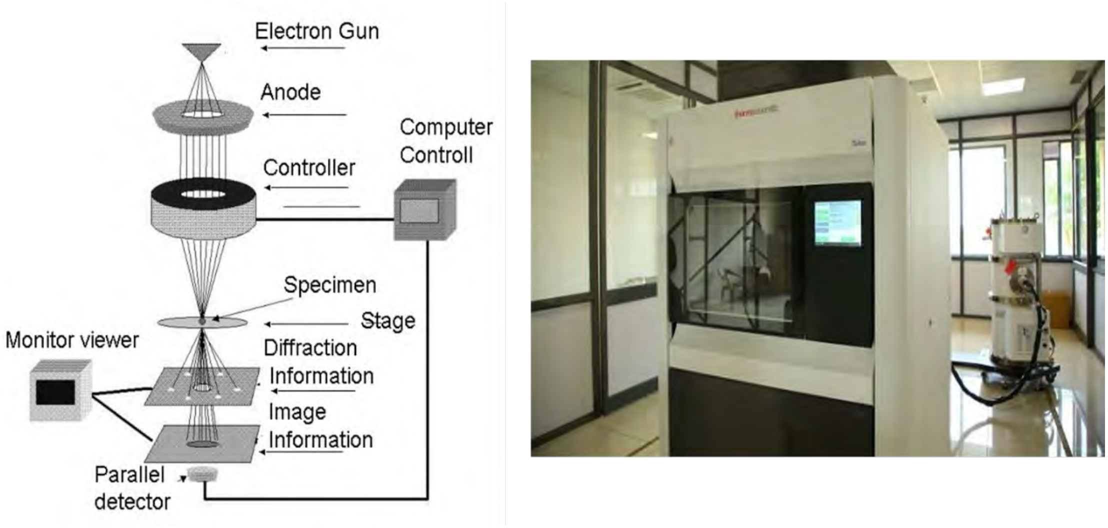

Fig. 3.18 Schematic diagram and Photograph of TEM (Model: Talos F200 S).

The condenser lens concentrates the electron beam from the electron gun into a compact, thin, coherent beam. The condenser aperture limits this beam, excluding high angle electrons. The beam then strikes the specimen, and depending on its thickness and electron transparency, parts of it are transferred. The objective lens focuses this transmitted portion into an image on a phosphor screen or charge coupled device (CCD) camera. The schematic diagram and TEM instrument are shown in figure 3.18. By shutting out high-angle diffracted electrons, optional objective apertures can be employed to improve contrast. The picture is then expanded all the way down the column as it passes through the intermediate and projection lenses.

3.6.4 Experimental

The prepared samples are studied by TEM images and SAED pattern using Talos F200 S TEM instrument. The particle size was calculated using ImageJ software.

3.6.5 Selected area electron diffraction (SAED)

Selected area electron diffraction (SAED), is a crystallographic experimental technique usually performed using a transmission electron microscope (TEM). It is a type of electron diffraction that is employed as one of the most prevalent experimental techniques in material research and solid-state physics. SAED patterns, especially when combined with proper analytical tools, can be utilized to detect crystal orientation, estimate lattice constants, and examine defects.

Due to its relative ease of use and significant informational value, SAED analysis is frequently employed in material research. The device enables a routine diffraction acquisition in a matter of seconds after the sample has been prepared and viewed with a current transmission electron microscope. The images can be used to identify crystal structures, ascertain their orientations, quantify crystal features, look at crystal flaws, or study material textures if they are properly understood. The method of analysis depends on the quantity to be determined as well as whether the diffractogram shows a ring or spot diffraction pattern.

When a large number of crystallites with various orientations are included in the lighted area chosen by the aperture, their diffraction patterns superimpose, forms the illusion of concentric rings. When dealing with polycrystalline samples, powders, or nanoparticles, the ring diffractogram is usual. Each ring's diameter is equal to the sample's plane system’s interplanar distance. This diffractogram offers more statistical data, such as overall crystallinity or texture, than information about specific grains or sample orientation. Despite adequate crystallinity to produce smooth rings, textured materials have a non-uniform intensity distribution over the ring circumference. Ring diffractograms can also be used to distinguish between amorphous and nanocrystalline phases.

3.6.6 Results and discussion

TEM images of GO at different magnitude and SAED pattern are shown in figure 3.19. GO has layers of varying thicknesses reveal a sheet-like morphology with varying transparency. It has a dimension of 1.9 µm x 1.44 µm. The dark areas represent a thick stacking nanostructure made up of many GO with several oxygen functional groups. The enhanced transparency portions correspond to substantially thinner films of a few layers graphene oxide and reduced graphene oxide caused by stacking nanostructure exfoliation. The rGO sample has a significantly high transparency of delaminated graphene layers (of around one to several layer thickness) than the GO sample, demonstrating layer delamination due to reduction.

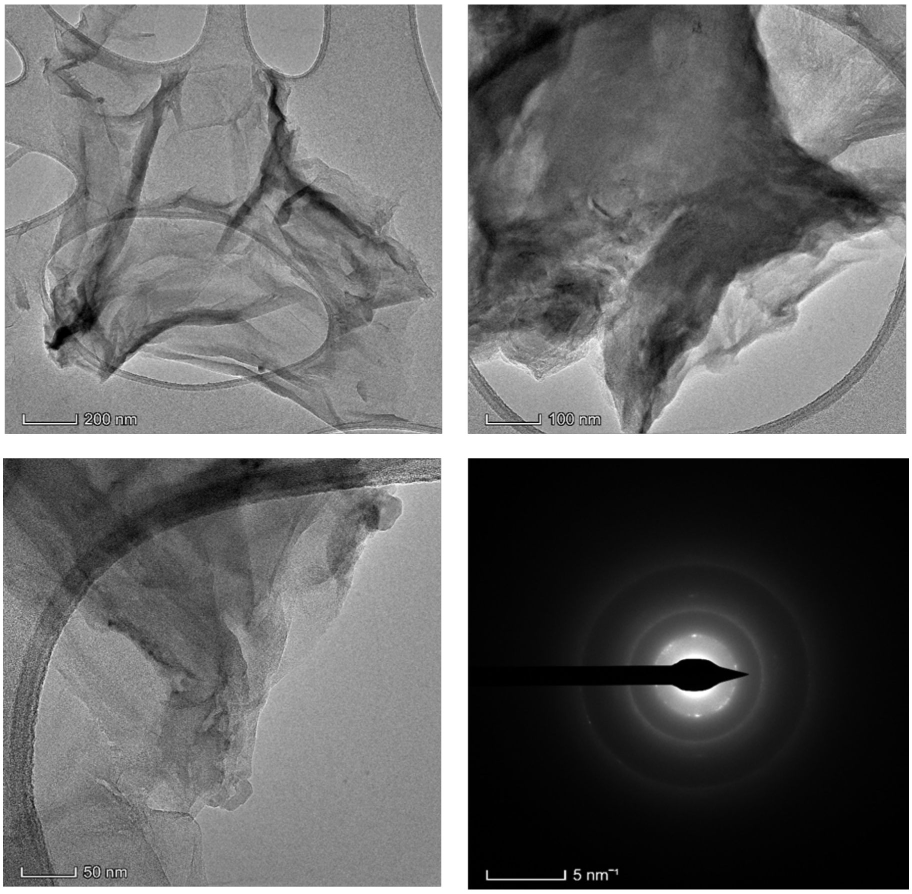

Fig. 3.19 TEM images of GO at different magnification and SAED pattern.

Image 3.20 shows the TEM images of rGO at different magnitudes and SAED pattern. rGO depicts thin sheets like morphology with dimension 1.11 μm x 0.94 μm. After reduction, there was a modification in morphology, with fewer layers and irregular shape morphology. Its appearance has changed after reducing GO with amla extract. Exfoliation of thin multilayer sheets in reduction process and sonification mediums is caused by the rapid removal of intercalated oxygen and other functional groups between the layers.

Selective area electron diffraction (SAED) was used to determine the crystallographic structure of graphene sheets. According to the SAED pattern, the majority of the GO sheets exhibited a set of ring shape patterns with clear diffraction. rGO shows a set of rings with clear and sharp diffraction pattern. We found several spots rather than a single set of ring shape diffraction patterns in rGO, which could be related to the few layers in rGO. This is also shown in the TEM image. Along with this, the diffraction spots in rGO are sharp and clear, which confirms the crystallinity nature. d-spacing is calculated for both GO and rGO samples from SAED pattern. It was found to be 7 Å for GO and 2.3 Å for rGO. The d-spacing values of both GO and rGO calculated from XRD are matched with the values calculated from SAED pattern within the experimental error.

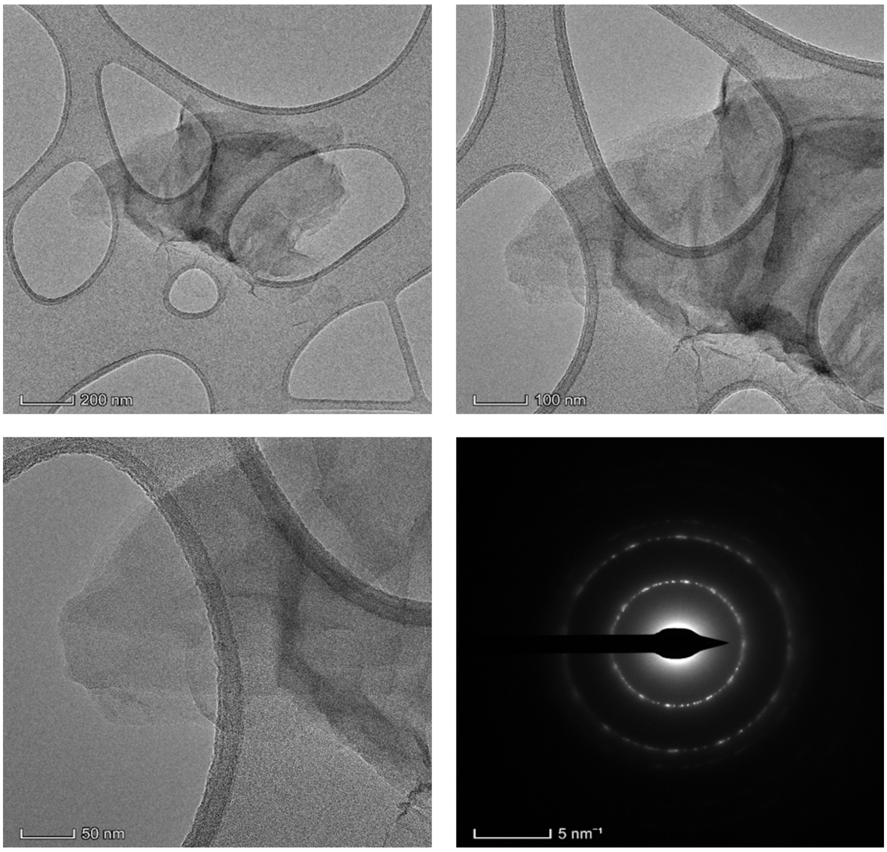

Fig. 3.20 TEM images of rGO at different magnification and SAED pattern.

Figure 3.21 depicts the TEM image and SAED pattern of rGO/NiO composite. It can be clearly seen that the NiO nanoparticles are well decorated on rGO sheets. It reveals that the NiO nanoparticles having uniform diameter decorated on the surface of rGO. The size of the particle is calculated from ImageJ software. Here in the composite, NiO particles having an average size of 67.4 nm.

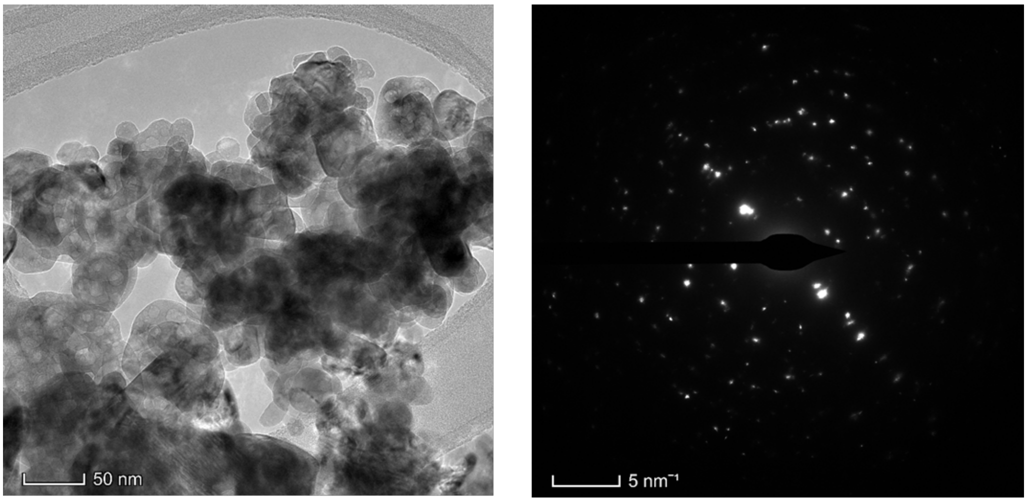

Fig. 3.21 TEM image of rGO/NiO composite and its SAED pattern.

SAED pattern depicts ring shape of diffraction patterns, indicating that the NiO particles are polycrystalline. Calculated d-spacing values are matched with XRD results.

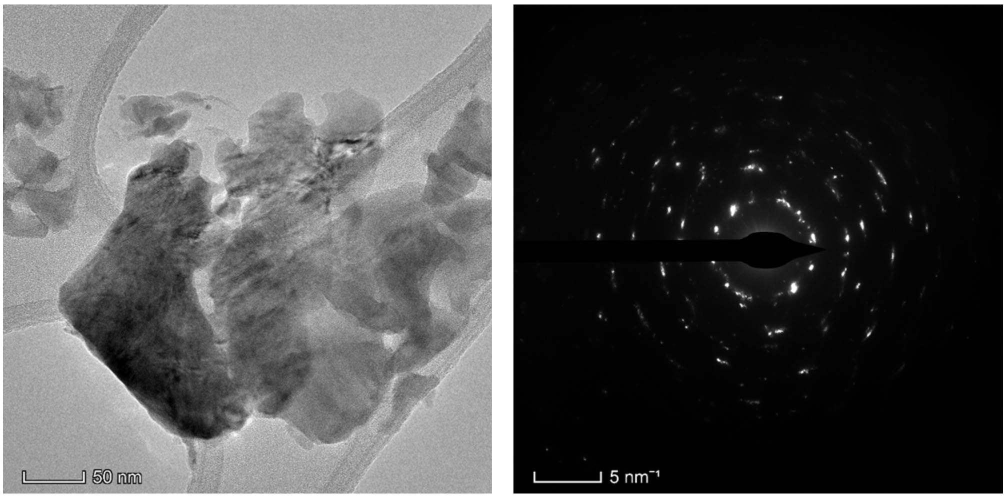

Fig. 3.22 TEM image of rGO/CuO composite and its SAED pattern.

TEM image and SAED pattern of CuO is shown in figure 3.22. From this figure one can clearly say that the CuO nanoparticles are well decorated on the rGO sheets and CuO are irregular in shape having average particle size of about 41.6 nm. SAED pattern reveal that it has ring shape diffraction pattern which indicates that CuO is polycrystallne.

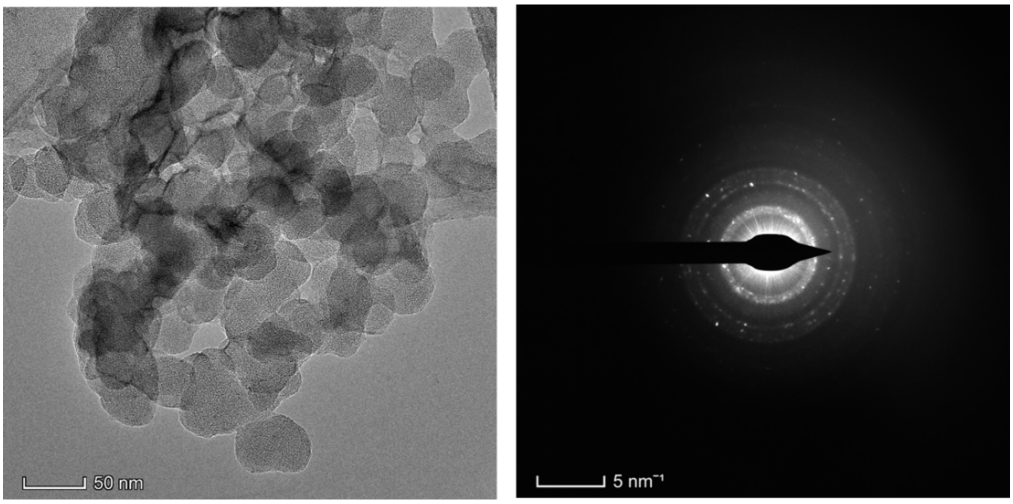

Fig. 3.23 TEM image of rGO/ZnO composite and its SAED pattern.

Figure 3.23 depicts the TEM image and SAED pattern of rGO/ZnO. It can be seen that the ZnO particles are having uniform particle's size and these are well decorated on the surface of rGO sheets. The average size of ZnO nanoparticle is found to be 47.6 nm. SAED pattern shows that the spots form a ring shape of diffraction pattern. It confirms the polycrystalline nature of ZnO nanoparticles.

3.7 Energy dispersive analysis of X-rays

3.7.1 Introduction

Energy-dispersive X-ray analysis (EDAX, EDX or EDS) is a technique used by SEM or TEM to analyse nanoparticles. This is a strong technique for analysing the elemental composition of a desired sample. The nanoparticles are analysed in this procedure by activation with an EDS X-ray spectrophotometer, which is commonly used in modern SEM. Individually separated nanoparticles are placed on a suitable substrate that does not interfere with nanoparticle characterization. It is based on the interaction of an X-ray excitation source and a sample. Its characterization capabilities are largely due to the fundamental premise that each element has a unique atomic structure, which allows a distinct set of peaks on its electromagnetic emission spectrum. The sample can be taken in any form, including solid thin films, solid powder, liquid samples or pellets.

3.7.2 Principle

The fundamental principle of EDAX is the production of X-rays from a specimen using an electron beam. The X-rays are produced based on the properties and type of the elements contained in the sample. As a result, this approach can also be used to determine the energy of emitted X-rays. After maintaining the appropriate instrumental conditions, this method yields accurate findings not only for element identification, but also for element concentration.

The ability of high intensity electromagnetic radiation (X-rays) to eject 'core' electrons (electrons that are not in the outermost shell) from an atom is the main operational principle that permits EDS to function. This is known as Moseley's Law, which established a direct relationship between the frequency of light released and the atomic number of the atom.

Removing these electrons from the system creates a hole that a higher energy electron can fill, releasing energy as it relaxes. Because the energy produced during this relaxing process is unique to each element on the periodic table, blasting a sample with X-rays can be used to determine which elements are present.

3.7.3 Instrumentation

A common EDAX configuration is identical to that of a SEM configuration. EDAX, more particularly, is built within the SEM setup. The operation of EDX, like that of SEM, is dependent on electron focusing. SEM and scanning transmission electron microscopes (STEM) use electron beam excitation, but X-ray fluorescence (XRF) spectrometers use X-ray beam excitation. A detector converts X-rays into voltage signals, which are then measured and passed to a data analyzer for display and study. A Si(Li) detector cooled at cryogenic temperatures by liquid nitrogen is frequently used, and some current systems include silicon drift detectors (SDD) with Peltier cooling devices.

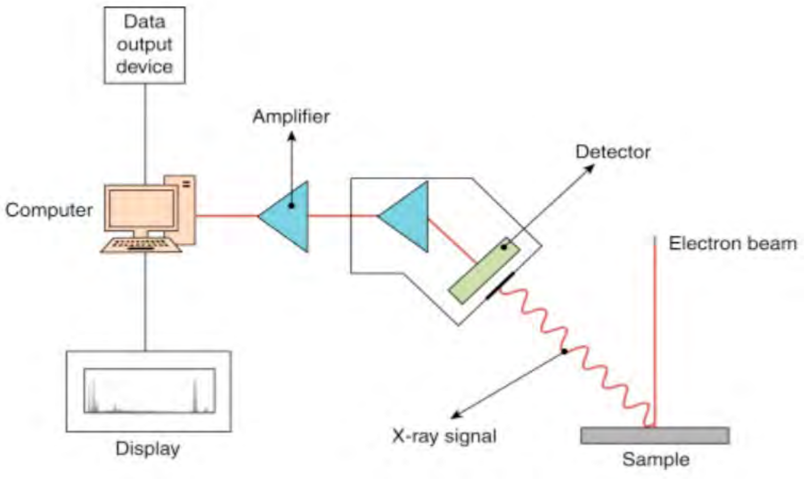

Fig. 3.24 Schematic diagram of EDAX.

The schematic diagram of EDAX is shown in figure 3.24. An extremely powerful beam of charge carriers (electron or proton) or X-rays is used to bombard an object in order to cause it to emit distinctive X-rays. Ground state (unexcited) electrons in distinct energy levels or electron shells are bound to the nucleus in the sample atoms. An incoming beam can excite an electron in an inner shell, removing it from its shell and creating a hole where the electron was before excitation. An electron from a higher-energy shell can occupy this hole.

An X-ray is released when the energies of the higher and lower energy shells differ. The energy-dispersive analysis of X-rays can be used to quantify the energy and number of these X-rays.

In basic EDAX systems, there are three major components. The X-ray detector, a pulse processor to measure voltage in relation to X-ray energy, and a computer system are these components. The X-ray detector is set up to detect X-rays released by the specimen. An X-ray detector detects the emitted X-rays from the sample. When an X-ray enters the detector, it generates a little current, which is then translated into a voltage pulse. The voltage pulse is affected by X-ray energy. Following the measurement of the voltage pulse for a 60-second period, histograms of this data can be shown. This histogram depicts the X-ray energy spectrum, which can be used for elemental analysis.

3.7.4 Experimental

Elemental compositions are studied by using EDAX. X-ray spectra are presented with energy in KeV on the x-axis and the number of counts on the y-axis.

3.7.5 Results and discussion

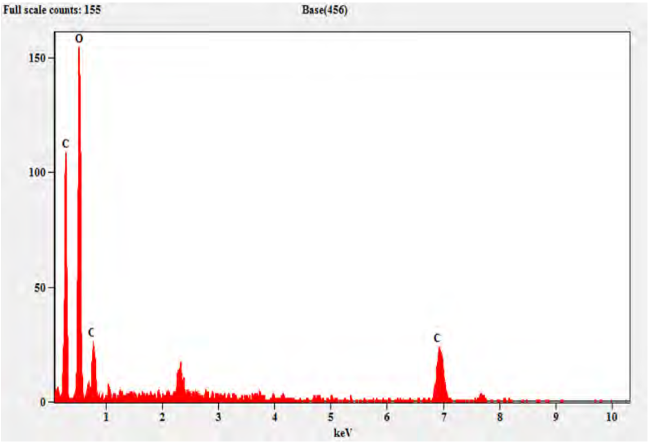

Fig. 3.25 EDAX image of GO

Figure 3.25 depicts the EDAX result of GO and figure 3.26 depicts the result of rGO/NiO, rGO/CuO, rGO/ZnO and rGO/Co_3O_4 composite materials. It clearly shows that there are no extra elements present in the samples. Absence of unwanted peaks confirms the purity of sample.

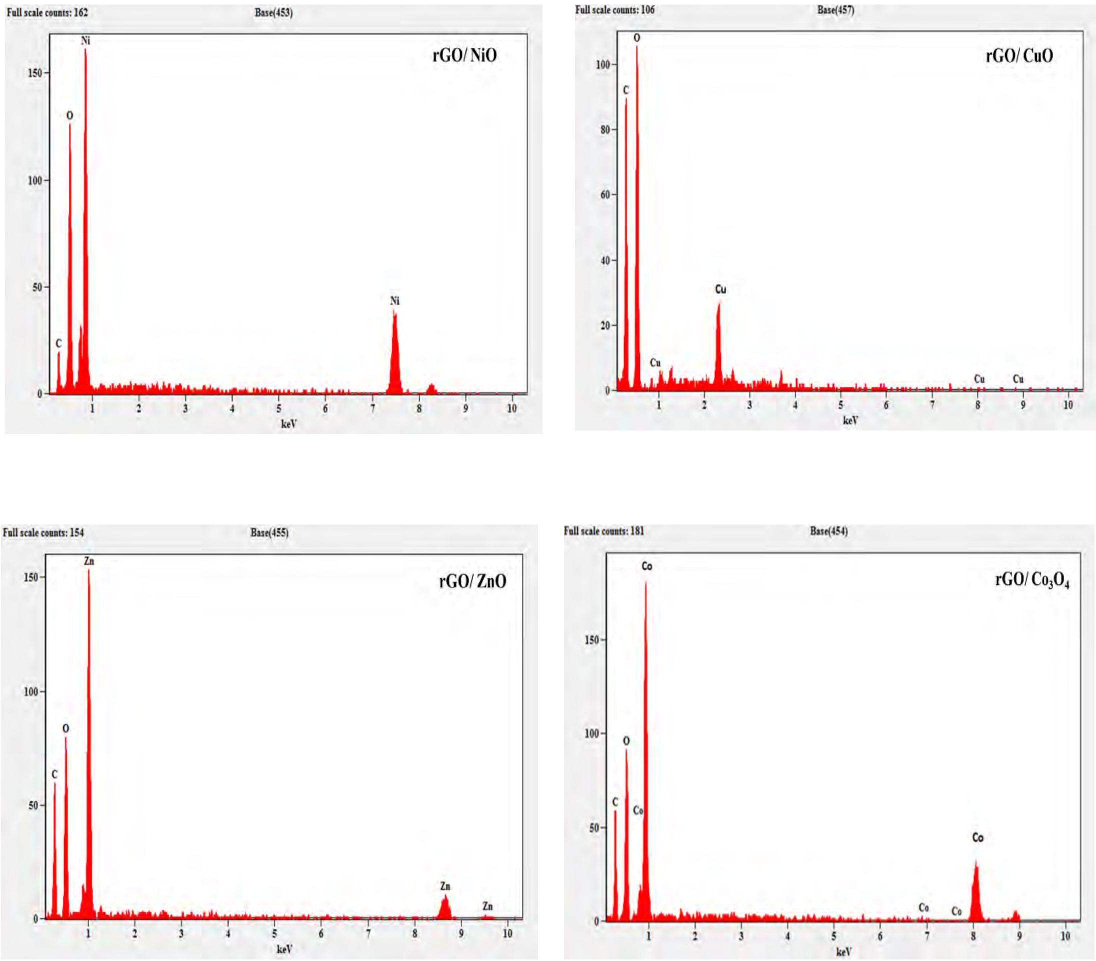

Fig. 3.26 EDX images of rGO/NiO, rGO/CuO, rGO/ZnO and rGO/Co_3O_4.

Table 3.1 shows the elemental composition of GO, rGO/NiO, rGO/CuO, rGO/ZnO and rGO/Co_3O_4 composites. It contains all information including elemental family, percentage of atomic fraction and also percentage of mass fraction.

Table 3.1 Composition analysis of GO and other composite materials.

	Element	Family	Atomic fraction %	Mass fraction %
1. GO	C	K	92.7	90.3
	O	K	7.3	9.7
2. rGO/NiO	C	K	50.2	26.8
	O	K	27.9	20.3
	Ni	K	21.9	52.9
3. rGO/CuO	C	K	61.4	32.6
	O	K	16.0	11.5
	Cu	K	22.6	55.9
4. rGO/ZnO	C	K	90.30	81.8
	O	K	7.74	9.55
	Zn	K	1.96	8.65
5. rGO/Co_3O_4	C	K	39.49	60.44
	O	K	25.64	29.46
	Co	K	34.87	10.1

Limitations of EDAX

Although EDS is a very effective approach, there are a number of issues with the process that limit its utility. To begin with, EDS is not a particularly sensitive method. If an element's concentration in the sample is too low, the quantity of energy emitted by X-rays after striking the sample will be inadequate to accurately estimate its proportion. Second, EDS does not operate for elements with low atomic numbers in general. Both hydrogen and helium have a n=1 shell, which means there are no core electrons to be removed, allowing for X-ray emission. Meanwhile, lithium and beryllium have sufficiently low atomic numbers that the energy of X-rays emitted by Li or Be samples is insufficient for measurement and sometime they cannot be measured.

The thickness of the sample adds another layer of difficulty to the method. Sample thickness can bring energy levels closer together, making electrons more easily moved to outer energy levels, causing divergence in the results. Overlapping emitted x-rays are another form of inaccuracy that might affect KeV values. Furthermore, X-rays are not particularly effective at penetrating above several nanometers in samples, therefore the approach can only efficiently assess surface layers. As a result, if there is a difference between the exterior and interior material layers, it will not always be seen in EDS.

3.8 Summary

In this chapter we have discussed several characterization techniques used to study the prepared samples. XRD data confirms the synthesized materials by their characteristic peaks and diffraction plane. Crystallite size is calculated using Debye-

Scherrer equation. Calculated d-spacing values reveal the reduction of GO by amla extract. The functional groups are identified by FTIR analysis. Raman spectra confirms the existence of G band D band for GO and rGO samples. A slight shift in the G band indicates the reduction of GO and other metal oxides are also confirmed by existence of peaks in the lower wave number region. The morphology is studied by SEM and TEM images. TEM images reveal that the particles are in the nm range and EDAX confirms that there are no additional peaks present in the image which implies the prepared samples are pure.

From all these characterizations, we can conclude that amla is an efficient reducing agent and it avoids the use of hazardous chemicals for the reduction process. Also, the results indicate that ultrasonication method of synthesis of composite is proved to be an efficient method and it produces homogeneous nanoparticles with particle size ranges in the nm scale.

References

[1] B.S. Murthy, P. Shankar, Baldev Raj, B.B Rath, James Murday, *Textbook of Nanoscience and Nanotechnology*, 2013, (Universities Press Private Limited+Spinger, India).

[2] Rajendra Kumar Goyal, *Nanomaterials and Nanocomposites*, 2018, (Taylor & Francis, Newyork).

[3] Myeongkyu Lee, *X-ray Dffraction for Materals Research*, 2016, (CRC Press+Apple Academic Press, Florida, Canada).

[4] C.S. Naveen, M.L. Dinesha, H.S. Jayanna, *J. Mater. Sc. Technol*. **29** (2013) 898.

[5] Brian C. Smith, *Fundamentals of Fourier Transform Infrared Spectroscopy*, 2011, (Taylor and Francis group, London, Newyork).

[6] Yong Jiang, Dandan Chen, Jinsong Song, Zheng Jiao, Qiliang Ma, Haijiao Zhang, Lingli Cheng, Bing Zhao, Yuliang Chu, *Electrochim. Acta*, **91** (2013) 173.

[7] Afshin Pendashteha, Mir Fazlollah Mousavia, Mohammad Safi Rahmanifar, *Electrochim. Acta*, **88** (2013) 347.

[8] Kyeong-Won Park, Jong Hwa Jung, *J. Power Sources*, **199** (2012) 379.

[9] Shuo Huang, Yuhong Jin, Mengqiu Jia, *Electrochim. Acta*, **95** (2013) 139.

[10] Jun Zhang, A thesis on ‘Analysis and characterization of consumer products by FTIR, Raman, Chemometrics, and two dimensional ATR-FTIR correlation spectroscopy’. The State University of New Jersey, New Jersey (2009).

[11] Gurvinder Singh Bumbrah, Rakesh Mohan Sharma, *Egypt. J. Forensic Sci*. **6** (2016) 209.

[12] P. Pushkar, Kalantri, R. Rakesh, Somani, T. Dinesh, Makhija, *Der Chemica Sinica*, **1** (2010) 1.

[13] H. Pang, Z. Yan, W. Wang, J. Chen, J. Zhang, H. Zheng, *Nanoscale*, **4** (2012) 5946.

[14] Krishnamoorthy K, Veerapandian M , Zhang LH, Yun K, Kim SJ, *J phys C*, **116** (2012) 17280.

[15] Venugopal G, Krishnamoorthy K, Mohan R, Kim SJ, *Mater. Chem Phys* **132** (2012) 29.

[16] D. Gao, G. Yang, J. Li, J. Zhang, J. Zhang, D. Xue, *J. Phys. Chem. C,* **114** (2010) 18347.

[17] M.A. Dar, S.H. Nam, Y.S. Kim, W.B. Kim, Synthesis, *J Solid State Electrochem*, **14** (2010) 1719.

[18] Yan-Li Chen, Zhong-Ai Hu, Yan-Qin Chang, Huan-Wen Wang, Zi-Yu Zhang, Yu-Ying Yang, and Hong-Ying Wu, *J. Phys. Chem. C,* **115** (2011) 2563.

[19] T.V. Khai, D.S. Kwak, Y.J. Kwon, H.Y. Cho, T.N. Huan, H. Chung, H. Ham, C. Lee, N.V. Dan, N.T. Tung, *Chem. Eng*. **232** (2013) 346.

[20] Ray F. Egerton, Physical principles of electron microscopy, 2005, (Springer, Newyork).

[21] Challa S.S.R. Kumar, Transmission Electron Microscopy Characterization of nanomaterials, 2014, (Springer, Newyork).

4.1 Introduction

Electrochemistry is a significant tool for investigating electron transport reactions. The movement of electrons is linked to chemical changes in electrochemistry. Electrochemistry is the study of electron transfer at the solution/electrode interface. Cyclic voltammetry is one of the techniques used in electrochemistry. It has long been noted for its diverse applications in a variety of fields that involve electron transfer processes, both directly and indirectly. It has been widely used in monitoring the electrochemical behaviour of a wide range of compounds because it can provide insights into the link between structure, potential, and characteristic activities. The technology is noteworthy for its benefits such as simplicity, sensitivity, speed, and low prices, among others, which has resulted in a wide range of applications.

An electrochemical reaction occurs when a chemical reaction is caused by an externally supplied current, as in electrolysis, or when an electric current is produced by a spontaneous chemical reaction, as in a battery. Oxidation-reduction or (redox) reactions are chemical reactions in which electrons are exchanged directly between molecules and/or atoms. Electrochemistry, in general, defines the overall processes that occur when individual redox reactions are independent yet linked by an external electric circuit and an intervening electrolyte.

Luigi Galvani, an Italian physician and anatomist, established electrochemistry in the late 18th century. On his essay, he builds a connection between chemical reactions and electricity "In Motu Musculari, De Viribus Electricitatis Commentarius" in 1791 where he mentioned a "nerveo-electrical substance" on biological life forms [1].

The term "redox" refers to the reduction-oxidation process. It describes the electrochemical processes that include the transfer of electrons to or from a molecule or ion that is altering its oxidation state. The removal of electrons from an atom or molecule is referred to as oxidation, whereas the gain of electrons is referred to as reduction. This reaction can be initiated by an external voltage or by the release of chemical energy. The terms oxidation and reduction refer to the changes in oxidation states that occur in the atoms, ions, or molecules involved in an electrochemical reaction. The oxidation state of an atom or ion that gives up an electron to another atom or ion increases, while the oxidation state of the recipient of the negatively charged electron decreases.

The atom or molecule that releases electrons is known as the reducing agent, or reductant, while the substance that takes electrons is known as the oxidant. In the other context, oxidation and reduction reactions can also be defined as: the gain of oxygen is called the oxidation of the atom or molecule to which the oxygen is added. The loss oxygen or gain of hydrogen means a reduction.

Here in this study, the electrochemical measurements were done by using cyclic voltammetry, Electrochemical impedance spectroscopy and Galvanostatic charge/discharge curves. These are the three significant techniques used for supercapacitor study.

4.2 Three electrode system

An electrochemical cell is a device that generates an electric current by releasing energy through a spontaneous redox reaction, which can be produced by electricity. The three-electrode system is comprised of a counter electrode, a reference electrode and a working electrode. The job of the reference electrode is to serve as a reference in measuring and adjusting the working electrode potential while no current is passed through it. At low current density, the reference electrode should have a constant electrochemical potential. The reference potential is substantially more stable with the three-electrode arrangement, and there is compensation for voltage drop across the solution. This results in greater control over the working electrode potential. The Saturated Calomel Electrode and the Ag/AgCl electrode are the most commonly used lab reference electrodes. Figure 4.1 depicts the electrochemical cell used for the cyclic voltametric study.

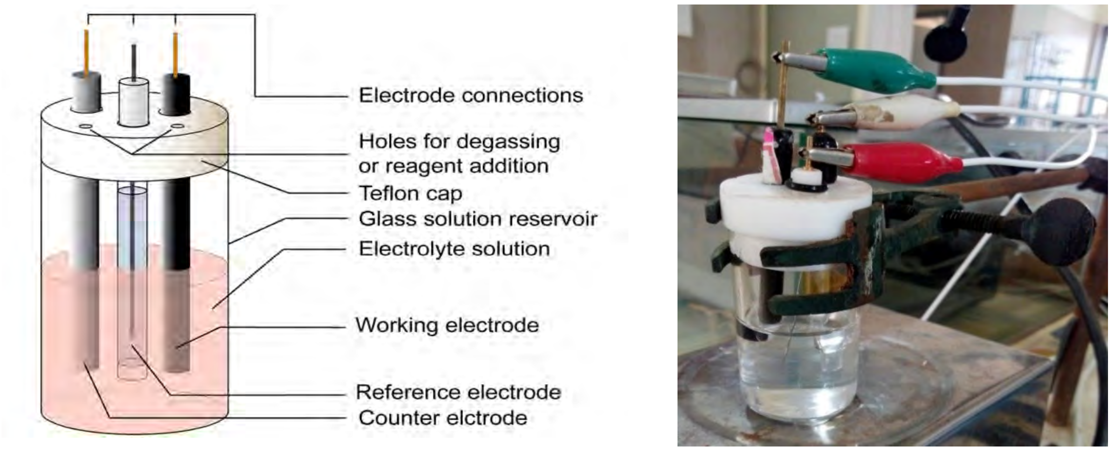

Fig. 4.1 Schematic representation (ref. 2) and photograph of electrochemical cell.

One of the three electrodes is the test or working electrode. This is the electrode where the electrochemical processes (reduction or oxidation) being studied occur. The reference electrode is the second functioning electrode. This is the electrode whose potential is stable enough to serve as a standard against which the potentials of the other electrodes in the cell can be measured. The final functioning electrode is the counter or auxiliary electrode, which functions as an electron source or sink to let current to flow from the external circuit through the cell.

4.2.1 Preparation of electrodes

Glassy carbon electrode is used as a working electrode and here it occurs electrochemical reactions. Once activated by polishing, the surface of glassy carbon electrodes is extremely reactive. When impurities are present in the solvent, they preferentially adsorb to the carbon surface of the electrode, causing the voltammograms to change.

Prior to taking measurements, the electrode must be polished. Because some analytes are sensitive to electrode surface adsorption, electrodes must frequently be repolished between measurements during the course of an experiment. Figure eight motions on a cloth polishing pad in a water-alumina slurry are a simple approach to polish an electrode. After completion of polishing the glassy carbon electrode, the sample is coated on it using micro pipette and kept it for drying.

4.2.2 Cyclic voltammetry

Cyclic voltammetry (CV) is a technique used to analyze reaction mechanism involving electron transfer. The approach entails varying an electrode potential between two limits at a constant rate while monitoring the current that develops in an electrochemical cell. In cyclic voltammetry, a voltage is applied to an electrode submerged in an electrolyte solution, and the system is then monitored for response.

Cyclic voltammetry measures a supercapacitor's charge-response to a changing voltage and is thus a method of determining capacitance. The process for obtaining a voltammogram is straightforward and does not require any specialized equipment.

Cyclic voltametric studies were conducted using CHI6155E which is shown in figure 4.2 with three electrode system. We have used Ag/AgCl as reference electrode, platinum as counter electrode and glassy carbon electrode as a working electrode.

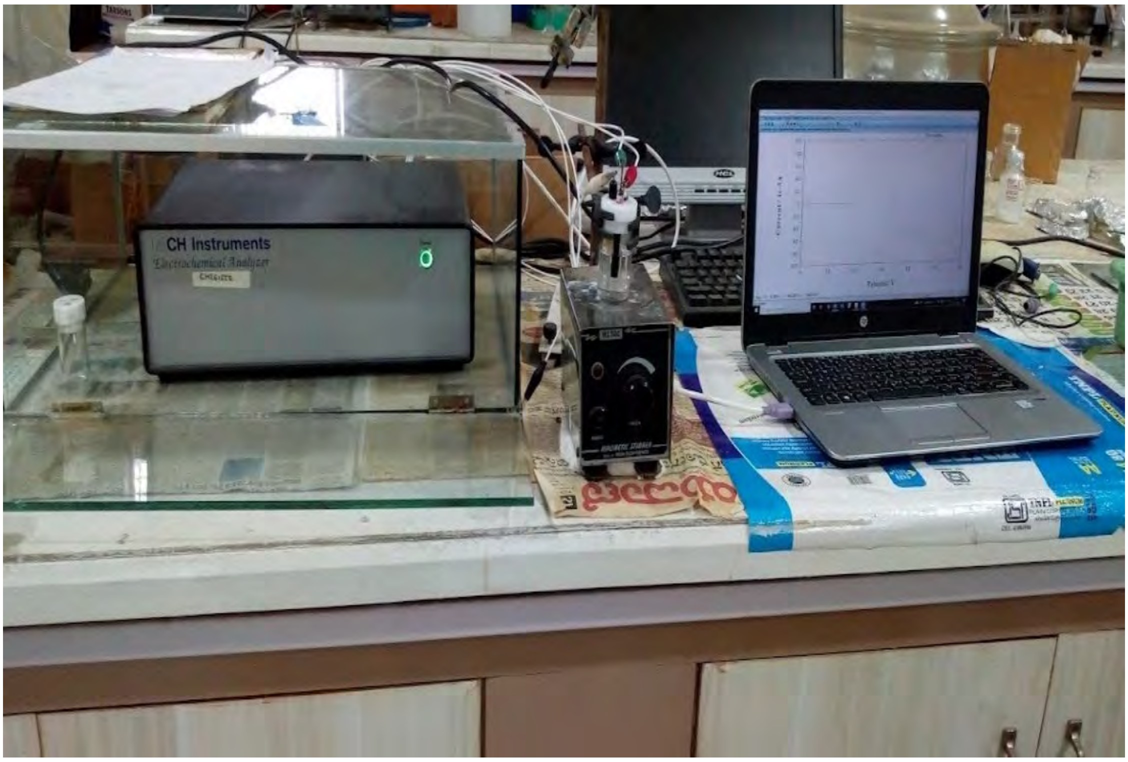

Fig. 4.2 Photograph of CH instrument.

CV is a potentio dynamic electrochemical technique that is commonly used to investigate the electrochemical properties of an analyte in solution, specifically to measure the current that develops in an electrochemical cell over a voltage range. CV keeps changing the potential as a linear function of time, and the corresponding current response is recorded. A cyclic voltammogram is the resultant of current versus potential graph. The current at the working electrode is used in this study. The potential of the working electrode is raised linearly with time. The ramping is referred to as scan rate and is measured in Vs^{-1}. The reference electrode's potential is kept constant.

The forward scan generates a current peak for any analyte that, depending on the starting scan direction through the potential range examined, can be reduced or oxidized. The current increases as the voltage approaches the reduction potential of the analyte, but subsequently decreases as the concentration of the analyte gets closer the electrode surface. If the redox pair is reversible, the applied potential will approach the potential that will re-oxidize the product generated in the first reduction reaction, producing a reverse polarity current from the forward scan. This oxidation peak will typically resemble the reduction peak in form.

The electrolytes were used by taking 1M NaOH, 2M NaOH, 1M KOH and 2M KOH solutions. The prepared samples were coated on the glassy carbon electrode by using micro pipette without using any binder. This binder free electrode will enhance the electrochemical performance of the material [3].

The specific capacitance of the material from CV curve can be calculated using the relation 4.1.

$$C_s = \frac{1}{m\, s\, \Delta V} \int_{Vi}^{Vf} I(V)dV \quad \ldots\ldots\ldots\ldots\ldots.. \ (4.1)$$

Where m is the mass of active material, s is the scan rate, $\Delta V = V_f - V_i$ is the potential window and I(V) is the instantaneous current. Integral part is the area of the curve in voltammogram.

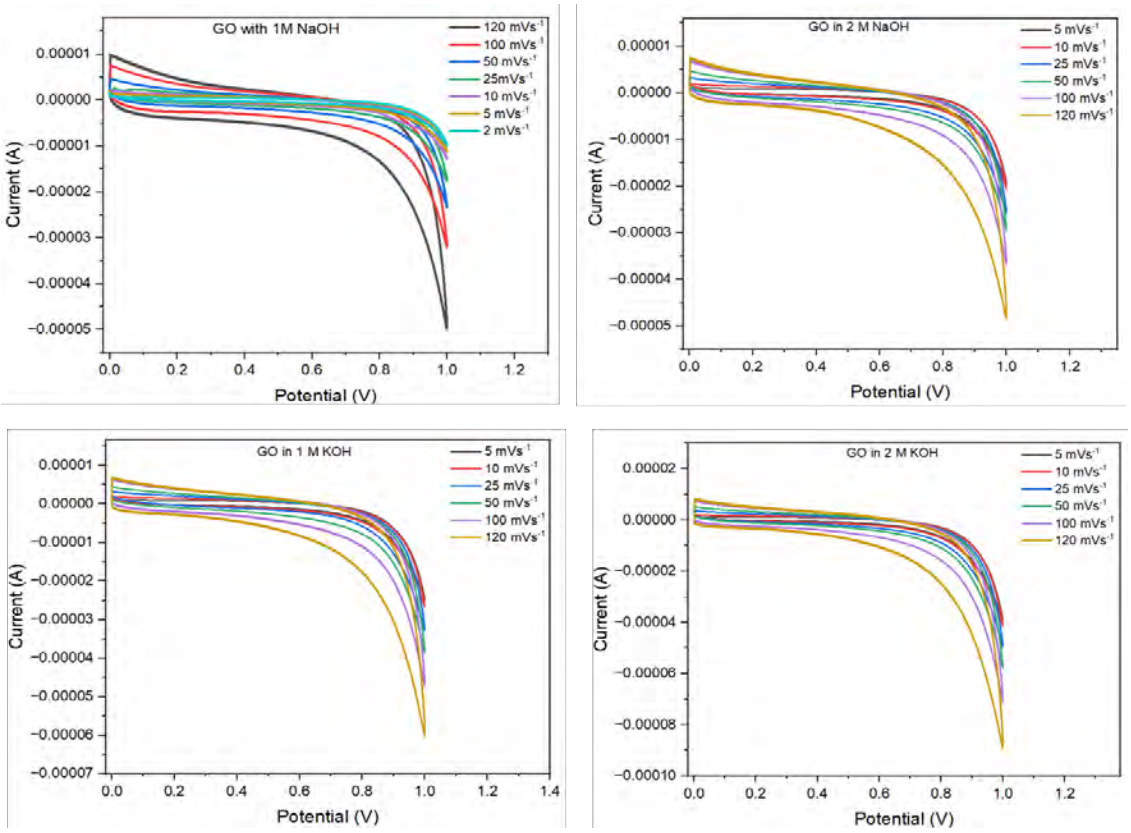

Fig. 4.3 CV curves of GO at different scan rates in 1M NaOH, 2M NaOH, 1M KOH and 2M KOH (aqueous) electrolytes.

Figure 4.3 depicts the CV curves of the GO sample at scan rates 5 mVs^{-1}, 10 mVs^{-1}, 25 mVs^{-1}, 50 mVs^{-1}, 100 mVs^{-1}, 120 mVs^{-1} in 1M NaOH, 2M NaOH, 1M KOH and 2M KOH electrolytes. It can be clearly seen the CV curves are approximately rectangular shape and there are no redox peaks in any of the electrolyte indicating capacitive type of behaviour. Specific capacitance at different scan rates is calculated using expression 4.1 and it shows higher value of specific capacitance value for 2M KOH electrolyte. K^+ ions have higher ionic mobility (7.6 x 10^{-5} cm^2 s^{-1} v^{-1}) and molar conductivity (73.5 cm^2 Ω^{-1} mol^{-1}) than Na^+ ions (5.2 x 10^{-5} cm^2 s^{-1} v^{-1} and 50.1 cm^2 Ω^{-1} mol^{-1}) in aqueous medium [4]. Due to this reason GO shows good specific capacitance value for 2M KOH.

The specific capacitance values at different scan rates and different electrolyte are tabulated in the table 4.1. The specific capacitance value decreases with increase in scan rate and highest value of specific capacitance is observed for 2M KOH solution.

Table 4.1 Specific capacitance values of GO at different scan rates and electrolytes

GO	**Specific capacitance (Fg^{-1})**			
Scan rate (mVs^{-1})	1M NaOH	2M NaOH	1M KOH	2M KOH
120	4.61	5.04	5.94	8.4
100	5.95	5.82	6.76	9.42
50	6.09	7.44	8.95	12.5
25	8.71	12.5	14.3	20.9
10	16.4	23.5	28.7	42
5	27	40.9	50.9	76.1
2	52.8			

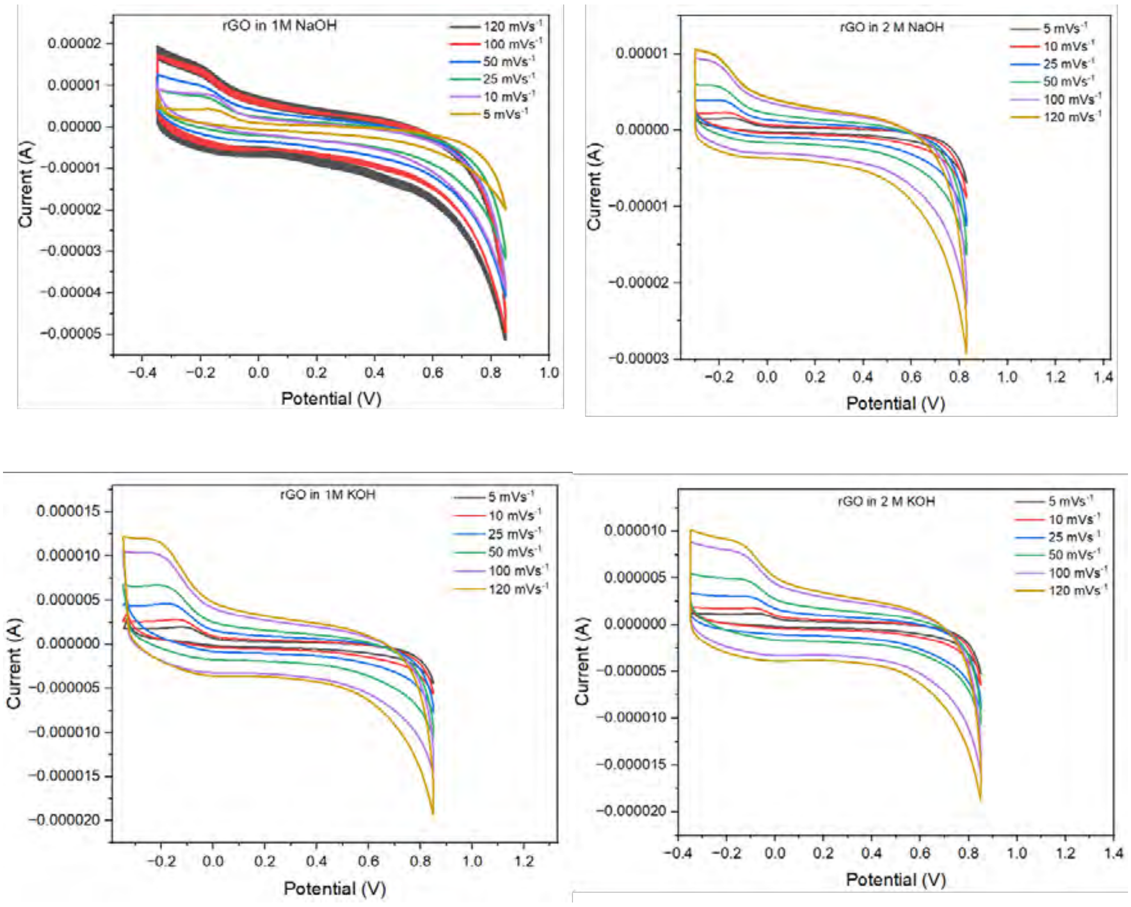

Fig. 4.4 CV curves of rGO at different scan rates in 1M NaOH, 2M NaOH, 1M KOH and 2M KOH (aqueous) electrolytes.

Figure 4.4 depicts the CV curve of rGO at different scan rates and used 1M NaOH, 2M NaOH, 1M KOH and 2M KOH electrolyte solutions. The CV curves are approximately rectangular for 1M and 2M NaOH solutions. For 1M and 2M KOH solutions, the curve is rectangular between the potential 0 to 0.85 V which indicates the capacitive type of nature. A small redox hump can be seen in lower potential values. A slight deviation of the CV curves at specifically lower potential regions are associated to fast Faradaic reactions, which may be attributed to the existence of extra oxygen-containing functional groups, particularly epoxy and alkoxy, at the carbon's surface [5-7].

The specific capacitance values are calculated for all 4 electrolytes at different scan rates. It shows highest value of specific capacitance in 1M NaOH electrolyte solution compared to other three. Ionic radius also plays an important role here. Ionic radius of K^+ ion is 280 pm and that of Na^+ is 227 pm. The match between the electrolyte ion size and the pore size of carbon electrode material has a significant impact on the possible specific capacitance [8].

Table 4.2 Specific capacitance values of rGO at different scan rates and electrolytes

rGO	**Specific capacitance (Fg^{-1})**			
Scan rate (mVs^{-1})	1M NaOH	2M NaOH	1M KOH	2M KOH
120	10.3	6.23	5	5.75
100	11.1	6.26	5.15	6
50	17.5	8.67	8.58	7.96
25	25.7	13.2	12.9	12.6
10	75.6	24.9	24.2	22.5
5	77.9	41.6	40.4	38.2

Figure 4.5 shows the CV curves of bare NiO in all the four electrolytes and measured at different scan rates. The curves are not in rectangular shape which indicates that it undergoes reverse redox reaction. As the scan rates increase, the oxidation and reduction peaks shift more in favor of the positive and negative axis, which is a result of the Faradic redox reaction's rapid ionic/electronic diffusion [9-11].

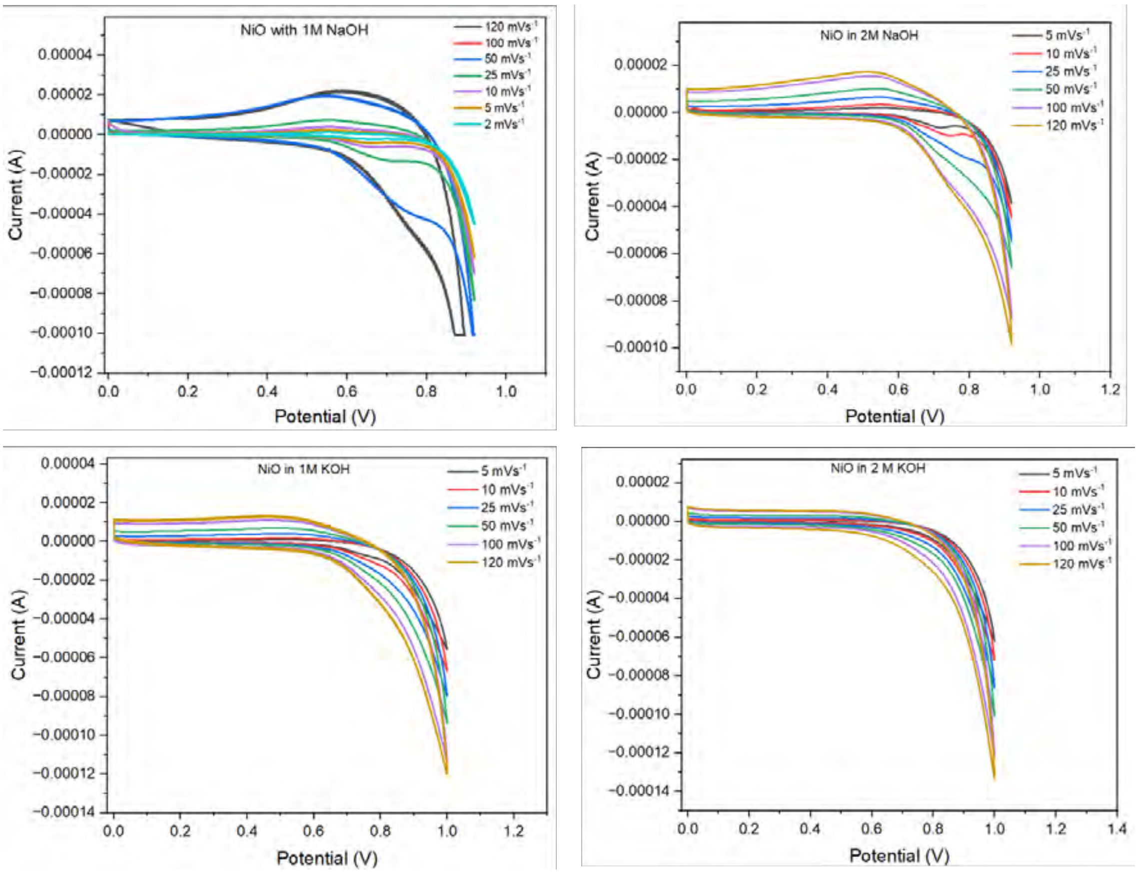

Fig. 4.5 CV curves of NiO at different scan rates in 1M NaOH, 2M NaOH, 1M KOH and 2M KOH (aqueous) electrolytes.

The charge storage process occurs due to the redox reaction

$$NiO + OH^- \leftrightarrow NiOOH + e^- \text{ .... (4.2)}$$

The specific capacitance is calculated and the values are tabulated in the table 4.3. From this it is seen that the specific capacitance value is high for KOH electrolyte than NaOH.

As the concentration of electrolyte increases, the specific capacitance value also increases because of the ionic concentration.

Table 4.3 Specific capacitance values of NiO at different scan rates and electrolytes

NiO	**Specific capacitance (Fg^{-1})**			
Scan rate (mVs^{-1})	1M NaOH	2M NaOH	1M KOH	2M KOH
120	13.2	18	13.4	12
100	14.8	12.8	14.5	12.7
50	28.2	17.4	21.8	20
25	29.6	24.5	34.2	33
10	48.6	41.3	65.8	66.6
5	77.2	63.8	107	115
2	135			

Figure 4.6 shows the cyclic voltammogram of CuO at various scan rates with the potential window 0 to 1 V for all four electrolytes. From this figure we can clearly say that it is a pseudocapacitive type nature. The specific capacitance values are measured and tabulated in the table 4.4. It reveals that KOH shows a good electrochemical reaction. And the material shows high value of specific capacitance in 2M KOH electrolytes compared to other three due to higher ionic concentration. The summarized redox reaction for CuO is given as [12]

$$2CuO + H_2O + 2e^{-1} \leftrightarrow Cu_2 + 2OH^{-} \ldots\ldots\ldots\ldots (4.3)$$

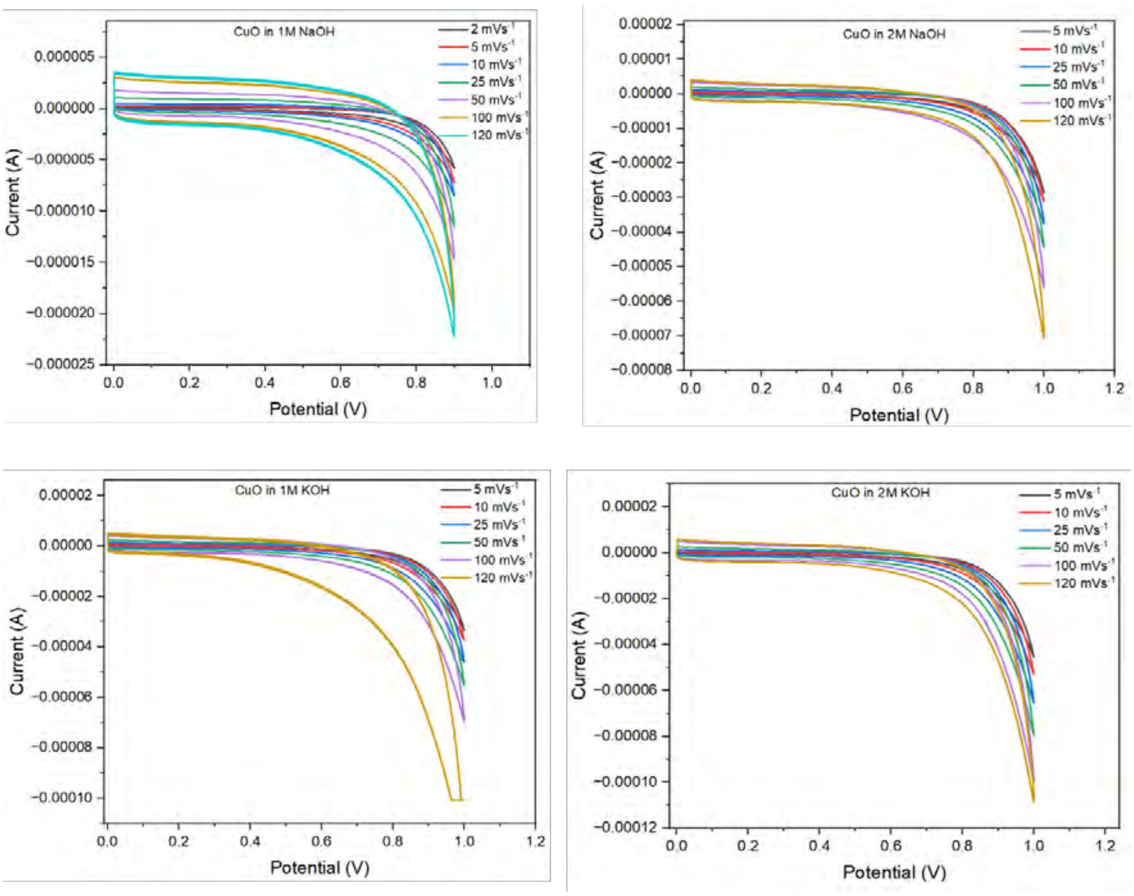

Fig. 4.6 CV curves of CuO at different scan rates in different electrolytes.

Table 4.4 Specific capacitance values of CuO at different scan rates and electrolytes

CuO	**Specific capacitance (Fg^{-1})**			
Scan rate (mVs^{-1})	1M NaOH	2M NaOH	1M KOH	2M KOH
120	3.15	6.62	8.59	10.7
100	3.31	7.09	13.9	11.2
50	4.36	10.2	14.9	17.3
25	6.04	16.4	20.3	27.3
10	9.91	32.6	39.4	54.2
5	16	58.8	68	91.4
2	30.5			

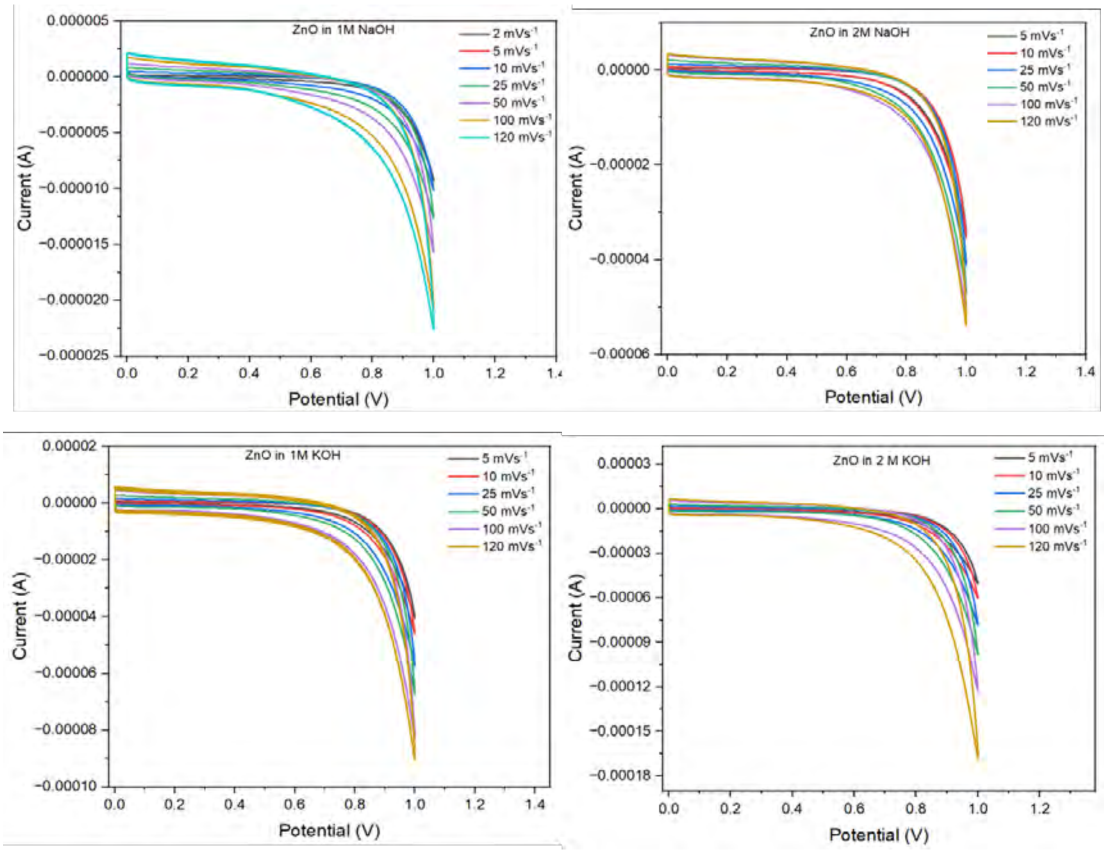

Fig. 4.7 CV curves of ZnO at different scan rates in 1M NaOH, 2M NaOH, 1M KOH and 2M KOH (aqueous) electrolytes.

Table 4.5 Specific capacitance values of ZnO at different scan rates and electrolytes

ZnO	**Specific capacitance (Fg^{-1})**			
Scan rate (mVs^{-1})	1M NaOH	2M NaOH	1M KOH	2M KOH
120	2.53	4.96	9.04	14.3
100	2.7	5.94	9.85	15.7
50	3.9	10.1	14.5	20.2
25	6.04	16.9	24.1	31.2
10	11.5	34.2	46.7	61
5	22.9	65.8	81	103
2	47			

Figure 4.7 shows the CV curves of ZnO nanoparticles in various electrolytes. These curves reveal that it is a pseudocapacitive behaviour. The specific capacitance values were calculated for all four electrolytes and tabulated in the below table 4.5. Here also the electrochemical reaction was good for 2M KOH compared to other three.

Figure 4.8 shows the cyclic voltammogram of Co_3O_4 sample with the potential window 0 to 0.8 V. Here we can clearly observe redox peaks in each graph indicates that it is a pseudocapacitive type material. The distance between anodic and cathodic peak is more for NaOH electrolyte. The reactions involved in redox reaction are

$$Co_3O_4 + OH^- + H_2O \leftrightarrow 3\ CoOOH + e^- \quad \ldots\ldots\ldots\ldots\ldots\ (4.4)$$

$$CoOOH + OH^- \leftrightarrow CoO_2 + H_2O + e^- \quad \ldots\ldots\ldots\ldots\ldots\ldots\ (4.5)$$

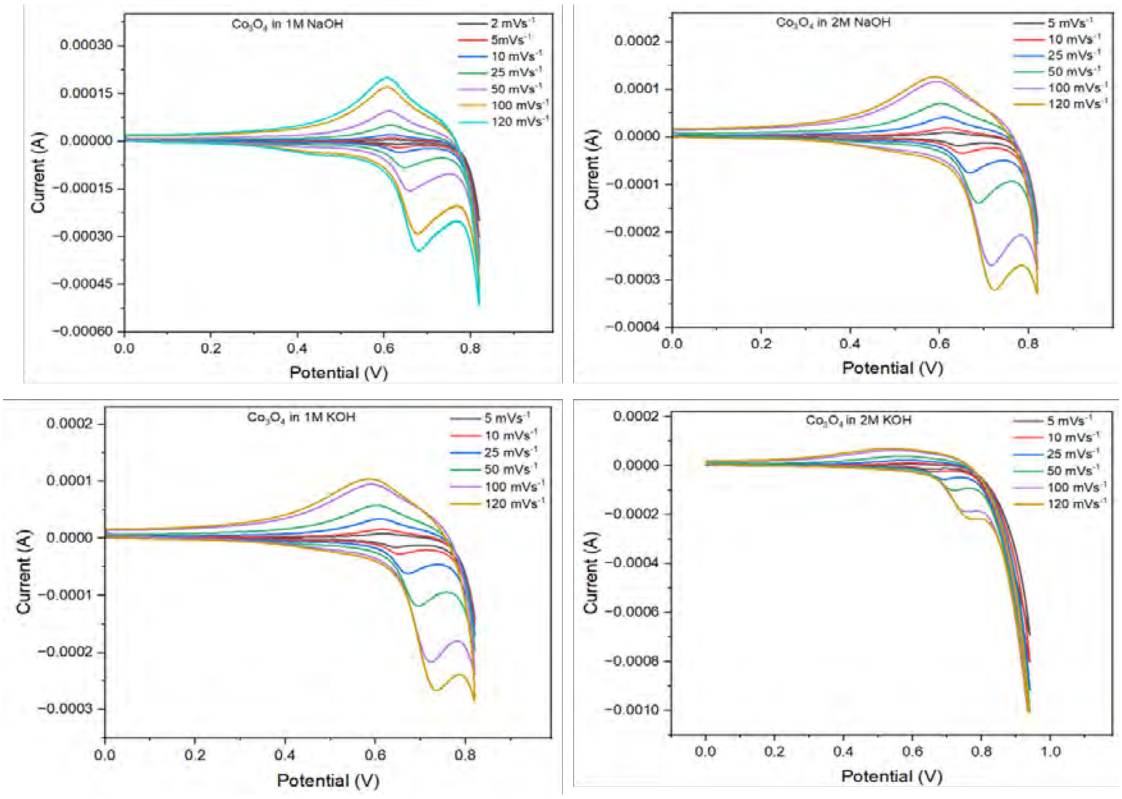

Fig. 4.8 CV curves of Co_3O_4 at different scan rates in 1M NaOH, 2M NaOH, 1M KOH and 2M KOH (aqueous) electrolytes.

As the scan rate increases the area of the curve also increases. The specific capacitance decreases with increase in scan rate.

Table 4.6 Specific capacitance values of Co_3O_4 at different scan rates and electrolytes

Co_3O_4	**Specific capacitance (Fg^{-1})**			
Scan rate (mVs^{-1})	1M NaOH	2M NaOH	1M KOH	2M KOH
120	39.3	29.8	24.6	21.2
100	39.4	31.1	25.4	22.5
50	41.6	32.7	29.1	26.9
25	44.4	36.9	30.7	37.8
10	46.3	44.2	35.5	65
5	54	47.1	41.8	74
2	71.7			

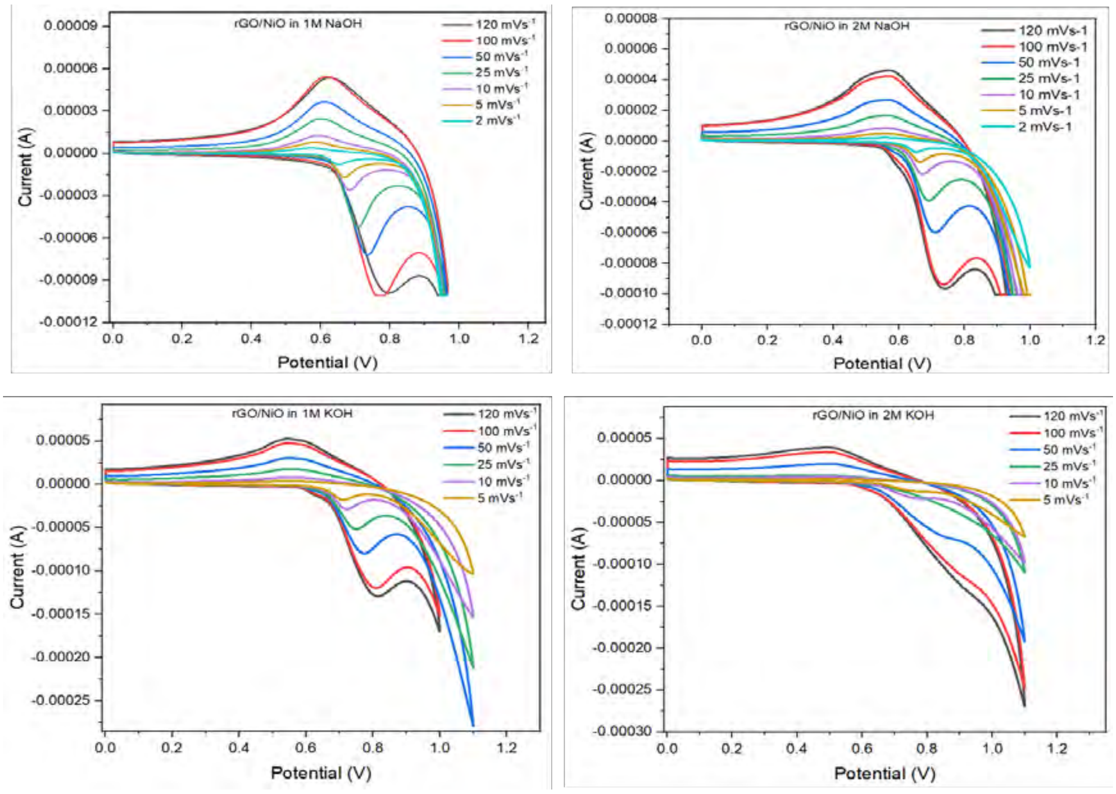

Fig. 4.9 CV curves of rGO/NiO at different scan rates in 1M NaOH, 2M NaOH, 1M KOH and 2M KOH (aqueous) electrolytes.

Cyclic voltammogram of rGO/NiO composite is shown in figure 4.9. rGO/NiO CV curves are almost similar to bare NiO CV curves. This suggests that the NiO component dominates the redox behaviour of the rGO/NiO composite. The separation between anodic and cathodic peaks deceases with decrease in the scan rate. The Ohmic resistivity and polarization during the redox reaction are responsible for the decreasing pattern of both the CV curve regions and the spacing between the anodic and cathodic peaks [13, 14].

Table 4.7 Specific capacitance values of rGO/NiO at different scan rates and electrolytes

rGO/NiO	**Specific capacitance (Fg^{-1})**			
Scan rate (mVs^{-1})	1M NaOH	2M NaOH	1M KOH	2M KOH
120	23.8	27.4	26.9	36
100	27.4	30.9	29	39.2
50	39.3	45.4	72.6	55.5
25	63.2	70.6	106	57.1
10	126	134	162	124
5	232	220	230	165
2	541	406		

From the CV graphs, it can be clearly seen that the redox peaks are good in 1M NaOH solution than other electrolytes. Also, the distance between anodic peak and cathodic peak is high for 1M NaOH. CV measurements clearly demonstrate that the rGO/NiO composite has significantly higher specific capacitance values than pure NiO, GO and rGO due to the synergistic effect. The specific capacitance values are calculated at different scan rates for all electrolytes and tabulated in table 4.7.

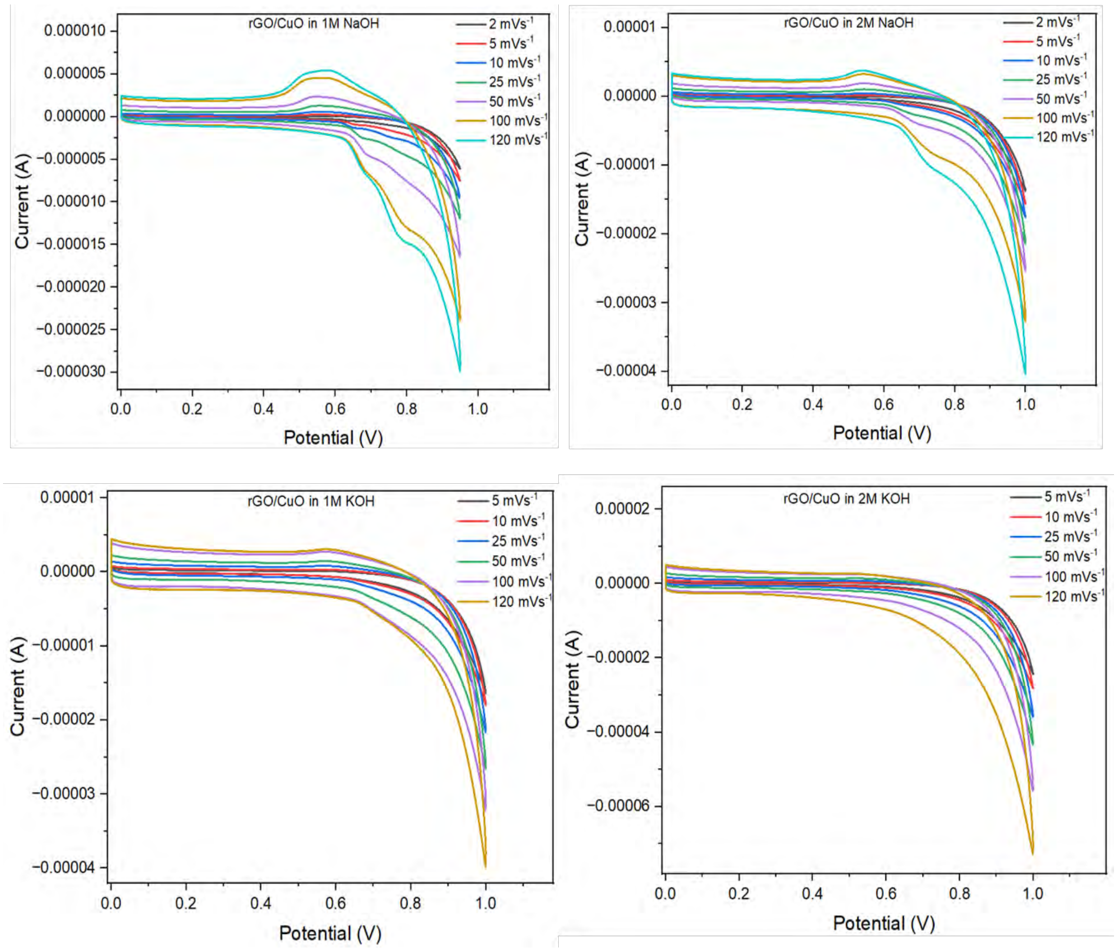

Fig. 4.10 CV curves of rGO/CuO at different scan rates in 1M NaOH, 2M NaOH, 1M KOH and 2M KOH (aqueous) electrolytes.

Cyclic voltammogram of rGO/CuO composite material at different scan rate are shown in figure 4.10. It can be clearly seen the redox peaks are present here. Pseudocapacitive nature dominates due to the presence of CuO. The distance between anodic peak and cathodic peak is high for 1M NaOH compared to other electrolytes. Specific capacitance is calculated and tabulated in the table 4.9 and it is higher than bare CuO, GO and rGO due to synergistic effect. Specific capacitance value decreases with increase in scan rate.

Table 4.8 Specific capacitance values of rGO/CuO at different scan rates and electrolytes

rGO/CuO	**Specific capacitance (Fg^{-1})**			
Scan rate (mVs^{-1})	1M NaOH	2M NaOH	1M KOH	2M KOH
120	43.8	46	48.7	43.3
100	45.1	46.6	51	48
50	55.8	56.43	62.9	58.92
25	70.3	70.39	71.9	68.637
10	120	102.34	101	99.87
5	180	148.89	159.01	155
2	327	297.8		

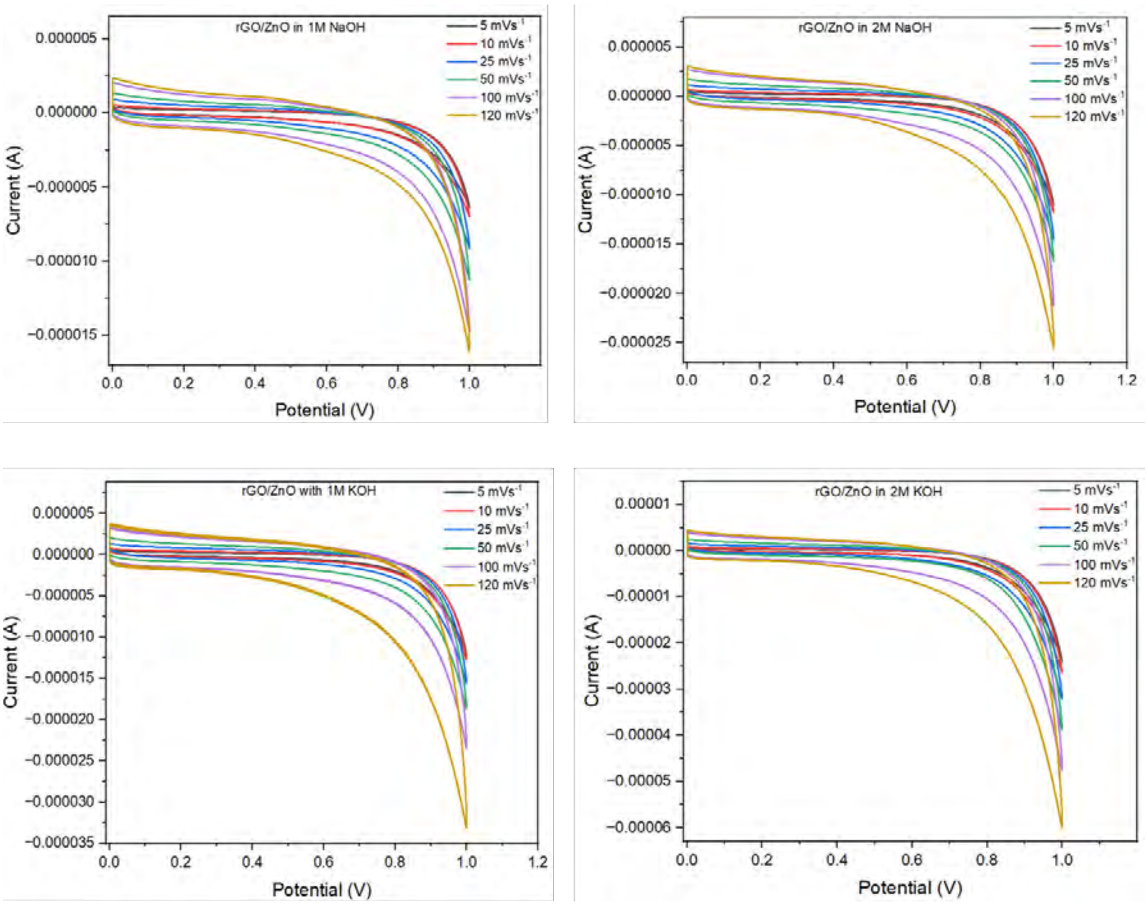

Fig. 4.11 CV curves of rGO/ZnO at different scan rates in 1M NaOH, 2M NaOH, 1M KOH and 2M KOH (aqueous) electrolytes.

Figure 4.11 shows the CV curves of rGO/ZnO at different scan rates from 2 mVs^{-1} to 120 mVs^{-1} in various steps. From these graphs it can be observed that the CV curves are not rectangular in shape. This suggests the existence of pseudocapacitance. As the scan rate increases, the specific capacitance value decreases and calculated values are listed in the table 4.9. Here the electrochemical activity is high for 2M KOH.

Table 4.9 Specific capacitance values of rGO/ZnO at different scan rates and electrolytes

rGO/ZnO	**Specific capacitance (Fg^{-1})**			
Scan rate (mVs^{-1})	1M NaOH	2M NaOH	1M KOH	2M KOH
120	21.9	32.4	35	41.29
100	22.8	32.7	43.07	51.11
50	32.4	44.7	50.2	55.90
25	50.2	52.08	64	70.12
10	80.4	87.35	114	110.43
5	124	132	138	146

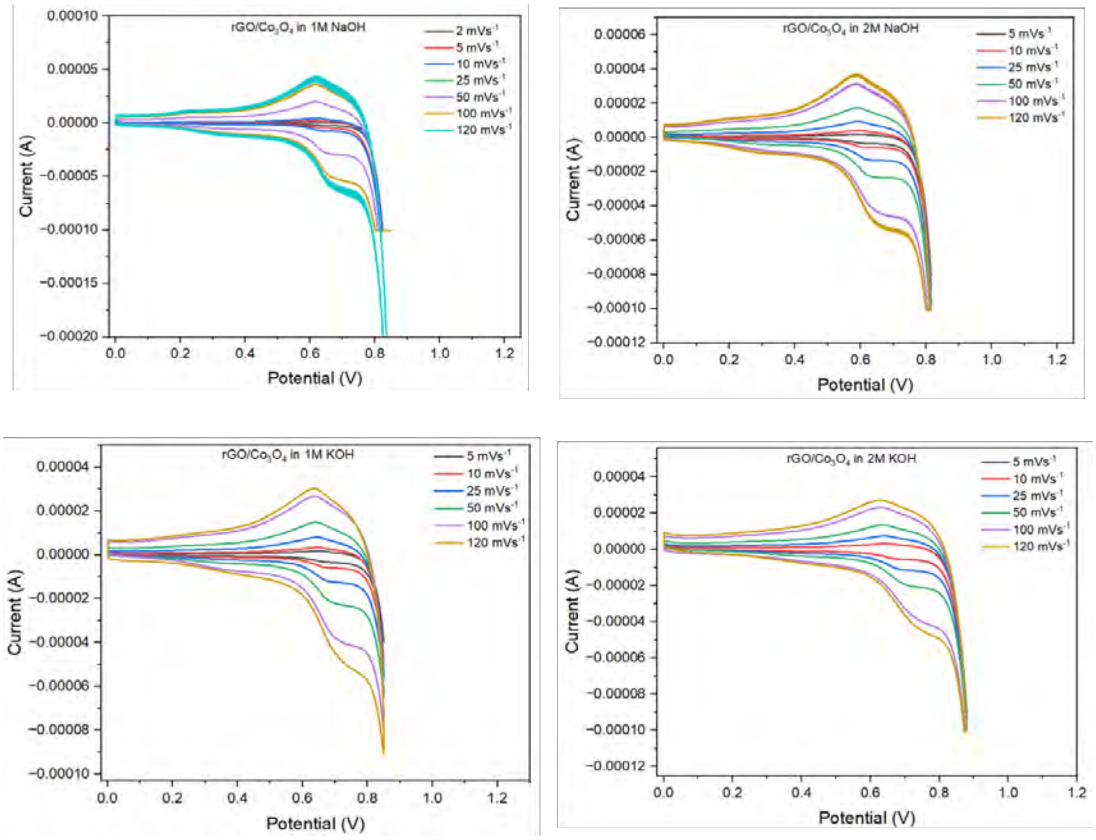

Fig. 4.12 CV curves of rGO/Co_3O_4 at different scan rates in 1M NaOH, 2M NaOH, 1M KOH and 2M KOH (aqueous) electrolytes.

Figure 4.12 depicts the rGO/Co_3O_4 composite at different scan rate. It can be clearly observed that the CV curves are having redox peaks and it has pseudocapacitive nature due to the presence of Co_3O_4. The distance between anodic peak and cathodic peak is more in 1M NaOH electrolyte solution compared to other three. Here the electrochemical activity is high in 1M NaOH solution. Specific capacitance is directly proportional to the area of the peak. The specific capacitance values are calculated and tabulated in the below table 4.10.

Table 4.10 Specific capacitance values of rGO/Co_3O_4 at different scan rates and electrolytes

rGO/Co_3O_4	**Specific capacitance (Fg^{-1})**			
Scan rate (mVs^{-1})	1M NaOH	2M NaOH	1M KOH	2M KOH
120	23.0	17.6	14.1	14.3
100	25.9	18.4	14.3	15.3
50	31.6	22.1	21	19
25	63.1	49.3	38.08	39.12
10	90.1	76.8	74.2	77.06
5	161.2	144	121	155
2	442			

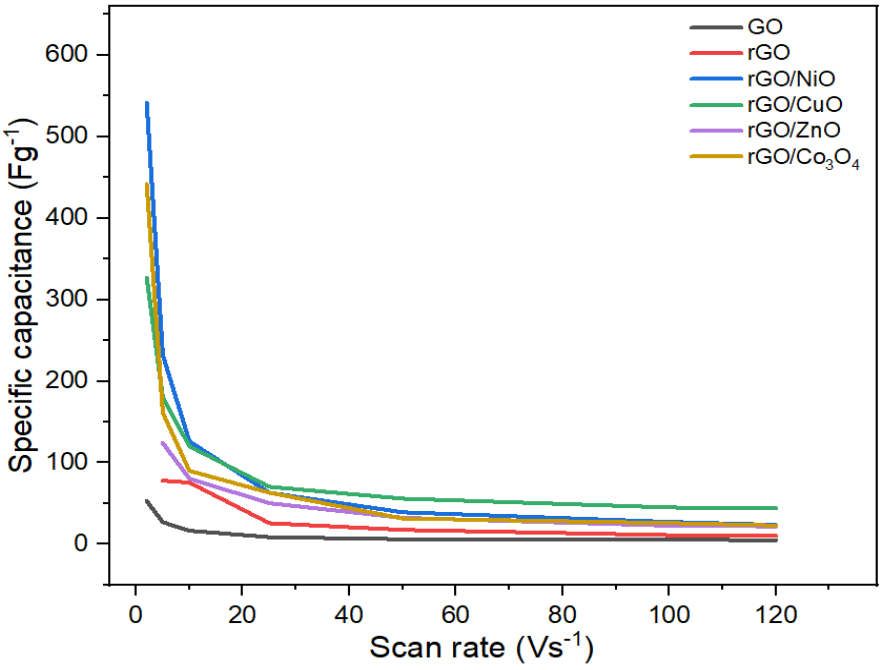

Fig. 4.13 Graph of specific capacitance versus scan rate

As the scan rate increases, the specific capacitance of the material decreases (shown in figure 4.13) because, at low scan rates, a huge number of ions are adsorbed on the inner and outer surfaces of the electrode materials resulting in a high specific capacitance. Due to slower ion transport at high scan rates, electrolyte ions are adsorbed only at the electrode's outer surface, resulting in decreased specific capacitance [4].

4.2.3 Electrochemical impedance spectroscopy

Electrochemical impedance spectroscopy (EIS) has been extensively utilized to characterize the performance of electrical energy storage and conversion devices such as electrochemical capacitors, batteries, and fuel cells [15- 23]. Individual electrodes used in electrochemical capacitors, corrosion testing, and capacitive deionization have also been characterized using it. The EIS could thus be used to investigate mass-transfer, charge-transfer, and diffusion processes. As a result, the EIS can investigate intrinsic material features or specific processes that may affect the conductance, resistance, or capacitance of an electrochemical system.

Nyquist plots depict the imaginary part $-Z_{im}$ of the complex impedance as a function of the real part Z_{re}. For electrodes made of transition metal oxides or conductive polymers capable of engaging in reversible redox reactions with ions present in the electrolyte, they typically consist of one or two semi-circles at relatively high frequencies and a non-vertical line with respect to the real axis at low frequencies [24]. EIS data of redox active electrodes with three electrodes numerically replicate for a wide range of electrode conductivity, electrolyte thickness, redox reaction rate constant, and bias voltage. The inset of the graph depicts zoomed part of the high frequency region.

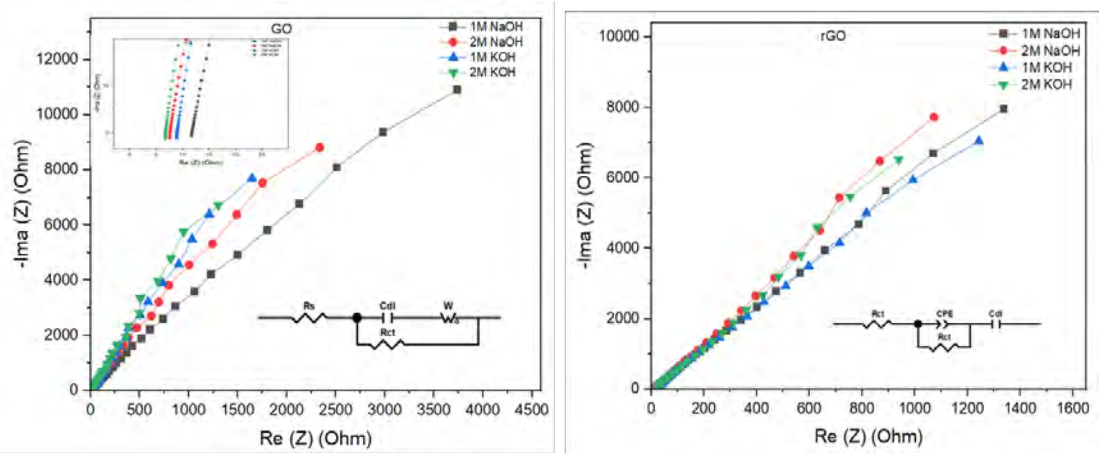

Fig. 4.14a EIS of GO and rGO in different electrolytes with equivalent circuit.

The Nyquist plot of GO and rGO is shown in Figure 4.14a. The behavior of an electrode is studied using Nyquist plot. A vertical straight line is seen at a low-frequency region, indicating that the electrodes have good capacitive performance. The semicircular arc is attributed to the double-layer capacitance, extrapolation of x intercept attrbuted to charge transfer resistance at the contact interface between electrode and electrolyte solution in the high-frequency zone. Using Z-view software, the impedance spectrum is studied by fitting an equivalent circuit. The component denoted with R_s is combinational resistance, which is the sum of the electrolyte's internal resistance and the contact resistance at the active material. The charge transfer resistance is R_{ct}, the double layer capacitor is C_{dl}, and the Warburg impedance is W. R_{ct} and C_{dl} values of GO are found to be 11.31 Ω and 9.1 μF respectively. rGO has R_{ct} and C_{dl} values of 16.02 Ω and 12.8 μF.

Rapid ion diffusion into the electrolyte and adsorption onto the electrode surface were evidenced by a nearly vertical line in the lower frequency band. The electrons may travel quickly due to less aggregation. GO has higher slope for KOH electrolyte compared to NaOH, whereas rGO shows higher slope value for NaOH electrolyte compared to KOH.

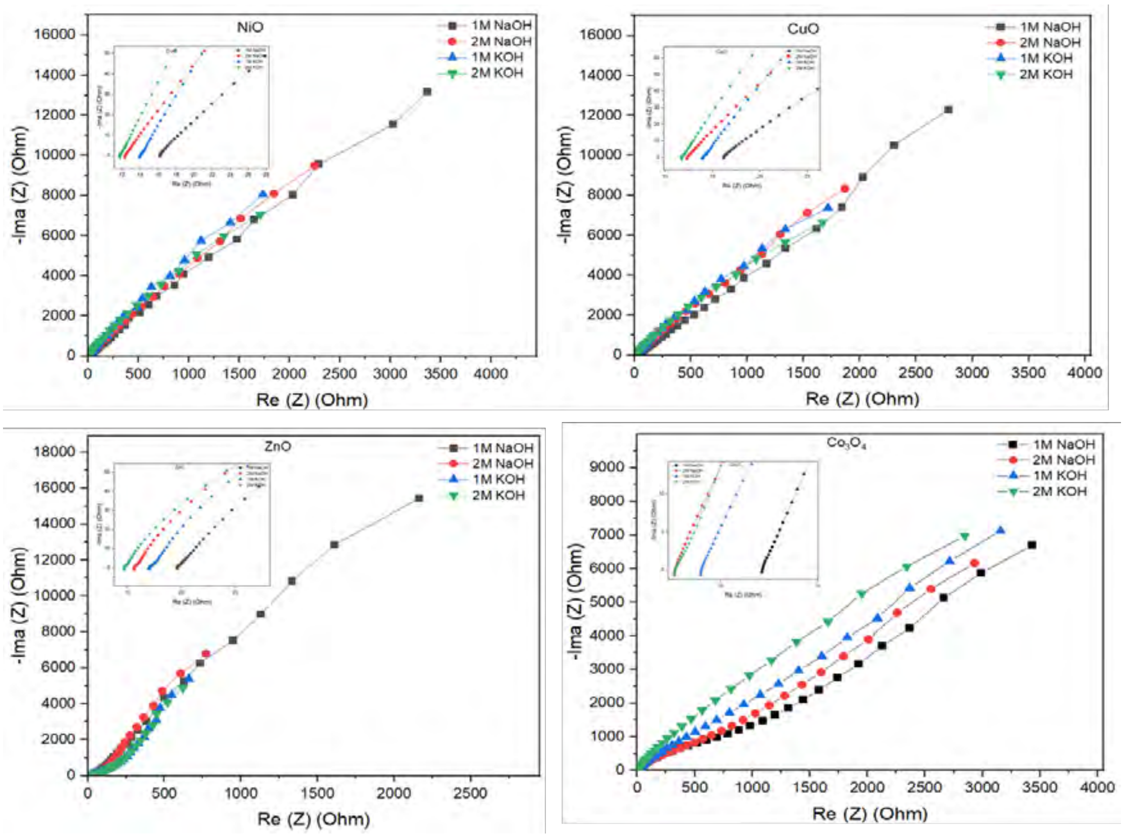

Fig. 4.14b EIS of NiO, CuO, ZnO and Co_3O_4 in different electrolytes.

Figure 4.14b depicts the EIS of NiO, CuO, ZnO and Co_3O_4. The inset of each graph depicts the high frequency region of EIS spectra. Rapid ion diffusion into the electrolyte and adsorption onto the electrode surface were evidenced by a nearly vertical line in the lower frequency band. The electrons may travel quickly due to less aggregation. NiO, CuO, ZnO and Co_3O_4 show higher slope value for KOH electrolyte compared to NaOH.

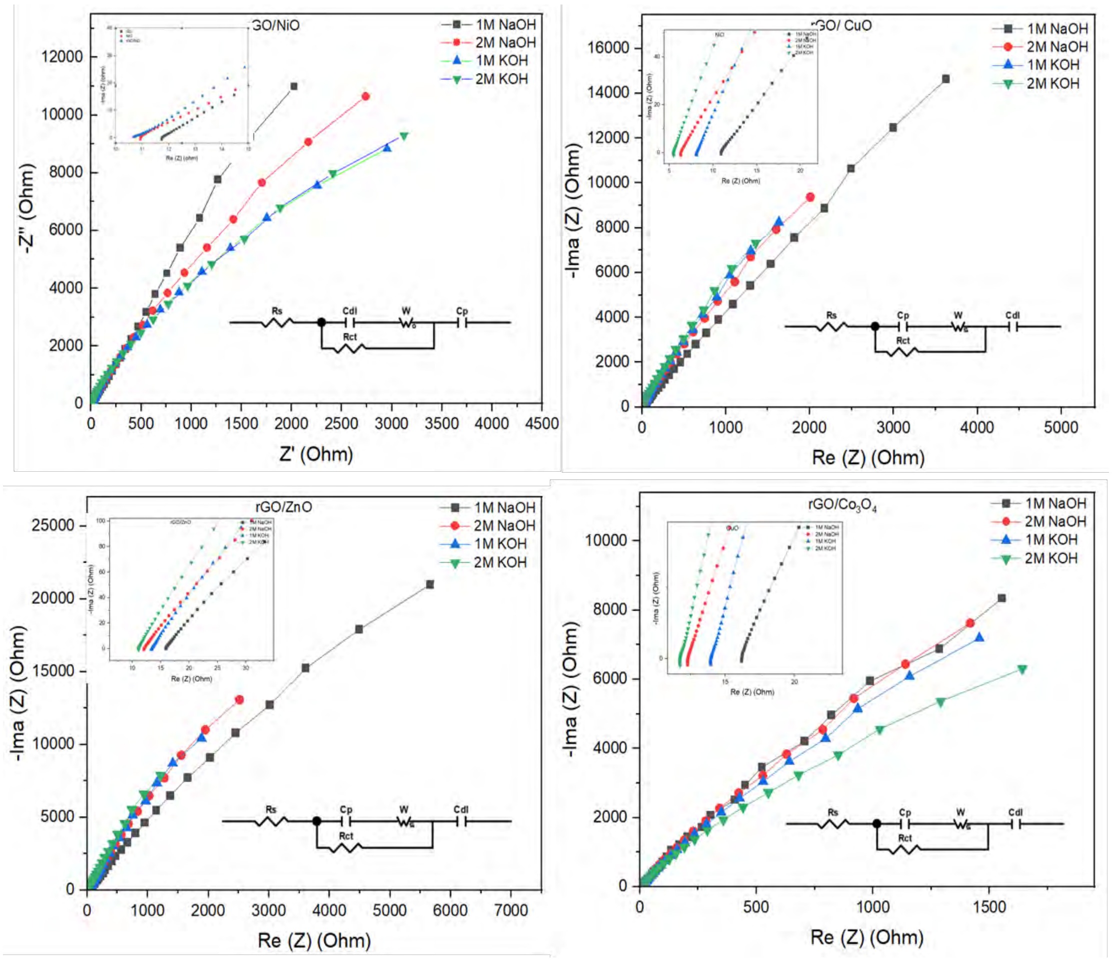

Fig. 4.15 EIS of rGO/NiO, rGO/CuO, rGO/ZnO and rGO/Co_3O_4 in different electrolytes with equivalent circuit.

Figure 4.15 depicts the Nyquist plot of rGO/NiO composite in various electrolytes. If the low frequency tail is parallel to the imaginary axis, the device exhibits low diffusive resistance. If the phase angle of the tail from the real axis is greater than 45, the device stores charge through the pseudocapacitive mechanism and has a high diffusive resistance. If the phase angle approaches 45 to 90, this indicates that both mechanisms are involved [25]. The tail is approaching 90 degrees in our experiment, showing that the device has a low diffusive resistance. The slope of the tail in the low frequency region of 1M NaOH solution is high, indicating that it has good capacitive behaviour. An equivalent circuit is fitted using Z-View software. The solution resistance, electrical double layer capacitance, charge transfer resistance, pseudo-capacitance, and Warburg resistivity are represented by R_s, C_{dl}, R_{ct}, C_p and W. The corresponding values of R_s, C_{dl}, R_{ct}, C_p for rGO/NiO composite are 10.5 Ω, 0.3 μF, 228 Ω and 0.13 μF. GO has R_s value of 11.2 Ω.

Nyquist plot of rGO/CuO also studied in different aqueous electrolytes such as NaOH and KOH. It shows higher value of slope for 2M KOH electrolyte and lower value for 1M NaOH electrolyte. This suggests that the electron diffusion is little less for NaOH electrolyte compared to KOH. An equivalent circuit is fitted using Z-View software. The solution resistance, electrical double layer capacitance, charge transfer resistance, pseudo-capacitance, and Warburg resistivity are represented by R_s, C_{dl}, R_{ct}, C_p and W. The corresponding values of R_s, C_{dl}, R_{ct}, C_p for rGO/CuO composite are found to be 9.495 Ω, 9.23 μF, 560 Ω and 0.164 μF respectively.

From the graph of EIS of rGO/ZnO we can observe that 2M KOH shows the higher ionic diffusion than other three. Equivalent circuit is fitted using Z-View software. The fitted values of R_s, C_{dl}, R_{ct}, C_p for rGO/ZnO composite are found to be 14.72 Ω, 6.41 μF, 584 Ω and 0.13 μF respectively.

Nyquist plot of rGO/Co_3O_4 composite studied in different aqueous electrolytes and an equivalent circuit is fitted using Z-View software. Here the fitted values of R_s,

C_{dl}, R_{ct}, C_p for rGO/ Co_3O_4 composite are found to be 10.53 Ω, 0.18 μF, 245 Ω and 0.6 μF respectively.

Both rGO/NiO composite and rGO/Co_3O_4 composite have low charge transfer resistance than rGO/CuO and rGO/ZnO so that the specific capacitance value of rGO/NiO composite and rGO/Co_3O_4 composite are high.

4.2.4 Galvanostatic charging and discharging

The standard technique for testing the performance and cycle life of supercapacitors and batteries is galvanostatic charge-discharge (GCD). A cycle is a repeated loop of charging and draining. The galvanostatic charge-discharge properties a sample at different current densities are plotted. The specific capacitance of samples is calculated using the relation (4.6)

$$C_s = (I_m \,.\, \Delta t) / (\Delta V) \quad \text{---------} \quad (4.6)$$

Where I_m is the current density, Δt is the discharge time and ΔV is the potential window.

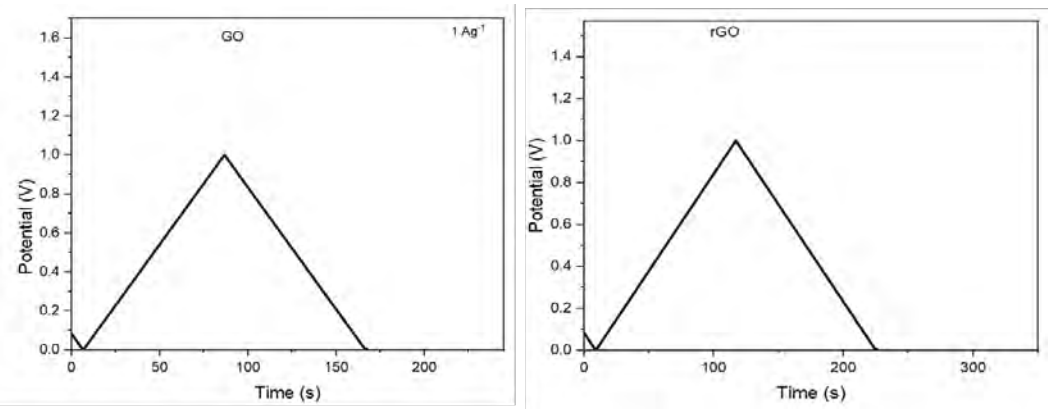

Fig. 4.16 GCD curves of GO and rGO

Figure 4.16 depicts the GCD curves of GO and rGO. GO and rGO both samples depict an ideal straight line for charging as well as discharging indicating the existence pure EDLC behaviour. At a given current density, the specific capacitance values are calculated using the relation 4.6. GO exhibits a specific capacitance of 86 Fg^{-1} at current density 1 Ag^{-1} and rGO exhibits 109 Fg^{-1} at same current density.

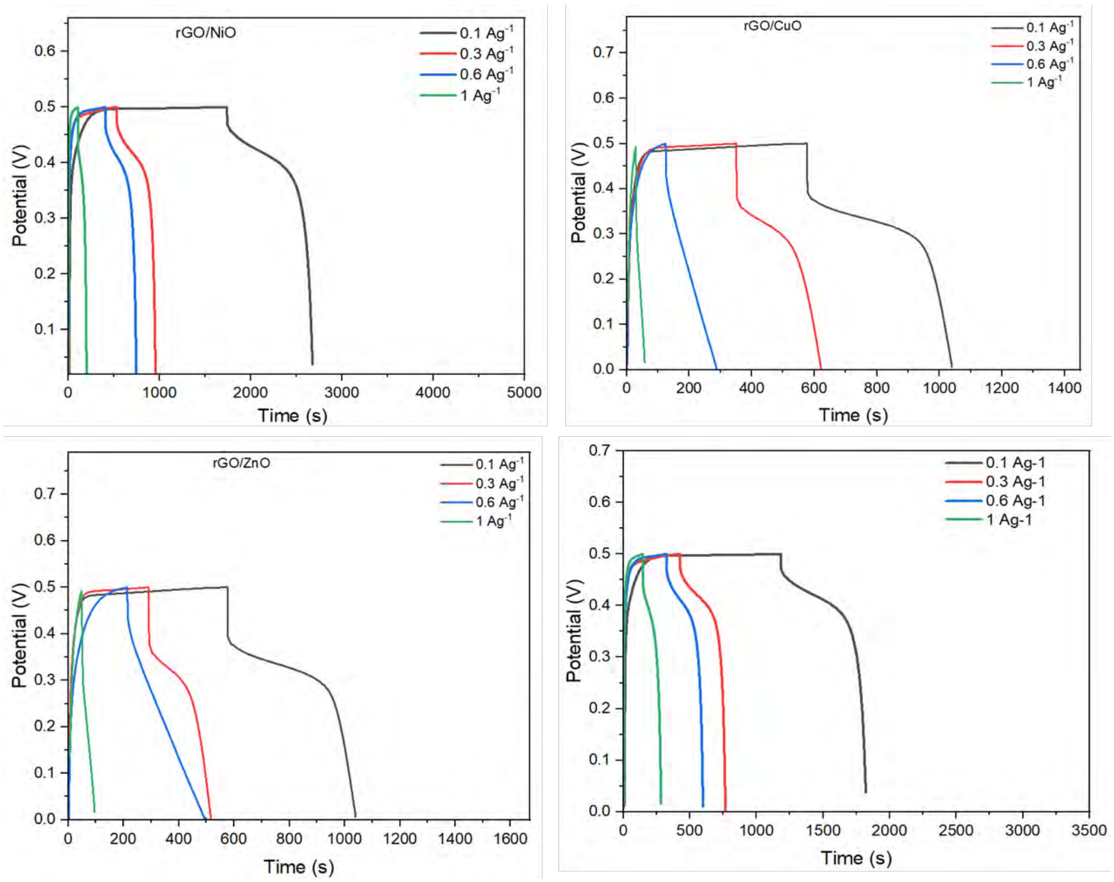

Fig. 4.17 GCD curves of rGO/NiO, rGO/CuO, rGO/ZnO and rGO/Co_3O_4 composites

Figure 4.17 depicts the GCD curves of rGO/NiO, rGO/CuO, rGO/ZnO and rGO/Co_3O_4 composites at different current density. Here the shape of charging and discharging curves are not a straight line which clearly indicates that the nature charge storage mechanism is pseudocapacitive. The nonlinear character of the CD curves clearly confirms the result of the CV measurements that the primary sources of charge storage in the composite material electrodes are Faradaic processes. Furthermore, the charge curves show that the majority of the capacitance is formed in the 0.01-0.5 V potential range, which corresponds to the Faradaic redox processes. The specific capacitance values are calculated at different current densities and tabulated in the below table 4.11.

Table 4.11 Specific capacitance values at different current densities

Material	**Specific capacitance (Fg^{-1}) at different current densities**			
	0.1 Ag^{-1}	**0.3 Ag^{-1}**	**0.6 Ag^{-1}**	**1 Ag^{-1}**
rGO/NiO	244.2	226.4	218.7	216
rGO/CuO	94.106	163.2	200.3	123.46
rGO/ZnO	94	138.02	197.68	109.2
rGO/Co_3O_4	127.52	196.82	215.14	188.88

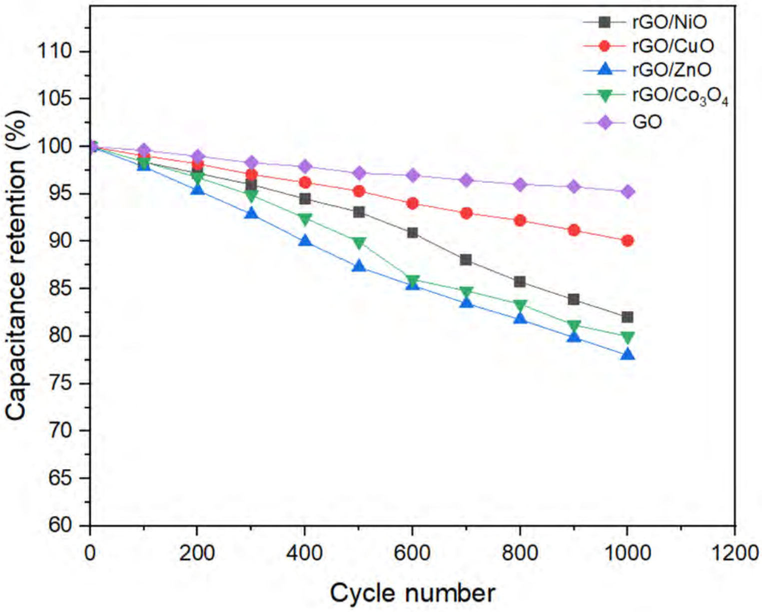

Fig. 4.18 Graph of capacitance retention over 1000 cycles.

Cycling stability is a critical property in real-world applications. The cycling stability of material was measured using constant current galvanostatic charge-discharge cycles at current density 0.6 Ag^{-1}. Figure 4.18 shows the graph of specific capacitance versus cycle number. The value of specific capacitance of rGO/NiO decreases to 95 % after 1,000 charge discharge cycles, specific capacitance of rGO/CuO decreases to 90%, specific capacitance of rGO/ZnO decreases to 78% and specific capacitance of rGO/Co_3O_4 decreases to 80%. Among all these samples rGO/NiO has better stability.

4.3 Two electrode system

Here the sample is coated on a substrate and a separator is placed in between two electrodes which is shown in figure 4.19. This device is connected to CH instrument for further studies. Here the working electrode is connected to one end of the device and reference and counter electrodes are shorted and connected to other end of the device, aluminium foils are used for connectivity. This is referred to as two-electrode system.

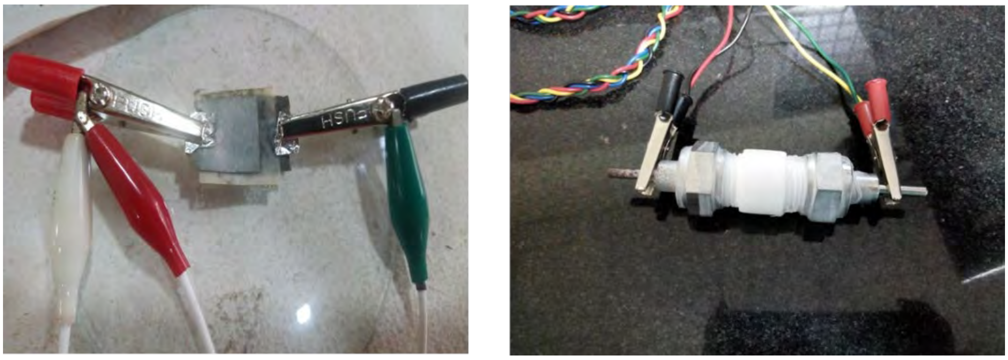

Fig. 4.19 Photographs of prepared electrodes connected to CH instrument

4.3.1 Preparation of electrodes for symmetric supercapacitors

- Electrodes were prepared using Whatman filter paper.
- The filter paper was cut into two pieces of dimension 2x2 cm.
- Active material was crushed properly and isopropanol was added to it to prepare a paste.
- This paste was gently coated on the filter paper of dimension 2x2 cm.
- A separator of dimension 2.2 x 2.2 cm was placed in between two electrodes.
- 1M NaOH solution was prepared as an electrolyte.

4.3.2 Cyclic voltammetry

In a two-electrode system, the electrochemical performance of GO, rGO and rGO/metal oxides composites for supercapacitors is performed using cyclic voltammetry (CV), galvanostatic charging-discharging curves, and electrochemical impedance spectroscopy (Nyquist plot) in 1M NaOH electrolyte.

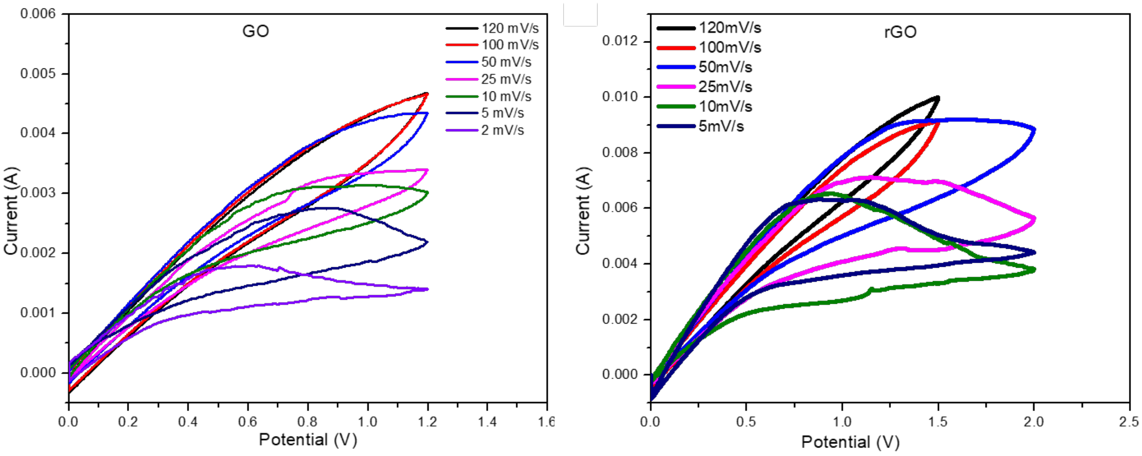

Fig. 4.20 CV curves of GO and rGO at different scan rates

Figure 4.20 depicts the CV curves of GO and rGO at different scan rates. Here the specific capacitance (C_s) values are calculated using the relation 4.7.

$$C_s = \frac{1}{2\, m\, s\, \Delta V} \int_{Vi}^{Vf} I(V)dV \quad \ldots\ldots\ldots\ldots\ldots\ldots.. \ (4.7)$$

Where m is the mass of active material, s is the scan rate, $\Delta V = V_f - V_i$ is the potential window and I(V) is the instantaneous current. Integral part is the area of the curve in voltammogram. C_s is directly proportional to the area of the CV curve. From the above figure it can be clearly seen that the area of the CV curve is more for rGO compared to GO. The specific capacitance values for 1 M NaOH electrolyte are calculated for scan rates of 120, 100, 50, 25, 10, 5 and 2 mVs^{-1} and are tabulated in the below table 4.12. The number of ions deposited on the electrode surface reduces as the scan rate increases. As a result, the material's specific capacitance decreases with scan rate.

The electrochemical behaviour of rGO is also studied in 1M KCl solution. The CV graph is depicted in the figure 4.21. The specific capacitance values are calculated according the relation 4.7 and all the values are tabulated in the table 4.12

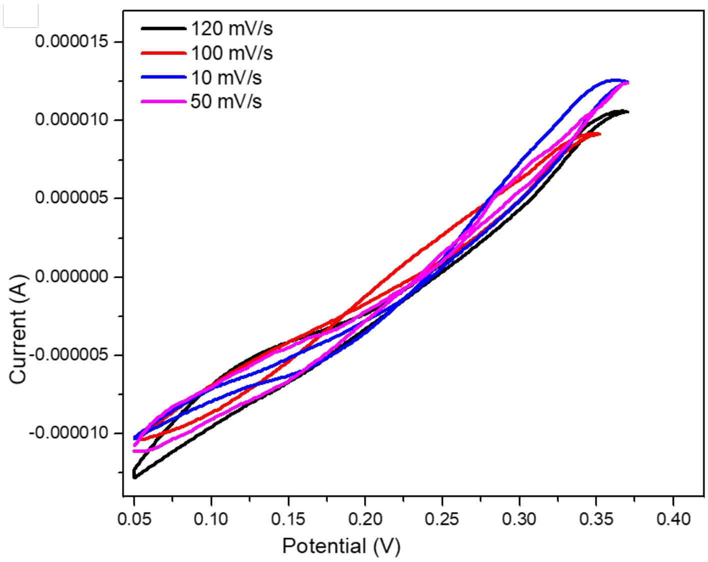

Fig. 4.21 CV curves rGO at different scan rates in 1M KCl electrolyte.

Among these two electrolytes, NaOH has a larger specific capacitance of rGO than KCl. This is due to the fact that the ionic radius of Na^+ ion is less than that of K^+ ion. The ionic radius is crucial parameter in this case. Ion diffusion into the electrode is aided by a low ionic radius. It also has ample time to interact with the electrode material and eliminate the surrounded water molecules. Along with this result, the mobility of OH^- ion (20.6×10^{-5} cm^2 s^{-1} v-1) is larger than that of cl^- ion ($7.91x10^{-5}$ cm^2 s^{-1} v^{-1}) [25]. This will help to enhance the specific capacitance value.

Table 4.12 Specific capacitance values at different scan rates in 1M KCl electrolyte

Scan rate (mVs^{-1})	**C_s in 1M KCl electrolyte (Fg^{-1})**
120	0.611
100	1.423
50	1.532
10	7.79

Figure 4.22 depicts the CV curves of rGO/metal oxides composites at different scan rates. The specific capacitance values are calculated using the relation 4.7 and values are tabulated in the below table 4.13.

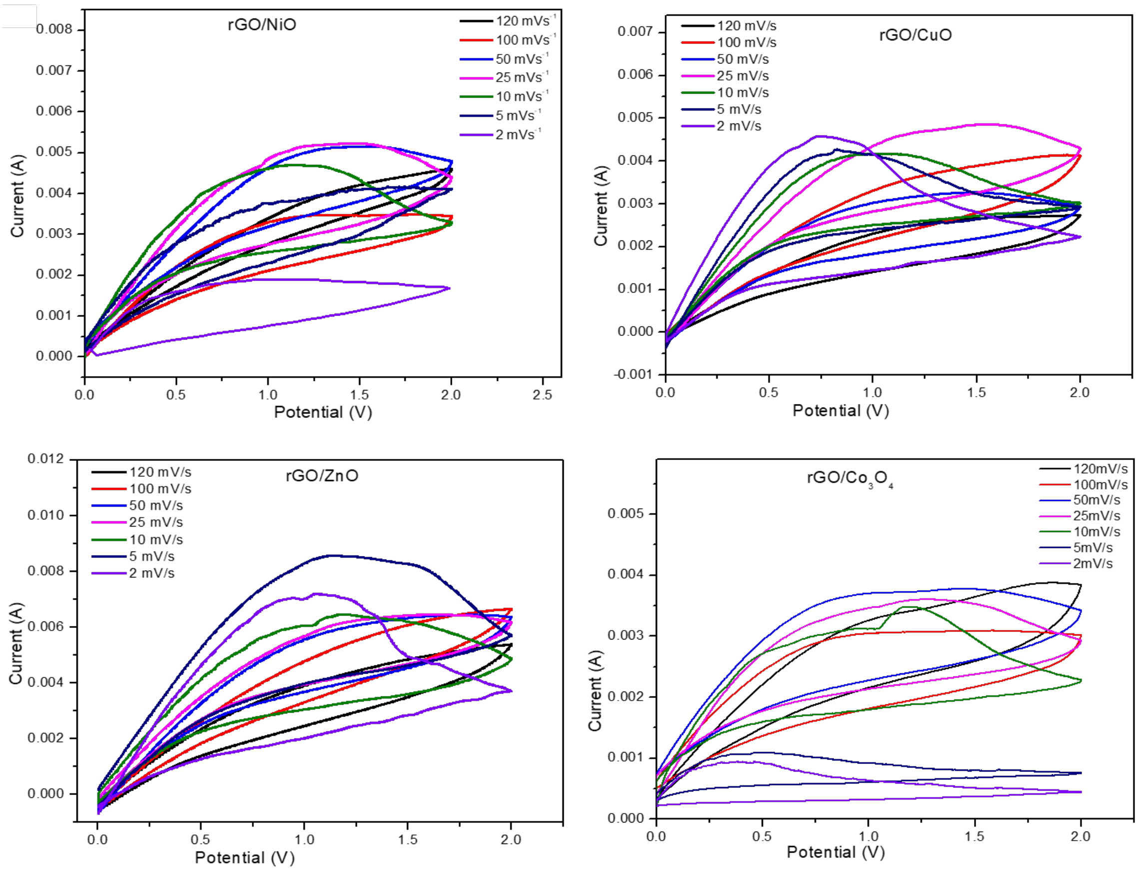

Fig. 4.22 CV curves of composite materials at different scan rates.

Table 4.13 Specific capacitance values at different scan rates

Materials	**Specific Capacitance (Fg^{-1})**						
	120 mVs^{-1}	**100 mVs^{-1}**	**50 mVs^{-1}**	**25 mVs^{-1}**	**10 mVs^{-1}**	**5 mVs^{-1}**	**2 mVs^{-1}**
GO	1.56	2.01	4.13	10.2	13.87	38.75	61.19
rGO	3.9	4.96	23.47	54.62	97.5	123.12	148.6
rGO/ NiO	1.68	3.41	8.04	24.54	45.45	113.6	227.3

rGO/ CuO	2.5	4.1	7.95	20.25	45	180	425
rGO/ ZnO	4	5.738	13	26.44	119.44	313.88	409.75
rGO/ Co_3O_4	9.6	12.86	28.56	50.28	130.68	289.6	360.4

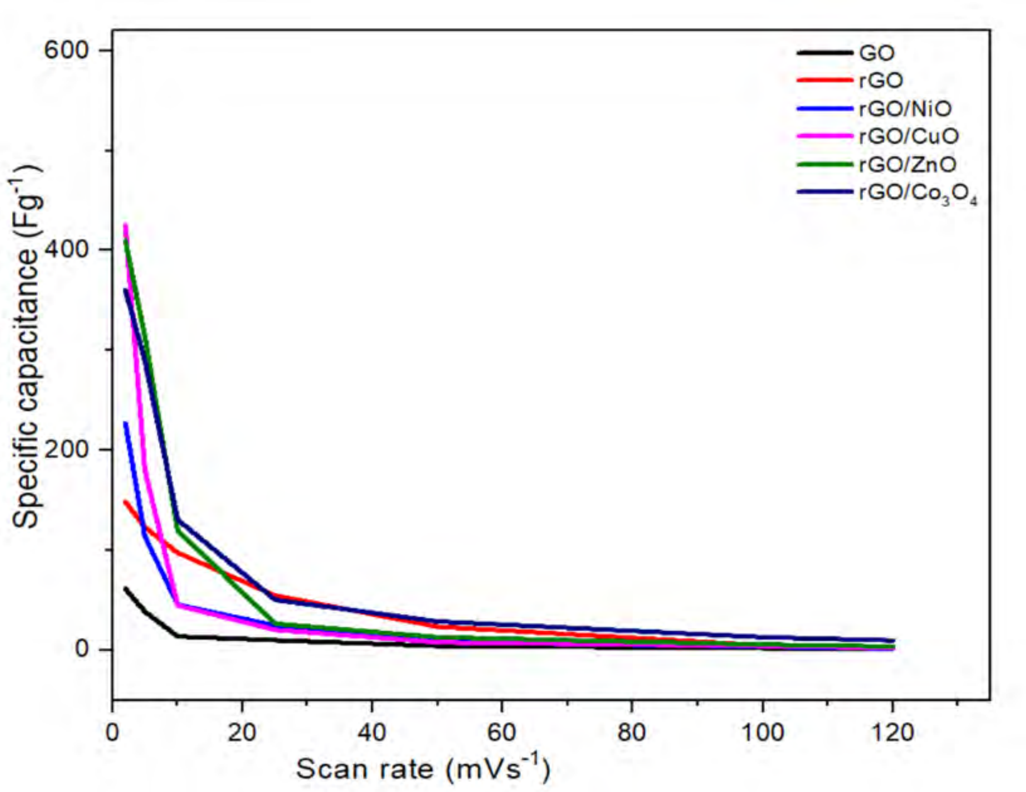

Fig. 4.23 Graph of specific capacitance versus scan rate

Figure 4.23 depicts a graph of specific capacitance versus scan rate. It can be observed that the specific capacitance values decrease with increase in the scan rate.

Cycle stability is another critical criterion for supercapacitors. The prepared sample's cyclic stability is examined over 1000 cycles at a scan rate of 120 mVs^{-1}. All samples showed good cycle stability and are above 85%.

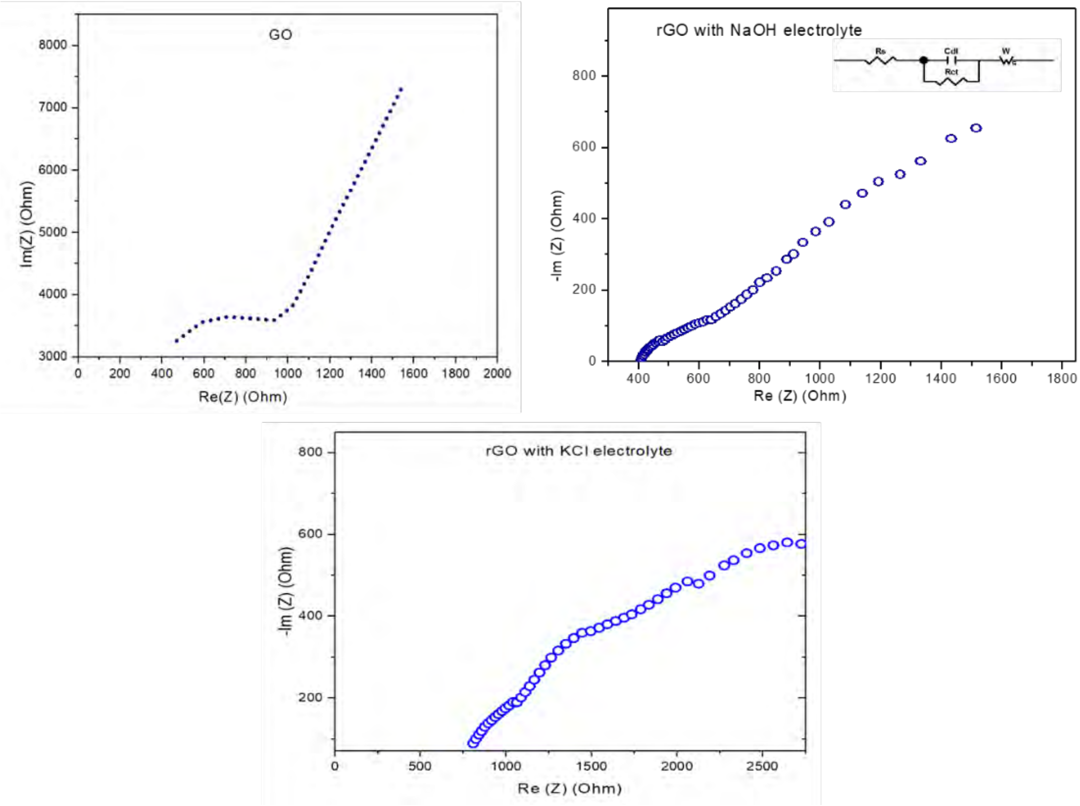

Fig. 4.24 EIS spectra of GO and rGO in 1M NaOH and 1M KCl electrolytes.

4.3.3 Electrochemical impedance spectroscopy

The Nyquist plots of GO and rGO are shown in Fig. 4.24. It depicts the electrode's behaviour. A nearly vertical straight line is visible at a low-frequency area, indicating that the electrodes have good capacitive performance. The semi-circular arc is attributed to the double-layer capacitance, parallel charge transfer resistance at the contact interface between electrode and electrolyte solution in the high-frequency zone. Using Z-view software, the impedance spectrum is studied by fitting an equivalent circuit. The component denoted by R_s is combinational resistance, which is the sum of the electrolyte's internal resistance and the contact resistance at the active material. The charge transfer resistance is R_{ct}, the double layer capacitor is C_{dl}, and the Warburg impedance is W. R_s, R_{ct}, and C_{dl} fitted values are 300 Ω, 759 Ω and 19.744 µF, respectively.

Nyquist plot of composite materials are shown in figure 4.25. A nearly vertical straight line is visible at a low-frequency area, indicating that the electrodes have good capacitive performance. The semi-circular arc is attributed to the double-layer capacitance, parallel charge transfer resistance at the contact interface between electrode and electrolyte solution in the high-frequency zone. An equivalent circuit is fitted using Z-View software.

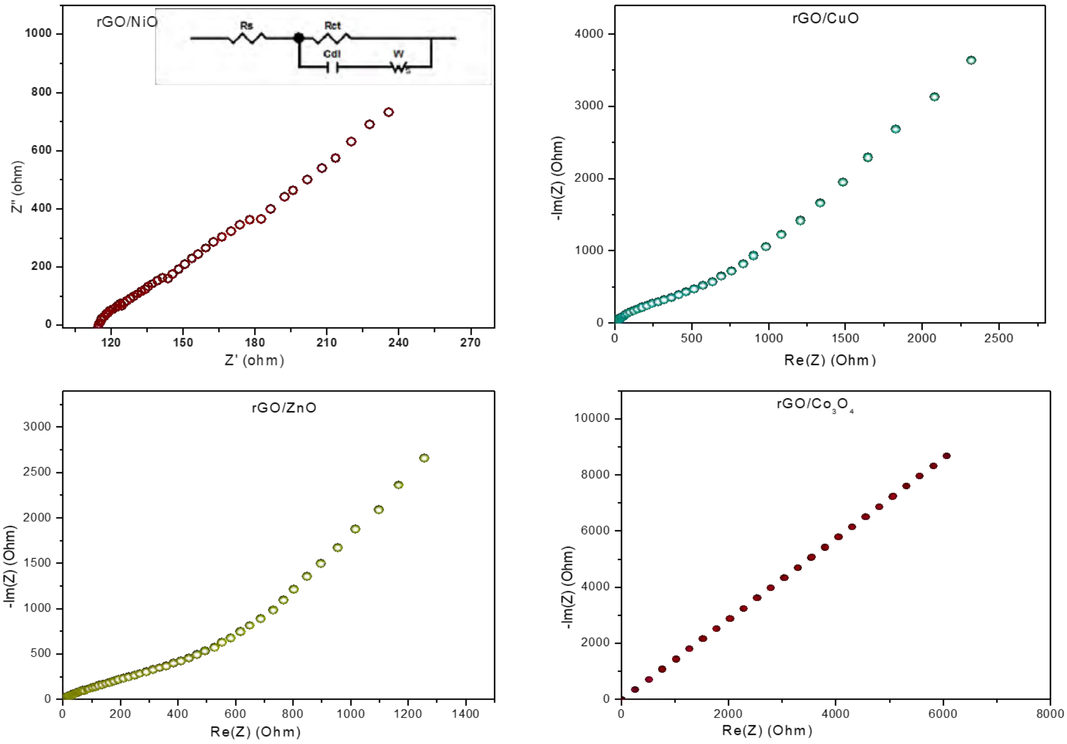

Fig. 4.25 EIS spectra of composite materials in 1M NaOH.

4.3.4 Galvanostatic charging and discharging

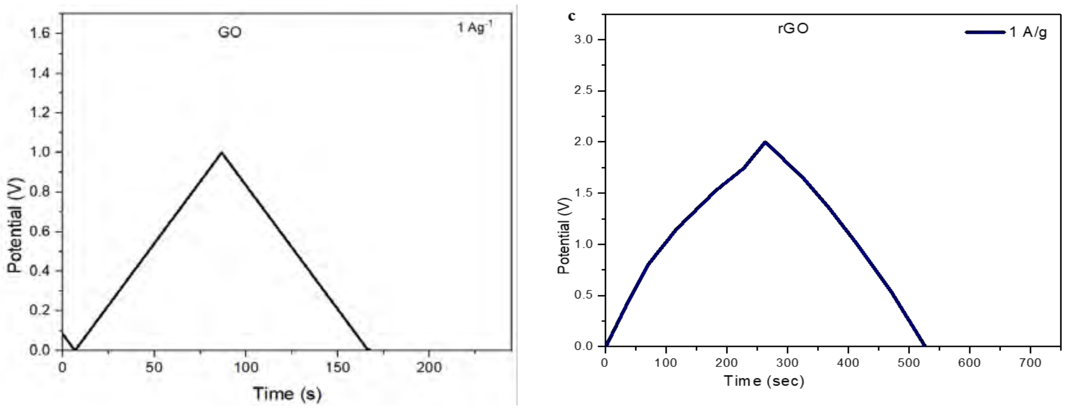

Fig. 4.26 GCD curves of GO and rGO.

The galvanostatic charge-discharge curves of GO and rGO are depicted in figure 4.26 with a current density of 1 Ag^{-1}.

$$C_s = It / (m\Delta t) \ldots\ldots\ldots\ldots (4.8)$$

is the formula for calculating specific capacitance. Where I is the charge/discharge current, Δt is the discharging time, m is the active material mass. Here we can clearly observe that the shape of curves is linear which indicates the double layer capacitor. The specific capacitance of GO and rGO are found to be 80 and 131 Fg^{-1} at the current density 1 Ag^{-1}.

Figure 4.27 shows the GCD curves of rGO/metal oxides at a current density of 1 Ag^{-1}. Here the shape of charging and discharging curves are not linear which indicates the pseudocapacitive type of behaviour. Specific capacitance values are calculated using the relation 4.8 and all the values are tabulated n the below table 4.14.

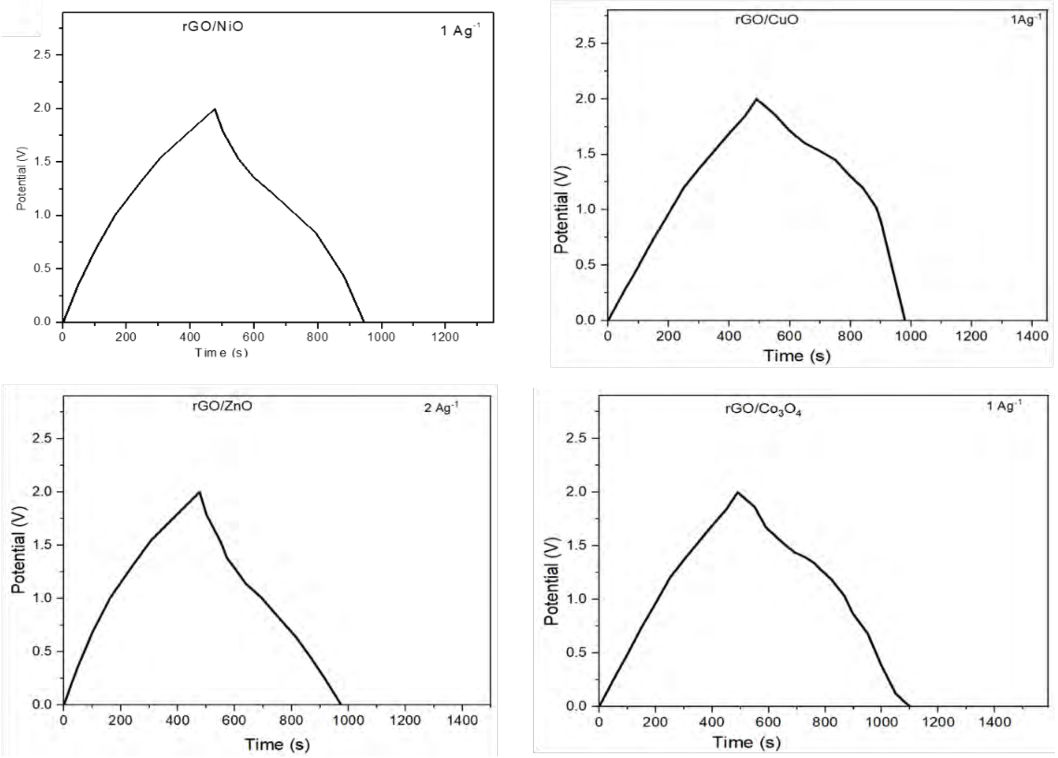

Fig. 4.27 GCD curves of composite materials

Table 4.14 Specific capacitance values at a given current density

Sample	Specific capacitance (Fg^{-1})
rGO/NiO	234.6
rGO/CuO	243.5
rGO/ZnO	364.2
rGO/Co_3O_4	305

Energy density is one of the crucial parameters for supercapacitor. Energy density is calculated according to the relation 4.9.

$$E = \frac{1}{2m} CV^2 \quad \Longrightarrow \quad E = \frac{1}{2} C_s V^2 \quad \ldots\ldots\ldots\ldots\ldots\ldots (4.9)$$

Where E is the energy density (Wh Kg^{-1}), C_s= C/m is the specific capacitance in Fg^{-1}, V is the potential window in V. The energy density is calculated for all the composite materials and tabulated in the table 4.14.

The time rate of energy transfer per unit volume is the power density and it explains how rapidly the device's reserved energy can be transferred to an external load. It can be calculated by using equation (4.10)

$$P = \frac{E}{t} 3600 \quad \ldots\ldots\ldots\ldots\ldots\ldots (4.10)$$

Here P is the power density (W Kg^{-1}), E is the energy density (Wh Kg^{-1}) and t is the discharge time (s).

Among all four composite materials rGO/NiO shows higher value of energy density.

Table 4.15 Energy density and power density of composite materials

Material	Energy density (WhKg^{-1})	Power density (WKg^{-1})
rGO/NiO	32.85	270
rGO/CuO	20.85	272.80
rGO/ZnO	16.88	275.44
rGO/Co_3O_4	25.37	269.46

4.4 Summary

In summary, GO was synthesized using a modified Hummers method, and rGO was effectively synthesized using a non-toxic and environmentally friendly reducing agent. All the composites were synthesized by a simple sonochemical method. Electrochemical performances (CV, EIS and GCD) were carried out for all the prepared samples using three-electrode as well as two-electrode systems. CV studies were carried out in 1M NaOH, 2M NaOH, 1M KOH and 2M KOH electrolyte solutions in three-electrode cell. GO shows good electrochemical activity in KOH electrolyte but rGO shows good results for NaOH electrolyte. Therefore, we have used 1M NaOH electrolyte for two electrode system for all the prepared electrodes. CV curves and GCD curves provide the clear information about nature of charge storage mechanism. GO and rGO are EDLC type and bare metal oxides and composites are pseudocapacitive type of charge storage devices. EIS spectra give information about diffusion of ions, series resistance, solution resistance and all. Equivalent circuit was fitted using Z-View software to get the values of R_s, R_{ct}, C_{dl}, and C_p. Energy density and power density are calculated for all the composite materials. Energy density is good for rGO/NiO composite compared to other samples.

References

[1] J.R. Norris, D.W. Ribbons, *Methods in Microbiology (Volume 6B)*, 1972, (Academic press, London and New York).

[2] Noemie Elgrishi, J. Kelley, Rountree, D. Brian, McCarthy, S. Eric, Rountree, T. Thomas, Eisenhart, Jillian L. Dempsey, *J. Chem. Educ.* **95** (2018) 197.

[3] Ong Gerard, Arshid Numan, Syam Krishnan, Mohammad Khalid, Ramesh Subramaniam, Ramesh Kasi, *J. Energy Storage*, **50** (2022) 104283.

[4] Kalimuthu Vijaya Sankar, Ramakrishnan Kalai Selvan, *Carbon*. **90** (2015) 260.

[5] Yuanlong Shao, Hongzhi Wang, Qinghong Zhang, Yaogang Li, *NPG Asia Mater*. 6 (2014) 1

[6] Y. Fang, B. Luo, Y. Y. Jia, X. L. Li, B. Wang, , Q. Song, F. Y. Kang, L. J. Zhi, *Adv. Mater*. **24** (2012) 6348.

[7] B. Xu, S. F. Yue, Z. Y. Sui, X. T. Zhang, S. S. Hou, G. P. Cao, Y. S. Yang, *Energy Environ.* Sci. **4** (2011) 2826.

[8] Cheng Zhong, Yida Deng, Wenbin Hu, Jinli Qiao, Lei Zhang, Jiujun Zhang, *Chem. Soc. Rev*. **44** (2015) 7484.

[9] A.K. Singh, D. Sarkar, G.G. Khan, K. Mandal, *J. Mater.Chem. A* **1 (**2013) 12759.

[10] P. Justin, S.K. Meher, G.R. Rao, *J. Phys. Chem. C* **114 (**2010**)** 5203.

[11] G.A. Babu, G. Ravi, T. Mahalingam, M. Kumaresavanji, Y. Hayakawa, *Dalton Trans.* **44** (2015) 4485.

[12] Baiju Vidhyadharan, Izan Izwan Misnon, Radhiyah Abd Aziz, K. P. Padmasree, Mashitah M. Yusoff, Rajan Jose, *J. Mater.Chem. A,* 2 (2014) 6578.

[13] M. Li, M. Zu, J. Yu, H. Cheng, Q. Li, *Small* **13** (2017) 1.

[14] R. Li, S. Wang, Z. Huang, F. Lu, T. He, *J. Power Sources*, **312** (2016) 156.

[15] Bing-Ang Mei, Obaidallah Munteshari, Jonathan Lau, Bruce Dunn, Laurent Pilon, *J. Phys. Chem. C*, **122** (2018) 194.

[16] Conway, B. E. Electrochemical Supercapacitors: Scientific Fundamentals and Technological Applications, 1999 (Kluwer Academic/Plenum Publishers: New York).

[17] R. Kotz, M. Carlen, *Electrochim. Acta*, **45** (2000) 2483.

[18] P. L. Taberna, P. Simon, J. F. Fauvarque *J. Electrochem. Soc.* **150** (2003) 292.

[19] J. R. Miller, R.A. Outlaw, B. C. Holloway, *Science*, **329** (2010) 1637.

[20] M. D. Levi, D. Aurbach, *J. Phys. Chem. B*, 101 (1997) 4630.

[21] F. L. Mantia, J. Vetter, P. Novak, *Electrochim. Acta*, **53** (2008) 4109.

[22] J. M. Atebamba, J. Moskon, S. Pejovnik, M. Gaberscek, J. Electrochem. Soc. 157 (2010) 1218.

[23] He, Z.; Mansfeld, F. Energy Environ. Sci. 2009, 2, 215 Bing-Ang Mei, Jonathan Lau, Terri Lin, Sarah Tolbert, Bruce Dunn, Laurent Pilon, *J. Phys. Chem. C*, **43** (2018) 24499.

[24] Kalimuthu Vijaya Sankar, Ramakrishnan Kalai Selvan, *Carbon*. **90** (2015) 260.

Conclusions

The main intension of developing supercapacitors is to fulfill the need for storing renewable energy. The performance of supercapacitors is highly influenced by the electrode materials as well as electrolyte. Transition metal oxides are the most preferred materials due to their higher energy density and specific capacitance than carbon materials, as well as their higher chemical stability than conductive polymers. Even though RuO_2 has higher value of capacitance, the use of this material in supercapacitors is hindered due to its toxicity and high cost. Metal oxides such as NiO, Co_3O_4, ZnO, CuO replace the use of RuO_2. However, Existing issues, such as low conductivity, limit their practical implementation in electrode materials. As a result, we have proposed some solutions to the problems.

(i) Nanoscale material preparation. The compact size increases the contact surface and decreases the distance between materials and electrolyte. The fundamental electrical and optical properties vary significantly depending on the size of the substance.

(ii) Making use of the synergistic effect. It is critical that the synergistic impact between different components be employed to increase electrochemical performance through various combinations of carbon materials and transition metal oxides.

Modified Hummers method was implemented for the synthesis of GO due to its simplicity and high yield. Phyllanthus Emblica was successfully used as a reducing agent to avoid hazardous chemicals. Combination of rGO metal oxides improves the surface area as well as conductivity.

In the present work, rGO with NiO, CuO, ZnO and Co_3O_4 composites were prepared by sonochemical method. The characterization of prepared samples was carried out using XRD, FTIR, Raman spectra. Morphology was studied by SEM and TEM images. EDX confirmed that there are no additional peaks which clearly says that there is no impurities present in samples. XRD analyses provide structural information about the synthesized sample, and decrease in the value of d spacing after reduction of GO ensures that oxygen functional groups are removed. The FTIR spectra was used to identify the functional groups. Raman spectra revealed an increase in the I_D/I_G ratio after GO was reduced. This represents the rGO plane's deformation. The details of morphology were studied by SEM and TEM. Here we observed that the metal oxide nanoparticles are well decorated on the surface of rGO.

Electrochemical performance was studied by CV, EIS and GCD with three electrode and two-electrode systems in 1M NaOH, 2M NaOH, 1M KOH and 2M KOH electrolytes. CV studies confirms the nature of charge storage mechanism and specific capacitance of all prepared samples was calculated. rGO shows good capacitive behavior than GO. Solution resistance and charge transfer resistance were taken by plotting an equivalent circuit. Charge discharge cycles also give specific capacitance value. By looking into all the electrochemical studies, we can observe that rGO/NiO and rGO/Co_3O_4 have higher value of specific capacitance compared to other two. From all these, we can conclude that amla extract is an excellent reducing agent and also environmentally friendly. The composite material prepared from this is a very good electrode material for supercapacitors.

Future scope

Although significant advancements in transition metal oxide-based electrode materials, low energy density remains a barrier to the development of supercapacitors.

Future work on supercapacitor electrodes should be focussed on following points.

(i) Researchers should focus their efforts on obtaining raw materials for electrodes at a low cost and with environmentally friendly nature.

(ii) The study of flexible supercapacitors is driven by the growth of portable and wearable electronic devices. That is, in addition to improving energy density, it is important to ensure capacitance performance stability under various bending and deformation conditions.

(iii) There are now numerous publications on transparent and flexible electrodes for solar batteries. Furthermore, supercapacitors based on battery-type electrodes have received a lot of attention. Simultaneously, hybrid supercapacitors can bridge the gap between traditional metal ion batteries and supercapacitors. We wonder if supercapacitors will be able to charge from the sun in the future. If the miracle comes true, it will mark a tremendous step forward in the development of supercapacitors.

List of publications

1. Reduction of graphene oxide by Phyllanthus Emblica as a reducing agent – A green approach for supercapacitor application.

D.R. Madhuri, K. Kavyashree, Ashok R Lamani, H.S. Jayanna, G. Nagaraju, Shridhar Mundinamani.

Materials Today: Proceedings, **49** (2022) 865.

2. A Simple sonochemical method of synthesis of rGO/Co_3O_4 composite with binder free electrode for supercapacitors.

D.R. Madhuri, K. Kavyashree, Ashok R Lamani, H.S. Jayanna, G. Nagaraju, Shridhar Mundinamani.

Proceedings of the DAE Solid State Physics Symposium, **55** (2021) 1027.

ISBN No: 81-8372-085-4

3. Effect of graphite particle size on oxidation of graphene oxide prepared by Modified Hummers method.

K. Kavyashree, **D. R. Madhuri**, Ashok R. Lamani, H. S. Jayanna, and M. Hemantha

AIP Conf. Proc., **2265** (2020) 030096.

Presentations/ participations in International and National conferences/Webinars/ National seminars/ Symposiums/ workshop.

1. **Poster presentation** in 65th DAE Solid State Physics Symposium held at BARC, Mumbai during December 15-19, 2021.

2. Completed an online certificate course on Nanomaterials Synthesis and Characterization Techniques held at Shri Shivaji Science College, Amravati during August 26 – September 8, 2021.

3. Participated in a webinar on Nanoscience & Technology: Education and career Prospects held at Karunya Institute of Technolgy and Sciences (Deemed to be University), Coimbatore on June 4, 2021.

4. Participated in an International webinar on Green Technology: Role of Chemistry and catalysis for the advancement of sustainable society, held at Reva University, Bengaluru on May 24, 2021.

5. Participated in a faculty development program on accelerating innovations in material science - surface characterization held at BMS Institute of Technology & Management, Bengaluru during May 18 - 22, 2021.

6. Participated in a webinar on Basics of electron microscopy organized by Jyothi institute of Technology, Bengaluru on August 8, 2020.

7. **Poster presentation** in an international conference on Accelerating Innovations in Material Science (AIMS 2020) organized by department of Chemistry, BMS Institute of Technology and Management, Bengaluru during August 4 -7, 2020.

8. Participated the International Web-Seminar on Recent Trends in Nanostructured Materials based Devices and their Applications organized by department of Physics and IQAC in collaboration with Electra Solar Energy System Pvt. Ltd, MIDC, Koregaon, Maharashtra on July 18, 2020.

9. Participated in the national webinar on Industrial Applications of Electrochemistry organized by PES Institute of Technology and Management, Shivamogga during July 13 - 14, 2020.

10. Attended the webinar on Applications of Cyclic Voltammetry in Research, Organized by Reva University, Bengaluru on July 12, 2020.

11. Participated in two days Webinar on Analytical techniques for determining elemental constituents organized by department of Chemical engineering, SIT, Tumakuru during June 8 - 9, 2020.

12. Participated in the Science leadership workshop organized by the Central University of Punjab, Bathinda from June 22 – 28, 2020.

13. **Oral presentation** in Second International Conference on Advanced Materials and Technology held at Sri Jayachamarajendra College of Engineering, Mysuru during 16th to 18th January 2020.

14. **Poster presentation** in 64th DAE Solid State Physics Symposium held at IIT Jodhpur, Rajasthan organized by BARC, Mumbai from December 18 - 22, 2019.

15. Attended a National workshop on Spectral, Electrochemical and Analytical techniques held at Periyar University**,** Salem, Tamil Nadu, during February 8-9, 2018.

16. Attended INUP Familiarization workshop on Nanofabrication Technologies held at IIT Bombay, during May 25- 27, 2016

17. Attended a National Seminar on Recent developments in nano materials and their applications.

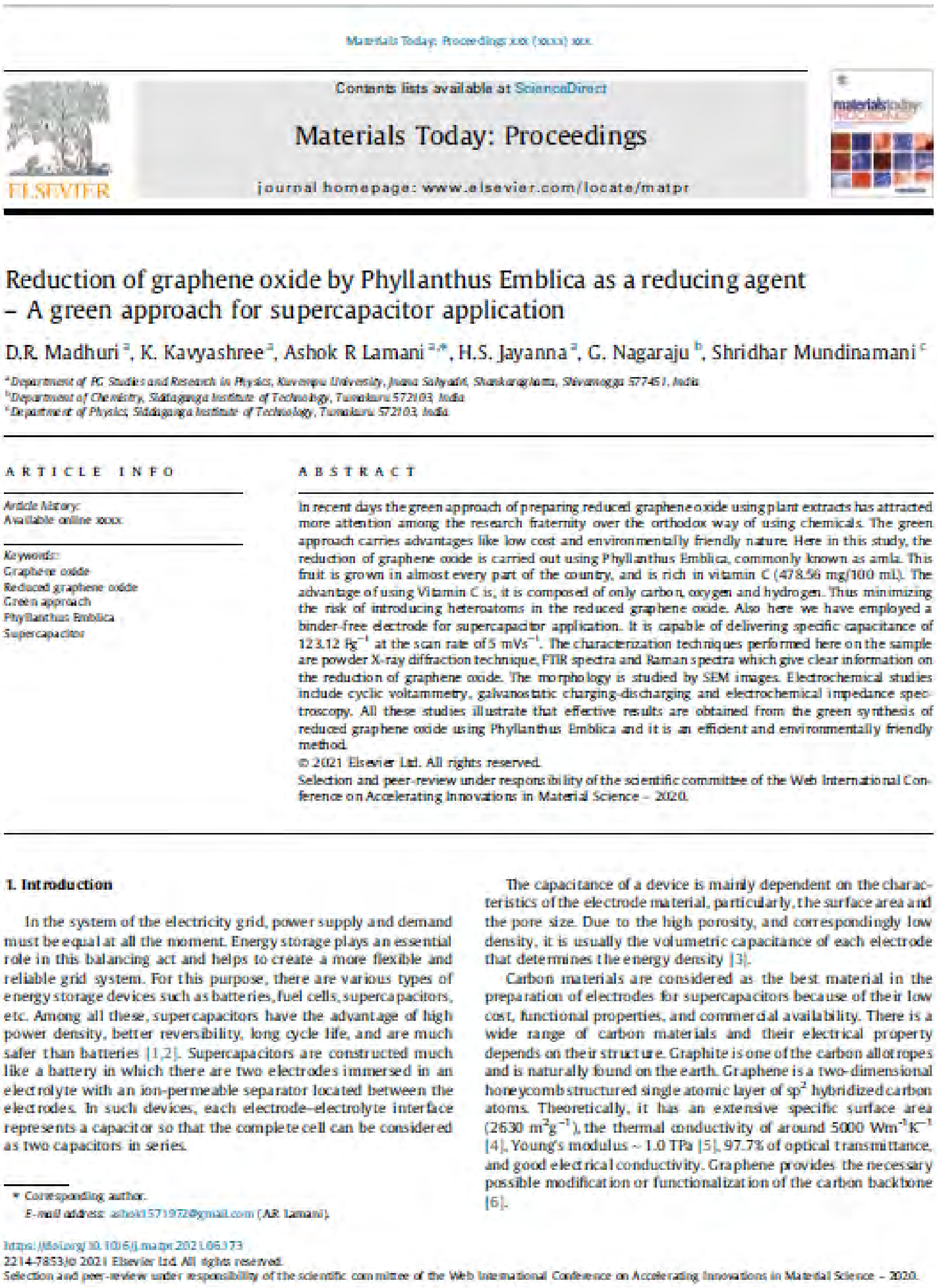

Materials Today: Proceedings xxx (xxxx) xxx

Contents lists available at ScienceDirect

Materials Today: Proceedings

journal homepage: www.elsevier.com/locate/matpr

Reduction of graphene oxide by Phyllanthus Emblica as a reducing agent – A green approach for supercapacitor application

D.R. Madhuri [a], K. Kavyashree [a], Ashok R Lamani [a,*], H.S. Jayanna [a], G. Nagaraju [b], Shridhar Mundinamani [c]

[a] Department of PG Studies and Research in Physics, Kuvempu University, Jnana Sahyadri, Shankaraghatta, Shivamogga 577451, India
[b] Department of Chemistry, Siddaganga Institute of Technology, Tumakuru 572103, India
[c] Department of Physics, Siddaganga Institute of Technology, Tumakuru 572103, India

ARTICLE INFO

Article history:
Available online xxxx

Keywords:
Graphene oxide
Reduced graphene oxide
Green approach
Phyllanthus Emblica
Supercapacitor

ABSTRACT

In recent days the green approach of preparing reduced graphene oxide using plant extracts has attracted more attention among the research fraternity over the orthodox way of using chemicals. The green approach carries advantages like low cost and environmentally friendly nature. Here in this study, the reduction of graphene oxide is carried out using Phyllanthus Emblica, commonly known as amla. This fruit is grown in almost every part of the country, and is rich in vitamin C (478.56 mg/100 ml). The advantage of using Vitamin C is, it is composed of only carbon, oxygen and hydrogen. Thus minimizing the risk of introducing heteroatoms in the reduced graphene oxide. Also here we have employed a binder-free electrode for supercapacitor application. It is capable of delivering specific capacitance of 123.12 Fg^{-1} at the scan rate of 5 mVs^{-1}. The characterization techniques performed here on the sample are powder X-ray diffraction technique, FTIR spectra and Raman spectra which give clear information on the reduction of graphene oxide. The morphology is studied by SEM images. Electrochemical studies include cyclic voltammetry, galvanostatic charging-discharging and electrochemical impedance spectroscopy. All these studies illustrate that effective results are obtained from the green synthesis of reduced graphene oxide using Phyllanthus Emblica and it is an efficient and environmentally friendly method.

Selection and peer-review under responsibility of the scientific committee of the Web International Conference on Accelerating Innovations in Material Science – 2020.

1. Introduction

In the system of the electricity grid, power supply and demand must be equal at all the moment. Energy storage plays an essential role in this balancing act and helps to create a more flexible and reliable grid system. For this purpose, there are various types of energy storage devices such as batteries, fuel cells, supercapacitors, etc. Among all these, supercapacitors have the advantage of high power density, better reversibility, long cycle life, and are much safer than batteries [1,2]. Supercapacitors are constructed much like a battery in which there are two electrodes immersed in an electrolyte with an ion-permeable separator located between the electrodes. In such devices, each electrode–electrolyte interface represents a capacitor so that the complete cell can be considered as two capacitors in series.

The capacitance of a device is mainly dependent on the characteristics of the electrode material, particularly, the surface area and the pore size. Due to the high porosity, and correspondingly low density, it is usually the volumetric capacitance of each electrode that determines the energy density [3].

Carbon materials are considered as the best material in the preparation of electrodes for supercapacitors because of their low cost, functional properties, and commercial availability. There is a wide range of carbon materials and their electrical property depends on their structure. Graphite is one of the carbon allotropes and is naturally found on the earth. Graphene is a two-dimensional honeycomb structured single atomic layer of sp^2 hybridized carbon atoms. Theoretically, it has an extensive specific surface area (2630 m^2g^{-1}), the thermal conductivity of around 5000 $Wm^{-1}K^{-1}$ [4], Young's modulus ~ 1.0 TPa [5], 97.7% of optical transmittance, and good electrical conductivity. Graphene provides the necessary possible modification or functionalization of the carbon backbone [6].

---

* Corresponding author.
E-mail address: ashok1571972@gmail.com (A.R. Lamani).

https://doi.org/10.1016/j.matpr.2021.06.373
2214-7853/© 2021 Elsevier Ltd. All rights reserved.
Selection and peer-review under responsibility of the scientific committee of the Web International Conference on Accelerating Innovations in Material Science – 2020.

A Simple Sonochemical Method of Synthesis of rGO/Co_3O_4 Composite With Binder Free Electrode For Supercapacitors

D.R. Madhuri[1], K. Kavyashree[1], Ashok R Lamani[1], H.S. Jayanna[1], G. Nagaraju[2], Shridhar Mundinamani[3]
[1]Department of PG Studies and Research in Physics, Kuvempu University, Jnana Sahyadri, Shankaraghatta, 577451
[2]Department of Chemistry, Siddaganga Institute of Technology, Tumakuru 572103
[3]Department of Physics, Siddaganga Institute of Technology, Tumakuru 572103

**Corresponding author: ashok1571972@gmail.com*

Abstract

In the present work, we have used Phyllanthus Emblica (amla) as a fuel as well as reducing agent to avoid toxic chemicals. rGO/Co_3O_4 composite was prepared by a simple sonochemical method. The electrodes were prepared by using Whatman filter paper without using any binder. The physico-chemical characterizations were performed by XRD, FT-IR, SEM and Raman spectroscopy. Electrochemical measurements were studied by cyclic voltammetry with two electrode system. The result revealed that the composite material has a very good specific capacitance and excellent cyclic stability.

INTRODUCTION

Supercapacitors have attracted more attention due to its good cycling stability, fast charge-discharge and high power density. Recently graphene has emerged as a promising material for supercapacitor due to its excellent electronic conductivity, extremely high specific area, outstanding mechanical strength, superior thermal conductivity and reasonable chemical stability [1,2]. However, it has been reported that electrodes made of graphene may display decreased surface area due to restacking of the graphene sheets and formation of agglomeration [3]. This drawback can be overcome by the addition of transition metal oxides. Transition metal oxides such as NiO, MnO_2, Fe_2O_3 and Co_3O_4 are being studied as promising materials for pseudocapacitors [4-11].

EXPERIMENTAL

Preparation of graphene oxide: Graphene oxide was prepared by modified Hummer's method.

Preparation of cobalt oxide: Cobalt oxide (Co_3O_4) was prepared by solution combustion method. 1 g of cobalt nitrate was dissolved in 10 mL of DI water. 1.5 mL of amla extract fuel was added and mixed well. The mixture was kept in a pre-heated muffle furnace. Black coloured powder was formed.

Preparation of rGO/Co_3O_4 composite: 300 mg GO was dispersed in 100 mL of DI water, ultrasonicated for 30 mi n. Added 2 mL of reducing agent (amla extract) and again ultrasonicated for 15 min. 300 mg of Co3O4 is added to the above solution, kept under ultrasonicated for 30 min. This was allowed to wash with DI water several times until clear solution was formed.

RESULT AND DISCUSSION

The XRD pattern is shown in figure 1. Diffraction peaks corresponding to GO appears at $2\theta \approx 9.6°$ and 42.3° (PDF no. 44-558) is the characteristic peak. The observed planes of Co_3O_4 belong to cubic structure (JCPDS card No. 42-1467). The average crystallite size of the Co_3O_4 is found to be 44nm.

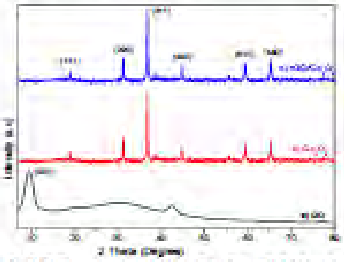

Fig. 1. XRD pattern of GO, Co_3O_4, rGO/Co_3O_4

Figure 2 depicts the FT-IR spectra. The broad peak at 3426 cm^{-1} is due to the presence of O-H stretching vibration in the hydroxyl group. Small

Effect of Graphite Particle Size on Oxidation of Graphene Oxide Prepared by Modified Hummers Method

K. Kavyashree, D. R. Madhuri , Ashok R Lamani[a)], H.S. Jayanna, Hemantha. M

Department of PG studies and research in physics, Kuvempu University, Jnana Sahyadri, Shankaraghatta,Shivamogga,Karnataka,India-577451

[a)]Email:ashok1571972@gmail.com

ABSTRACT: The effect of graphite particle size on oxidation of graphene oxide prepared by Modified Hummer's method has been investigated. The oxidation was performed on three different sized graphite particles 20µm, 100µm and 250µm.The samples were characterized by means of X-ray diffraction, FTIR.The CV studies for the different sized particles has been performed to study the electrochemical behavior of graphene oxide. This study demonstrates the dependence of oxidation of graphene oxide on the particle size of the graphite powder. The smaller particle sized graphite powder shows good oxidation.

Keywords: Graphite powder, graphene oxide, Hummers method, Particle size.

INTRODUCTION

Graphene is a single layer of sp2 carbon atoms arranged in a honeycomb structure. It possesses very high mechanical strength, specific surface area and high thermal and electrical conductivity [1-7].Graphene is a monolayer of carbon that forms a two-dimensional hexagonal sp^2 hybridized structure. Since the discovery of exfoliated free-standing graphene from bulk graphite using the "scotch tape" method, graphene has attracted much attention not only in fundamental research fields but also in various application fields due to its outstanding and unique electronic and mechanical properties. In particular, it has the potential to serve as a key component in energy storage devices such as fuel cells and Supercapacitor [8].Strong oxidizing agents can be used to produce oxidized forms of graphene, designated as graphene oxide (GO). Also, graphite can be directly oxidized to produce graphite oxide, which can then be exfoliated originating GO [9]. The exfoliation of graphite to graphene can be realized either physically or chemically [10]. Chemical methods are the most common ways of making graphene due to their high yield production and control. In addition, the final products of these methods are a colloidal suspension that provides a possibility of subsequent modifications such as functionalization [11].

EXPERIMENTAL

Experiments with three kinds of graphite powders with different size distribution were performed. The first sample was the graphite that was purchased from Lobo Chem. The second and third samples were purchased from S D Fine Chemicals Company and Sigma Aldrich Company and XRD images of the samples were shown in Figure. The average particle size of the first, second and third samples were 20 µm, 100 µm, and 250 µm, respectively. Potassium permanganate ($KMnO_4$) and sodium nitrate ($NaNO_3$) were purchased from Sigma Aldrich chemical Co., Ltd. Sulfuric acid (H_2SO_4) and hydrochloric acid (HCl) were obtained from Merck. Hydrogen peroxide (H_2O_2) was purchased from Merck. All the chemicals were research grade and used without any purification.Deionized water was used throughout the experiment.

DAE Solid State Physics Symposium 2019
AIP Conf. Proc. 2265, 030096-1–030096-4; https://doi.org/10.1063/5.0017325
Published by AIP Publishing. 978-0-7354-2025-0/$30.00